The healthy and keratoconic human cornea: structure, imaging, mechanical characterization and modeling

Chloé Giraudet, Jean-Marc Allain

La cornée humaine saine et kératoconique : structure, imagerie, caractérisation mécanique et modélisation

The healthy and keratoconic human cornea: structure, imaging, mechanical characterization and modeling.

Chloé Giraudet [1,2], Jean-Marc Allain [1,2] (jean-marc.allain@polytechnique.edu)

[1]Laboratoire de Mécanique des Solides, CNRS, École Polytechnique, Institut Polytechnique de Paris,
[2]Inria

RÉSUMÉ. Cet article vise à faire un état des lieux de nos connaissances de la cornée humaine, sa structure et son comportement, en vue d'une modélisation mécanique. Il présente dans un premier temps l'organisation générale de la cornée, ainsi que ses macro et microstructures. Dans un second temps, nous détaillons les techniques de Tomographie par Cohérence Optique (OCT), qui sont utilisées en clinique et en recherche pour observer la cornée. Ensuite, nous présentons la caractérisation expérimentale des propriétés mécaniques de la cornée. Enfin, nous passons en revue les approches de modélisation qui ont été utilisées pour décrire la réponse élastique du tissu.

ABSTRACT. This paper aims to give a review of our knowledge on the human cornea, its structure, and its behavior, for mechanical modeling. It presents first the general organization of the cornea, as well as its macro and microstructures. In a second time, we detail the Optical Coherence Tomography (OCT) techniques, which are used in clinics and in research to observe the cornea. Then, we present the experimental characterization of the cornea mechanical propoerties. Finally, we review the modeling approaches that have been used to describe the elastic response of the tissue.

MOTS-CLÉS. Cornée, microstructure, imagerie, lamelles de collagène, OCT, DIC/DVC, caractérisation mécanique, modélisation mécanique, kératocone

KEYWORDS. Cornea, microstructure, imaging, collagen lamellae, OCT, DIC/DVC, mechanical characterization, mechanical modeling, keratoconus

Introduction

Cornea is the most external tissue of the eye, responsible of our vision through its transparancy and its shape. Pathological alteration of the cornea mechanical properties or structure may lead to a loss of vision, and thus have attracted biomechanical studies in the past, with a focus on the role of the collagen microstructure. We propose here a review of the litterature on the biomechanics of the cornea. To do so, we will first describe the multiscale structure of cornea (Sec. 1.). Then, we present the main imaging technique, the Optical Coherent Tomography, which is used *in-vivo* or *ex-vivo* (Sec. 2.). Then, we present the mechanical characterizations, also *in-vivo* and *ex-vivo* (Sec. 3.). Finally, we will give some insights of the current models develops to describe the cornea at the scale of the tissue (Sec. 4.). In all section, we illustrate the effect of a pathological alteration throught the case of the keratoconus: this disease, which couples mechanical weakening and structural alteration, has attracted the attention of the biomechanical community.

1. Structure of the cornea

1.1. *Anatomy of the cornea*

Macroscopic description

The cornea is the external part of the eye (Fig. **1**.a-b). It is a transparent medium that transmits light inside the eye and protects it from external aggression. Accounting for 2/3 of the refractive power of the eye (around 40 diopters over 60), the cornea forms with the crystalline lens the ocular diopter, whose function is to focus the light on the retina. The cornea is attached to the eyeball through the sclera, the white tissue surrounding it (Fig. **1**.a). Its posterior surface is in contact with the aqueous humor, a transparent liquid composed of 99% water (refractive index $n_{aqh} = 1.3375$ [Sardar et al., 2007]): see Fig.**1**.c (anterior and posterior surfaces are the external and internal ones, respectively). Aqueous humor plays a key role in providing nutritional metabolic function to the lens and the cornea, and in regulating intraocular pressure (IOP), which is between 10 and 20 mmHg (1.3 and 2.7 kPa respectively) in healthy conditions [Hashemi, 2005].

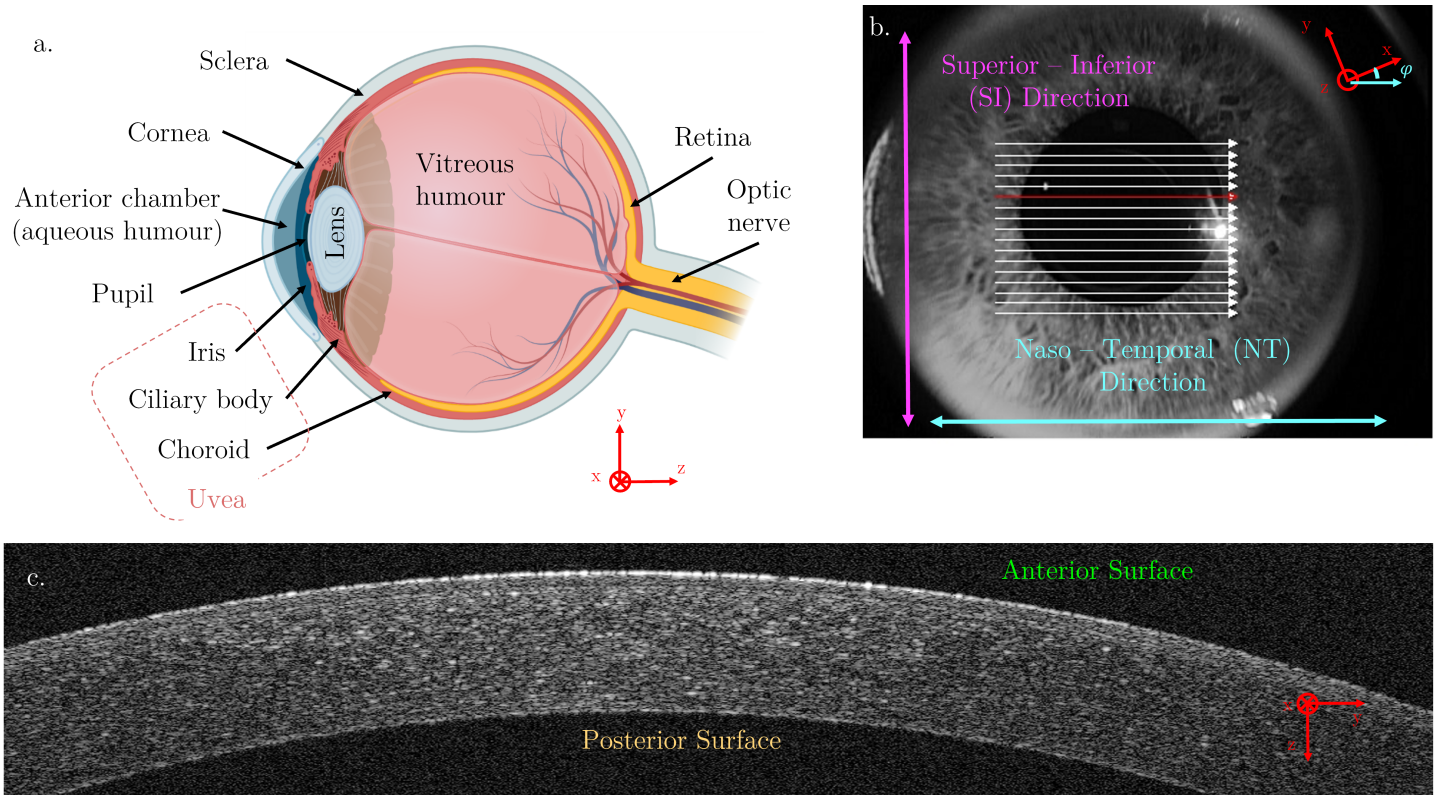

FIGURE 1. *a. Schematic view of the eye: the cornea is the external part of the eye, surrounded by the sclera and forming the optical diopter with the crystalline lens – [Created with BioRender.com]. b. Photo of an eye viewed from the front with the classical directions used in ophthalmology: Superior–Inferior in pink and Naso-Temporal in blue. c. Optical Coherence Tomography (OCT) image of a cornea defining the anterior and posterior surfaces (images b and c provided by Pr. Borderie from the 15-20 Hospital, Paris, France). The coordinate system is the same in all the scheme/images.*

Geometry

The corneal shape is close to a spherical cap. Typical dimensions of the cornea are around 1 cm in diameter, a thickness between approximately 500 μm in the central part and 600 μm in the periphery, and radii of curvature around 7.8 mm for the anterior surface and 6.5 mm for the posterior surface

[Mashige, 2013]. The geometry of the healthy cornea is regular and well described by a parametric quadratic equation [Gatinel et al., 2011]. Placing the apex of the cornea at the origin of a coordinate system with the z-axis oriented vertically and downwards (Fig 1.c for the representation of the axes), the anterior and posterior surfaces of the cornea are described by the biconic function [Janunts et al., 2015]:

$$z(x, y, R_x, R_y, Q_x, Q_y) = z_0 + \frac{\frac{x^2}{R_x} + \frac{y^2}{R_y}}{1 + \sqrt{1 - (1+Q_x)\frac{x^2}{R_x^2} - (1+Q_y)\frac{y^2}{R_y^2}}}, \tag{1}$$

where R_x and R_y are the curvature radii of the flattest (x axis) and the steepest (y axis) meridians of the cornea, Q_x and Q_y are the associated asphericities. Note that the x and y directions can be rotated by an angle ϕ from the classical naso-temporal (N-T) and inferior-superior (I-S) axes (Fig. 1.b). Finally, z_0 is an arbitrary translation with respect to the z axis origin.

Considering this approximation of the geometry of the cornea, the local diopter of the cornea is computed using:

$$D = \frac{n_{aqh} - n_{air}}{R_{ant}} \tag{2}$$

with $n_{aqh} = 1.3375$ and $n_{air} = 1.0000$ the refractive index of the aqueous humor and the air respectively and R_{ant} the local steepest curvature radius of the anterior surface.

Mesoscopic organization

The cornea is composed of six layers (a histological section is presented Fig. 2) described hereafter from the most external layer to the most internal one.

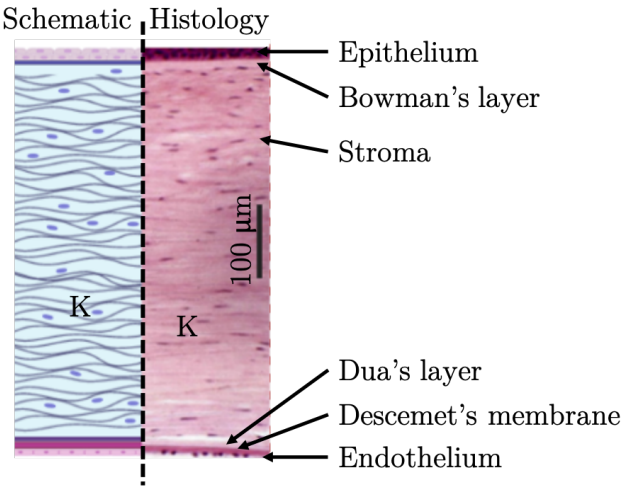

FIGURE 2. *Schematic view (left – [Schematic created with BioRender.com]) and histological section (right – from [Napoli et al., 2020]) of the cornea.*

The epithelium is the external part, composed of a few layers of epithelial cells (50-90 μm thick), and plays the role of a barrier against external aggression and a facilitator for the dispersion of the tears. Bowman's membrane is a non-cellular homogeneous layer (approximately 10 μm thick) composed of

collagen fibrils [Hayashi et al., 2002], which has the particularity to not regenerate after destruction. The stroma is the main part of the cornea and will be described in more detail in the following section (Sec. 1.2.). The fourth layer is Dua's layer, which was only discovered in 2013 [Dua et al., 2013]. It is around 15 μm thick and located between the stroma and Descemet's membrane. Its role is not yet clear. Descemet's membrane is a base membrane of the endothelium – and therefore plays the role of a joint between the stroma and the endothelium – and is mostly composed of a type VIII collagen network [Espana and Birk, 2020]. It grows over life from 3-4 μm thick at childhood to around 12 μm for adults [Bourne, 2003]. Finally, the endothelium is a single layer of endothelial cells approximately 5 μm thick. The endothelial density is between 3000 to 4000 cells$/mm^2$ for a new born and decreases down to approximately 2000 cells$/mm^2$ at old age [Bourne, 2003]. The endothelial cells do not regenerate so that when one of them dies, the surrounding cells enlarge to fill up the void. The endothelium acts like a pump between the aqueous humor and the cornea to maintain constant hydration – and with it transparency – of the tissue [Mergler and Pleyer, 2007]. It is commonly admitted that below a certain cell density (between 400 and 700 cells/mm^2 [Kaufman et al., 1998]), the endothelium does not longer fulfill its pumping role and then stromal edemas appear.

1.2. *Stroma*

The stroma represents about 90% of the cornea. It provides the cornea its mechanical strength and optical performance (transparency and optical power). This is due to the particular arrangement of collagen inside the tissue [Meek and Knupp, 2015, Ruberti et al., 2011]: the stroma is composed mainly of type I et V collagen fibrils arranged in lamellae anchored in a matrix of keratocytes (corneal fibroblasts) and proteoglycans [Espana and Birk, 2020]. Hereafter are described the multiple scales of collagen arrangement, from smallest (the triple helix) to largest (lamellae). The largest ones are detailed more precisely (see Fig. **9** for a summary of all scales), as they are consider as more important in the mechanical response.

1.2.1. Smallest scales of stromal collagen: the triple helix, the microfibril and the fibril of collagen

The triple helix of collagen (Fig. **3**.a) is one of the smallest observable arrangement of collagen monomers, with a diameter of only 1.5 nm. X-ray diffraction is one of the techniques available to observe the triple helix of collagen. It has been first applied on kangaroo tails (Fig. **3**.b) and led to a founding article on the organization of collagen at the smallest scale. It allows patterns of the arrangement of the collagen to be distinguished when looking at the different layers (e.g. alternation of black and white on the scattering gives a periodic pattern), but it is necessary to add amino acid composition and physicochemical data to obtain the classical 7/2-helical model (7 different amino acid per 2 turns of helix – Fig. **3**.c) found in [Okuyama et al., 2006].

Multiple triple helices of collagen pack to form 4 nm diameter microfibrils of collagen which axial arrangement is represented in Fig. **4**.a and c. Electron microscopy (Fig. **4**.b from [Marchini et al., 1986]) and tomography (Fig. **4**.c [Holmes et al., 2001]) allowed to observe the microfibrils of collagen of bovine cornea (orange boxes). They give access to the microfibril arrangement, which follows an alternation of overlap and gap zones with a period of 670 $\mathring{A}$ (Fig. **4**.c).

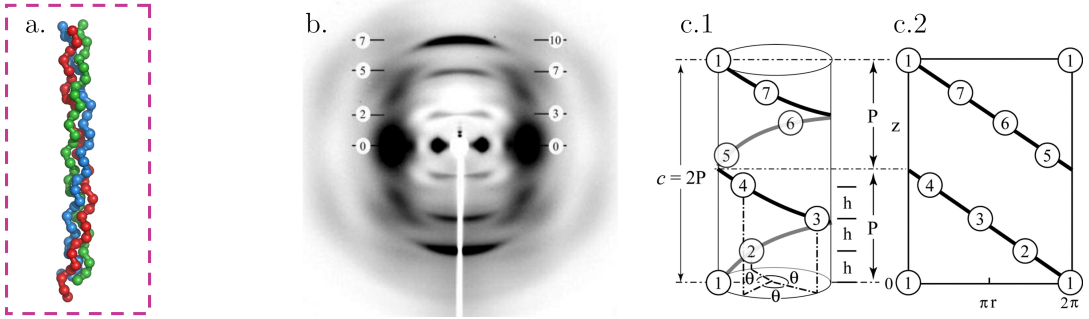

FIGURE 3. *a. Schematic view of the triple helix of collagen [Created with BioRender.com]. b. X-ray diffraction scattering (from [Okuyama, 2008]) of the triple helix of collagen in a kangaroo tail. c. schematic representation of the monomer of the triple helix (from [Okuyama et al., 2006]).*

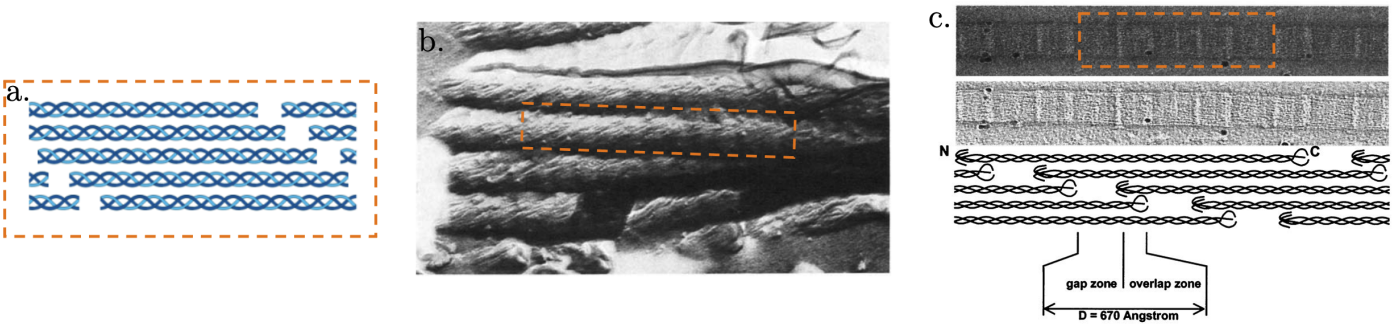

FIGURE 4. *a. Schematic view of a microfibril of collagen [Created with BioRender.com]. b. Electron microscopy (from [Marchini et al., 1986] - 80000X). c. Electron tomography image (from [Holmes et al., 2001] – 20000X) of the microfibrils of collagen of a bovine cornea.*

The microfibrils of collagen are themselves packed in fibrils of collagen (Fig. 5) of around 30 nm in diameter. Figure 5.b presents Transmission Electron Microscopy (TEM) images where the fibrils of collagen can be distinguished. TEM images also show that the directions of the fibrils of collagen alternate through the thickness of the cornea – from top to bottom three layers of fibrils of collagen. A keratocyte (corneal fibroblasts) can be distinguished on this image.

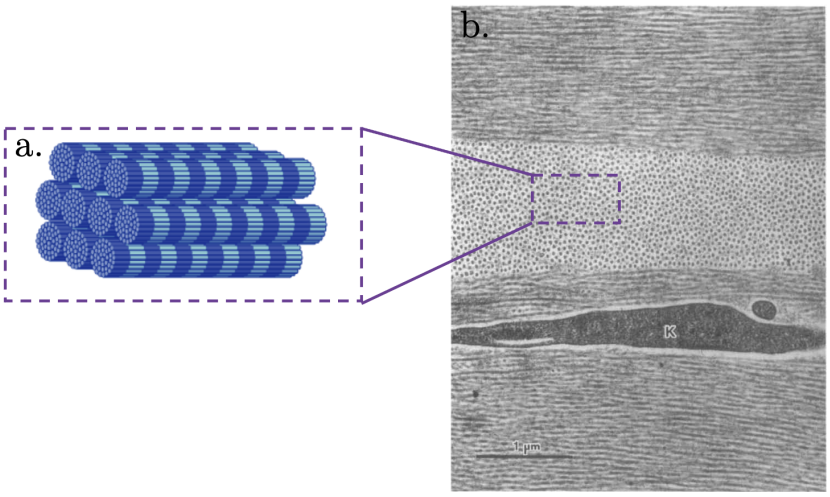

FIGURE 5. *a. Schematic view [Created with BioRender.com] and b. TEM image (from [Komai and Ushikif, 1991]) of the fibrils of collagen of a human cornea. K = keratocyte. Scale bar: 1 μm.*

1.2.2. Collagen lamellae

Figure 5 shows not only the fibrils but their upper scale organization: they form lamellae, the largest scale of collagen arrangement in the cornea. Collagen lamellae are arranged like a plywood with an alternation of lamellae with different directions (Fig. 6.a). Scanning Electron Microscopy (SEM) and Second Harmonic Generation (SHG) microscopy images (Fig. 6.b and c) reveal the presence of the lamellae (red "L's" on the images). The SEM image also shows that the lamellae are intertwined rather than just superimposed on top of each other, whereas the SHG image points out that the angles between the different lamellae are not exactly 90°.

The scale of the lamellae is generally the one used in mechanical models of cornea, which are inspired from the extensively used models of materials reinforced by fibers (Sec. 4.). This leads to a terminology confusion, with the use of "fibers" and "lamellae" to describe the lamellae. We will try to stick to lamellae, but, from now, if "fiber" is used, it should be understood as collagen "lamellae". The lamellae are heterogeneously distributed in the cornea. To quantify this heterogeneity, X-ray (Fig. 7.a) and SHG (Fig. 7.b) images have been used.

X-ray imaging allows the scattering pattern of the collagen in the lamellae to be obtained, averaged over the thickness of the tissue [Meek and Quantock, 2001, Meek and Boote, 2009]. Fig. 7.a presents the results of X-ray analysis, with a polar plot (butterfly diagram) of the lamella direction at each point of measurement, which gives an in-plane information on the average orientation of the lamella through thickness. The radial extent of the polar plot shows the relative number of collagen lamellae aligned in a

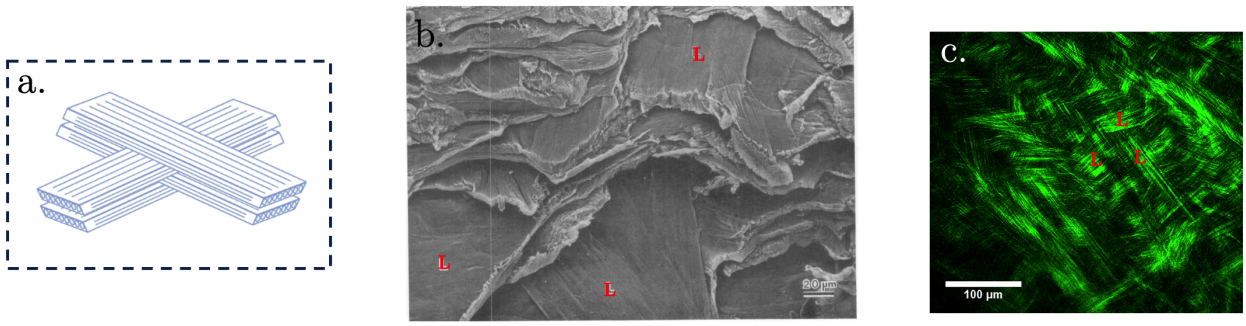

FIGURE 6. *a. Schematic view of the lamellae of collagen [Created with BioRender.com]. b. SEM image of the cornea (from [Komai and Ushikif, 1991]) – scale bar: 20 μm. c. SHG image of the cornea (from [Benoit et al., 2016]) – scale bar: 100 μm.*

particular direction, i.e. the longer the wing of the butterfly, the more lamellae along that direction. The width of the butterfly wings represents their scatter. The colors of the different butterflies indicate the factor with which the polar plots have been scaled down on the representation of Fig. **7**.a. Two main observations are drawn from this analysis. First, the lamellae in the center are oriented in the naso-temporal (N–T) and superior-inferior (S–I) directions with an angle of approximately 90°, while in the peripheral zone, the lamellae are mostly oriented in the circumferential direction of polar coordinates. Second, fewer lamellae (in orange, i.e. with no scaling) are oriented in the central area than in the peripheral one (mostly in dark red, black and green so with a scale down factor of 2, 3 or 4 on the representation).

Although X-ray analysis gives valuable information on the in-plane distribution of the lamellae, it does not give any insight into the out-of-plane distribution. To this end, SHG images (from [Winkler et al., 2011]) have been analyzed by Petsche and Pinsky [Petsche and Pinsky, 2013] to determine the out-of-plane dispersion of the collagen lamellae. They have shown that the maximum out-of-plane angle of the collagen lamellae varies with depth – decreasing from approximately 30° on the anterior part of the cornea to almost 0° on the posterior stroma – while no heterogeneity has been noted in the other two directions.

Those two analyses allow 3D maps of the orientation of the collagen lamellae in healthy corneas to be built. However, they remain limited to a very small number of cornea (around 1 or 2 per imaging approach method). In the case of pathological corneas such as keratoconus (see Sec. 1.3.), the arrangement of the collagen lamellae is altered, which affects the mechanical strength and the optical properties of the cornea, therefore causing a loss of vision.

1.2.3. Stromal striae

At tissue scale, "X-shape" linear structures appear both on Optical Coherence Tomography (OCT) images (Fig. **8**) and on histological cuts [Napoli et al., 2020]. They are called Vogt's or stromal striae, and are detected in healthy and pathological corneas [Grieve et al., 2017]. They are associated with a wrinkle of the collagen lamellae, but their organisation remains not so well understood. The stromal striae become less visible as the intra-occular pressure increases, meaning that these wrinkles fade with pressure (like a balloon that loses its ripples as it inflates). It suggests that the striae may have a protective

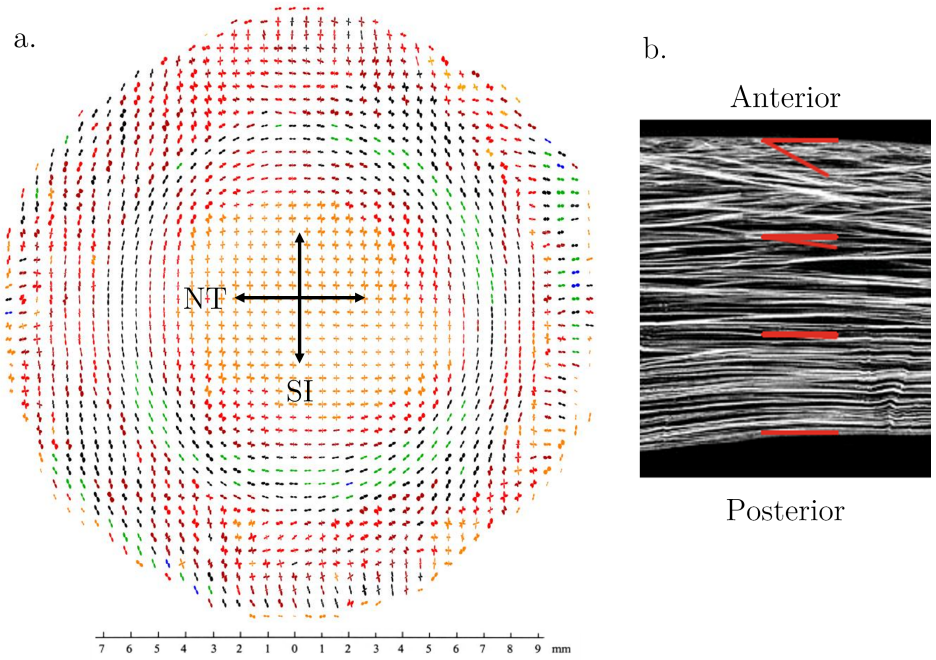

FIGURE 7. *a. In-plane and b. out-of-plane (right) distributions of the orientation of the collagen lamellae (width between 500-600 μm). The in-plane orientations have been determined by analyzing X-ray scattering observation (from [Aghamohammadzadeh et al., 2004, Boote et al., 2006]) (down scale factor: orange – 1, red – 1.5, dark red – 2, black – 3, green – 4, blue – 5), and the out-of-plane orientations use SHG images (from [Petsche and Pinsky, 2013, Winkler et al., 2011]).*

role from damage induced by a sudden increase in pressure (when the eyes receive mechanical shocks for instance) [Grieve et al., 2017].

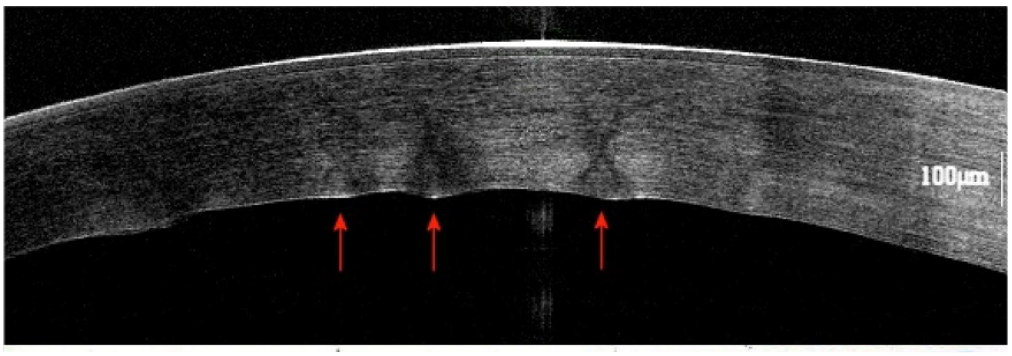

FIGURE 8. *Vogt striae in a human cornea on OCT imaging (top) and histology (bottom). The arrows indicate the most conspicuous 'X-shaped' structures. Scale bar: 100 μm (extracted from [Napoli et al., 2020]).*

1.2.4. Summary of all scales

Figure **9** summarizes the different scales of the components of the cornea, especially the different scales of collagen found in the stroma.

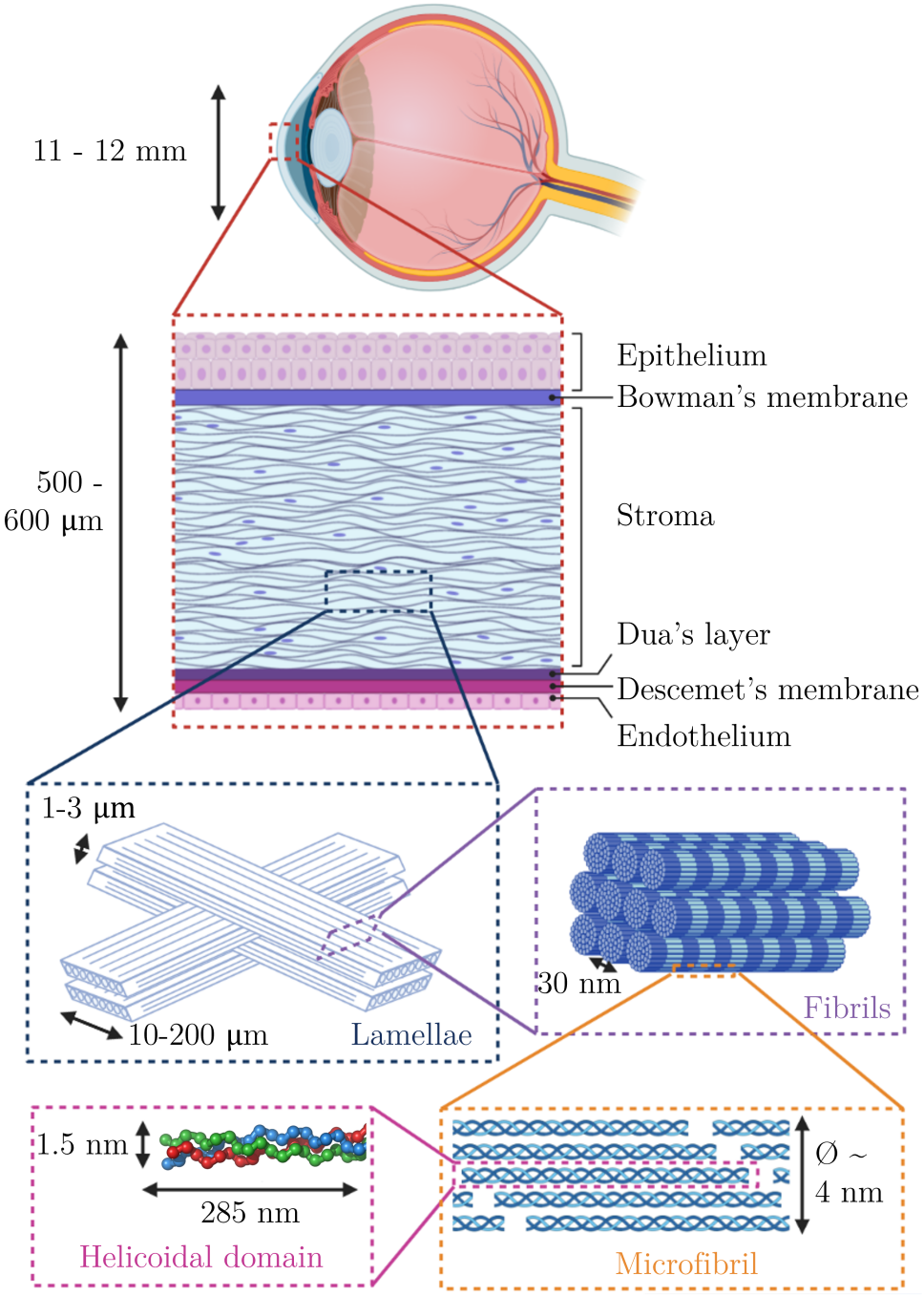

FIGURE 9. *Schematic view of the different scales of the components of the cornea. Top: eye scale. Red box: different layers composing the cornea – tissue scale. Blue box: collagen lamellae – micrometric scale. Violet box: fibrils of collagen – micro- to nanometric scale. Orange box: single microfibril of collagen – nanometric scale. Pink box: triple helix of collagen – nanometric scale. [Created with BioRender.com]*

1.3. *The keratoconus*

Keratoconus is an idiopathic pathology characterized by ectasia (corneal deformation) and progressive non-inflammatory localized thinning of the cornea. In other words, the cornea changes its shape during the progression of the pathology, from a quasi-spherical shape to an irregular conical one (Fig. **10**). This condition affects approximately 1 over 2000 to 500 new patients each year.

The keratoconus usually appears at the end of adolescence and affects both eyes, but not necessarily with the same severity nor in the same area of the eye. Although there is no clear origin of the disease, some risk factors have been identified such as family history (even if no specific gene has yet been identified), presence of allergy in the patient or regular eye rubbing [Najmi, 2019].

Four stages of the disease can usually be identified (Krumeich's classification [Naderan, 2017]): from the least advanced stage (stage I or frustrated stage), with visual discomfort, decrease in visual acuity, and astigmatism, to the most advanced stage (stage IV or severe stage), with thinning associated with a loss of transparency, scars or opacities at the top of the cone, and risk of acute keratoconus. The evolution from a stage to another is not systematic, not symmetric and not linear with time.

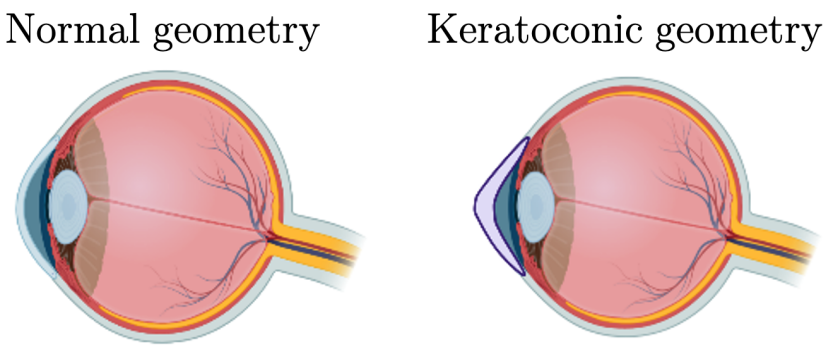

FIGURE 10. *Schematic representation of a keratoconus: the shape of the cornea changes from a spherical to a conical one [Created with BioRender.com]*

Treating keratoconus involves two parallel tasks: improving the patient's vision and stopping the progression of the disease. To stop the progression, one can use a corneal cross-linking treatment. It is based on the photo-polymerization of the collagen by riboflavin previously impregnated on the cornea. To improve the patient's vision, the method is to use first glasses, then therapeutic contact lenses, and in case of failure of those two approaches, corneal surgery. In the latter case, two options are considered: the placement of intra-corneal rings or corneal transplant (only 1% of the patient with a known keratoconus go through the latter). Intra-corneal rings are used to delay grafting. They are placed in the thickness of the cornea to tighten the central cornea. This technology has become more commun with the improvement of femto-second lasers, which enable to dig tunnels with extreme precision in the cornea, through which the surgeons introduce the intra-corneal rings. To treat the keratoconus, another approach can be used, based on the "Excimer" laser treatment. It allows the cornea to be remodeled by photo-ablation of the tissue and the visual accuracy of the patient to be increased, who will need a smaller visual correction. This technique is called LASIK surgery (Laser In Situ Keratomileusis) and is usually coupled with cross-linking to stop the progression of the disease. Finally, when all those techniques have failed, the only choice that remains is the graft. In the case of a keratoconus, surgeons perform a deep anterior

lamellar graft, which keeps the posterior part of the patient's cornea and only transplants the anterior part of the donor's cornea.

The change of shape of the cornea in case of a keratoconus comes with an alteration of the collagen lamellae. Figure **11** presents the orientation of the lamellae of collagen in one healthy and one stage III keratoconic cornea, taken at the central part of the cornea (Fig. **11**.a and b). In the case of a healthy cornea, it confirms that the lamellae are mostly parallel to the surface of the cornea (greenish and blueish colors on Fig. **11**.c) which is emphasized by the large peak near 0 on the histogram of out-of-plane orientations (Fig. **11**.e). On the other hand, the keratoconic cornea presents more diverse colors than the control one (Fig. **11**.d) – which is in agreement with the scatter in orientation angle in the middle stroma observed in the histograms on the right (Fig. **11**.f). SHG images also show that the lamellae are curved in the case of the keratoconic cornea, while they are straight for healthy cornea. Those structural changes in the tissue lead to different mechanical responses of the corneal stroma, which will be studied in Sec. 4.2..

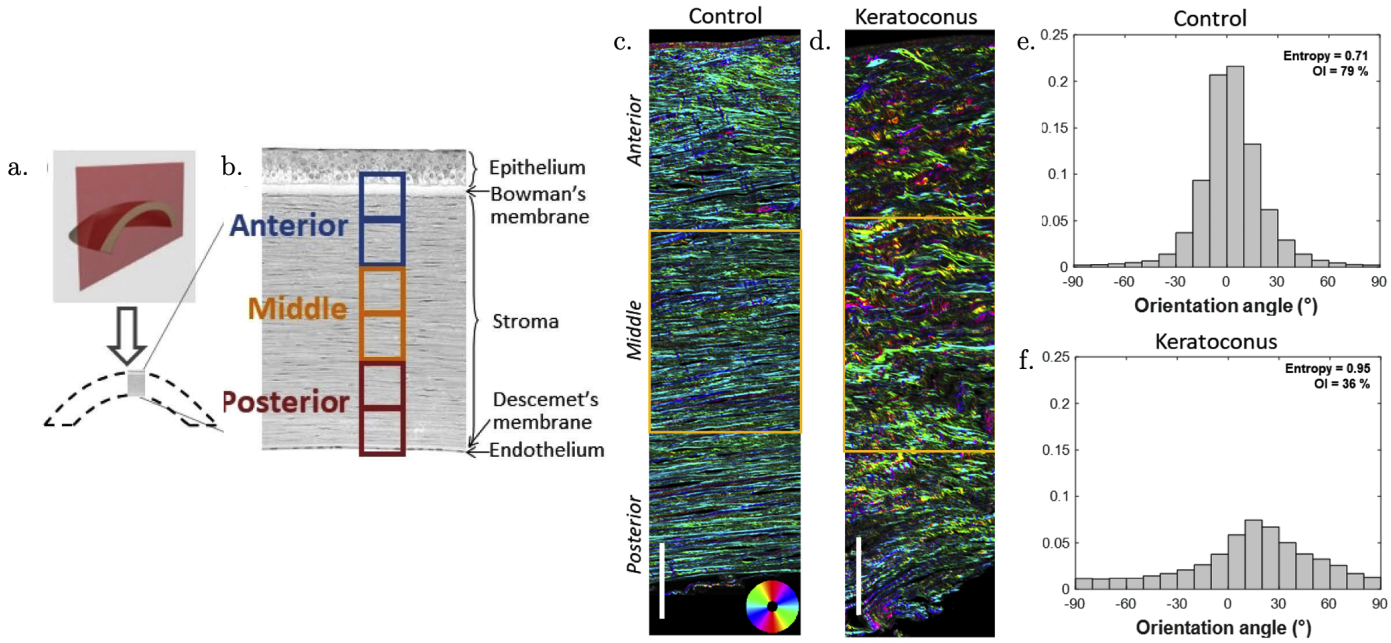

FIGURE 11. *Orientation distribution of collagen lamellae in control and stage III keratoconic corneas on samples located in the central part of the cornea (from [Raoux et al., 2021]). a, b. Location of the imaged samples. The anterior, middle and posterior stroma of the central part of the cornea are imaged. c, d: Typical out-of-plane orientation maps obtained from P-SHG images of transverse sections of the same control c. and keratoconic d. human corneas – scale bars: 100 μm – and e, f: histograms of the collagen out-of-plane orientation in the middle stroma of the e. control and f. keratoconic corneas displayed in c and d.*

2. Optical Coherence Tomography (OCT) and Image analysis

2.1. *Optical Coherence Tomography*

A variety of imaging techniques have emerged in the literature regarding tomography, the imaging technique allowing to look inside a material, and especially for biological tissues imaging. X-ray computed

tomography, confocal microscopy, magnetic resonance imaging (MRI) or Optical Coherence Tomography (OCT) are the most used in hospitals today. They each have their specificities (resolution, field of application...) and are based on different theories. In the case of the eye, the reference technology is OCT, which is widely used in clinics to image the retina and the cornea.

2.1.1. Principle of OCT

This section is largely based on [Drexler et al., 2014, Grieve, 2019, Davis, 2019]. It summarizes the principle of the most widely used OCT systems.

General principle

Optical coherence tomography (OCT) systems are non-contact and non-invasive systems using light scattering (particularly the reflectivity) of the imaged sample. The incident light is partially reflected by the internal structures of the sample (Fig. **12**). The characteristics of the reflected waves (amplitude and travel time) are then analyzed to compute a reflectivity map of the sample.

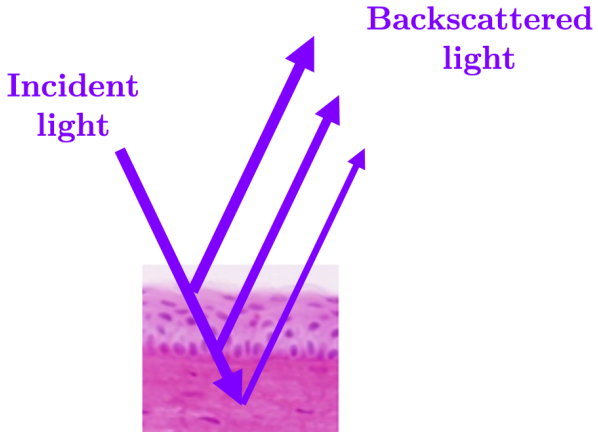

FIGURE 12. *General principle of Optical Coherence Tomography (OCT) systems. The incident light is reflected by the internal structures of the samples and the reflected waves are analyzed to create the reflectivity map (adapted from [Davis, 2019]).*

Since it is not possible to capture the reflected waves directly with sensors (the speed of light being too fast), another method – interferometry – has to be used. In the case of OCT systems, a Michelson interferometer is used to image the sample, taking advantage of the low coherence property of the light source to create localized interferences. Figure **13** presents the principle of the different OCT systems commonly used in hospitals today.

First, the light is split using a beam splitter (BS in Fig. **13**) between the reference and the sample arms. Then the signal is reflected both by the reference mirror and the reflective interfaces of the sample. The back-reflected signals create interferences when the optical path lengths are the same (within the coherence length) and then they are captured by a detector. With the optical path of the reference arm known, the interference signal is processed to generate images of the sample interfaces, and with that, reflectivity depth-profiles named A-scan. The axial (depth) resolution of the interferometer is determined

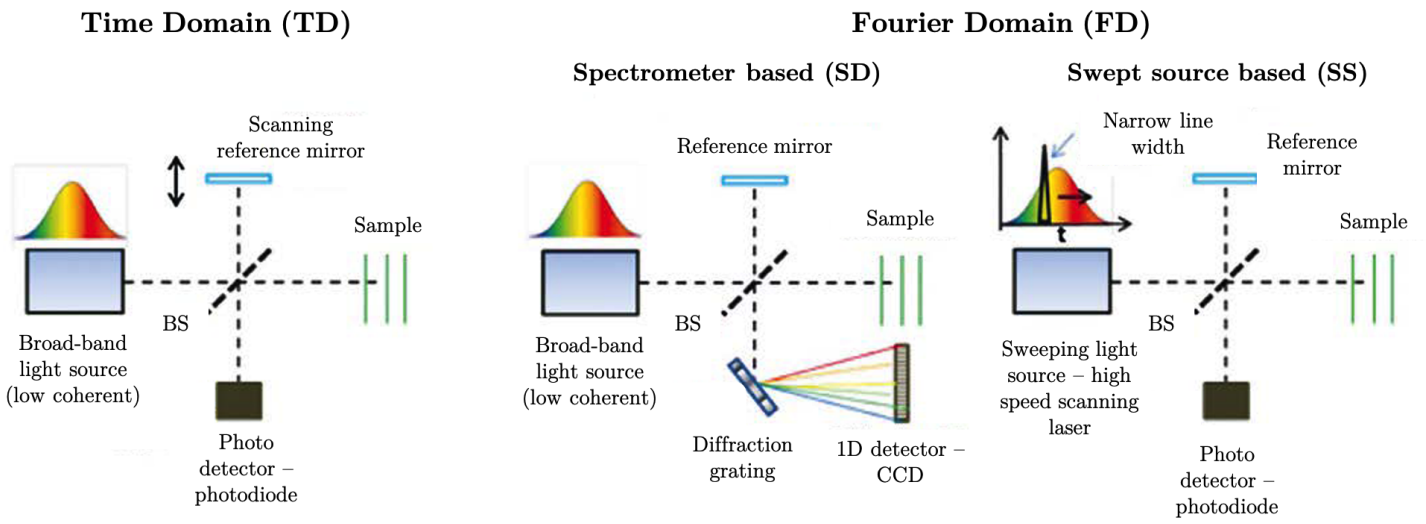

FIGURE 13. *Optical Coherence Tomography (OCT) systems can be divided into Time Domain (TD) and Fourier Domain (FD) systems. These last ones can also be separated into two types, the spectrometer based and the swept source based systems (adapted from [Drexler et al., 2014]).*

by the so-called coherence length, which is classically defined by:

$$l_c = \frac{2\ln 2}{\pi}\frac{\lambda_0^2}{\Delta\lambda} \tag{1}$$

with λ_0 the central wavelength of the spectrum and $\Delta\lambda$ the width of the spectrum. Note that the wider the spectrum, the smaller the coherence length and therefore the better the resolution. A simplified version of the intensity at the output of the interferometer (as the sum of the reference and object arm intensities) is [Davis, 2019]:

$$I(z) = \frac{I_0}{4}[R_{inc}(z) + R_{coh}(z) + R_{ref} + 2\sqrt{R_{ref}R_{coh}(z)}V_{coh}(z)\cos(\Delta\phi(\lambda_0, z))] \tag{2}$$

with $R_{coh}(z)$ the proportion of coherent back-scattered photons, $R_{inc}(z)$ the proportion of incoherent back-scattered photons, R_{ref} the reflectivity of the reference surface, $\Delta\phi$ the phase shift between the two arms of the interferometer and $V_{coh}(z)$ the Gaussian envelope of the wave, centered on the plane of zero step difference.

The phase in Eq. (2) is given by:

$$\Delta\phi(\lambda_0, z) = \frac{2n\pi}{\lambda_0}z \tag{3}$$

with n the refractive index and z the reference mirror position. This means that a change in intensity can be either obtained with a fixed wavelength λ_0 and a variable position z (TD-OCT) or with a variable wavelength λ_0 and fixed position z (FD-OCT) (Fig. **13**).

TD- and FD-OCT

TD-OCT systems use a broad-band light source (such as white light generated by optical fiber) with low coherence. This requires having very close optical paths between the two arms to obtain interferences. In this case, the position of the reference mirror changes (z in Eq. (3)) to create the interference

with the different reflected interfaces of the sample and create an A-scan. Figure **14**.a presents typical interferograms for two reflected interfaces of the sample. The envelope of the interferogram gives information on the material: the peak of intensity is related to the refractive power of the sample at that location. At the maximum intensity, constructive interferences appear: the image on the detector appears in white. Considering all the different intensity peaks, one can reconstruct the different gray levels of the A-scan. To distinguish two different interfaces of the sample, the two associated interferograms should be distinguishable. Thus, the coherence length of the source gives the limitation for the axial resolution of OCT. Once the A-scan is completed, a lateral sweeping (B-scan) is done to obtain a 2D image of the sample, and with a stack of 2D images, a 3D reconstruction of the sample can be obtained.

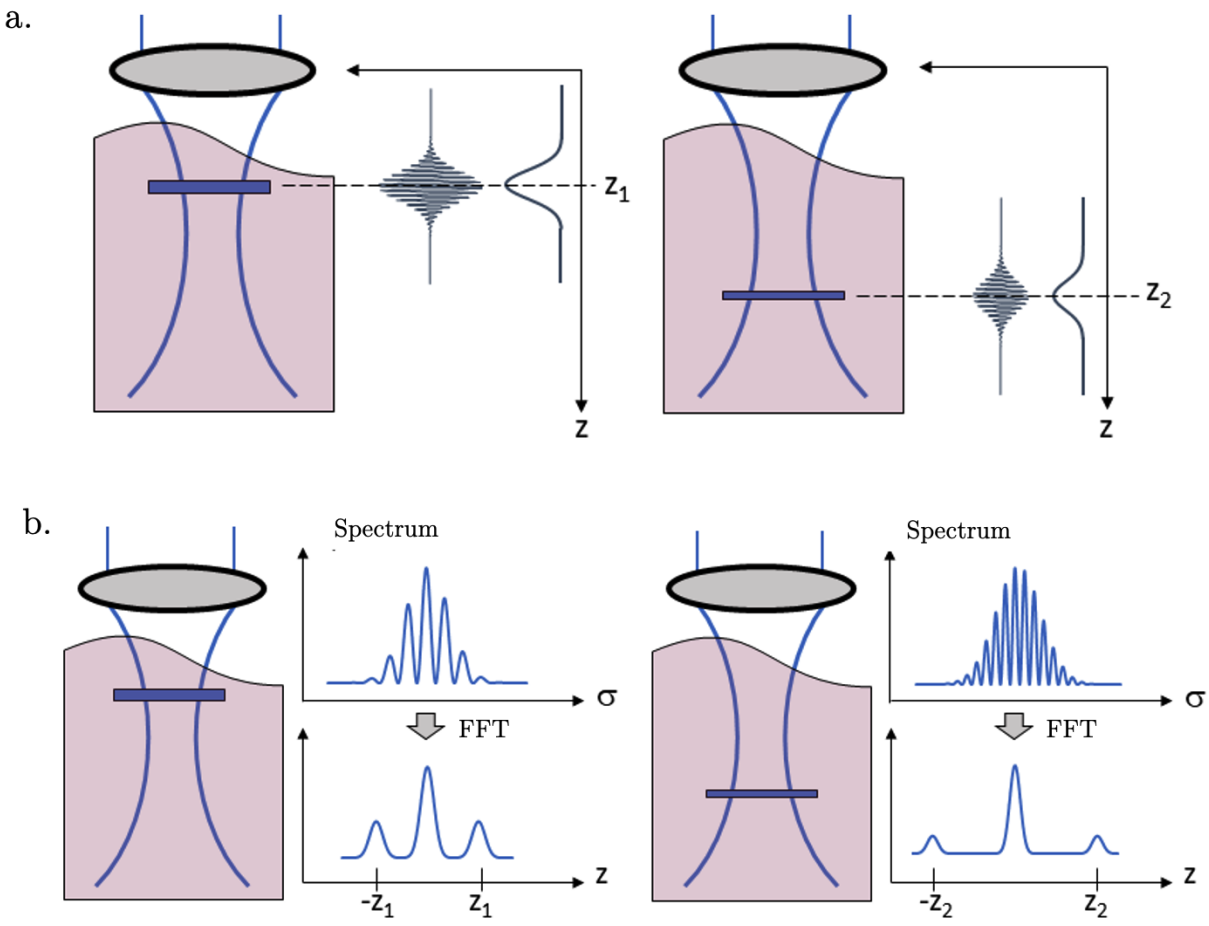

FIGURE 14. *a. Typical interferograms of TD-OCT systems and b. typical spectrum of FD-OCT systems (adapted from [Davis, 2019]).*

In the case of FD-OCT, the reference arm does not move, but the wavelength changes. The spectrum of the back-scattered signal is analyzed in the frequency domain. Depending on the type of spectrum analysis, FD-OCT systems are split into two categories: spectrometer based (SD-OCT) and swept source based (SS-OCT) systems. In the first case, a broad-band light source is used and the reflected signal is diffracted with a diffraction grating or a prism, and detected by a 1D detector such as a CCD (charge coupled device), or the grating spectrometer is directly used as detector. In the case of the swept source based system, the source is a frequency scanning light source, in which case a simple photo detector (photo-diode) is sufficient to capture the interference at the end of the process. In both cases, the axial resolution is limited by the spectral bandwidth of the light source.

Figure 14.b presents the typical spectrum detected for a sample with two reflective structures, which presents grooves due to the interference between reference and reflective light. The modulation frequency is proportional to the optical path difference and therefore to the distance (z_1 or z_2 on Fig. 14.b) to the coherency plane. So different grooves mean different depths of the reflective structures. Fast Fourier Transform (FFT) of the spectrum allows three components (three peaks on the FFT of the spectrum Fig. 14.b) to be found, one of which is interesting: the positive peak (in z_1 and z_2 on Fig. 14.b) gives the corresponding depth of the refractive surface – its height gives the amplitude of the back-scattered signal and its width the signal range. For a real sample, the signal is way more complex as the system captures one A-scan (the whole depth profile) at a time, but extracting positive peaks of FFT allows all the positions of the reflective structures of the sample to be found.

TD-OCT systems capture the A-scan pixel by pixel, whereas FD-OCT systems can capture one A-scan at a time. This gives the FD-OCT system a great advantage in speed and a better signal-to-noise ratio (SNR) [Drexler et al., 2014]. However, capturing the whole depth in one shot (A-scan) requires the lens to have a wide field of view to light up the whole measured depth of the sample. A compromise must be found between acquisition speed, SNR and field of view size. Today, most surgeons use FD-OCT, but this may change with the evolution of the different technologies.

2.1.2. Use of OCT in hospitals

This section is mainly based on [Ramos et al., 2009, Venkateswaran et al., 2018]. It details the main uses of OCT in clinics, especially on the cornea. Most of the figures are clinical images where the scale bar is not provided.

OCT in hospitals was first used to image the posterior chamber of the eye (especially retina) but it has proven to be a very effective tool to image the anterior chamber too, especially cornea. Ophthalmic OCT uses mainly infrared sources with wavelength typically between 800 and 900 nm for the retina and 1310 nm for the anterior chamber. With the emergence of FD-OCT systems, the scanning speed and axial resolution have increased due to the use of shorter wavelength. Commercial OCT systems achieve axial resolution of less than 5 μm for ultra-high resolution mode.

In hospitals, TD-OCT have been gradually replaced by FD-OCT systems to image anterior segments. For example it can help detect ocular surface lesion, diagnose pathologies (macular degeneration, keratoconus, tumor or retinal lesions), choose between different treatments (in particular different types of surgeries) or quantify some anterior segment parameters (such as the anterior chamber angle between the scleral spur and the iris). We will focus here on the imaging of the cornea and the detection of its pathologies, and particularly the keratoconus. Figure 15 presents a typical 2D OCT image of a normal cornea. Epithelium, stroma and endothelium are easily distinguished by the difference in contrast between the three regions of the cornea.

Detecting keratoconus

To detect Keratoconus, it is possible to use pachymetry, *i.e.* the map of corneal thicknesses over a 10 mm-diameter circle, obtained through OCT imaging. Figure 16.a presents a pachymetry of a kerato-

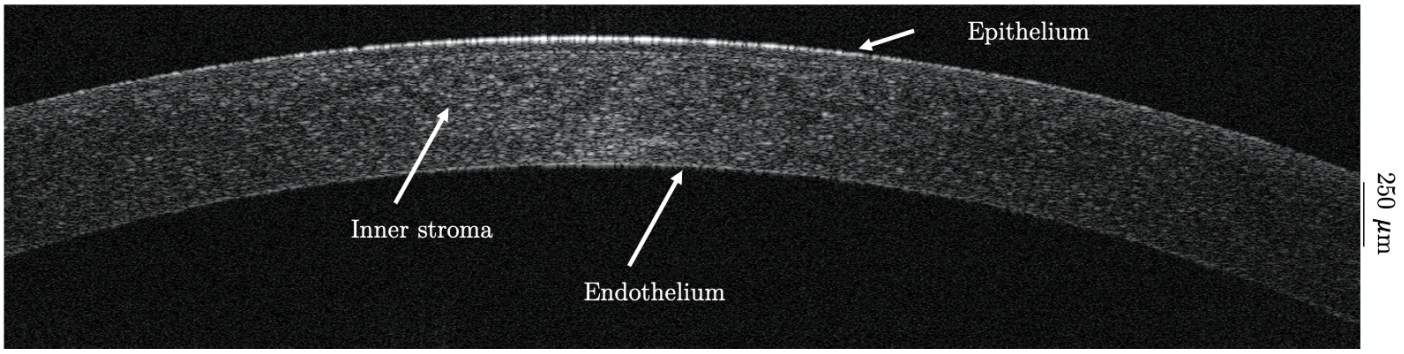

FIGURE 15. *Optical Coherence Tomography (OCT) image of a normal cornea. Scale bar: 250 μm. (kindly provided by V. Borderie from 15-20 hospital).*

conic cornea. Central thinning is detected with a minimum thickness of 422 μm in the central zone (in red) of 2 mm in diameter, which may indicate a fruste keratoconus. Figure **16**.b shows a 2D OCT scan of an other cornea presenting a scarring (the tissue appears whiter on the image in the affected area) and a thinning in the region pointed by the white arrow, also revealing a keratoconus. These two images show that pachymetry and 2D scans of corneas can be helpful to detect keratoconus.

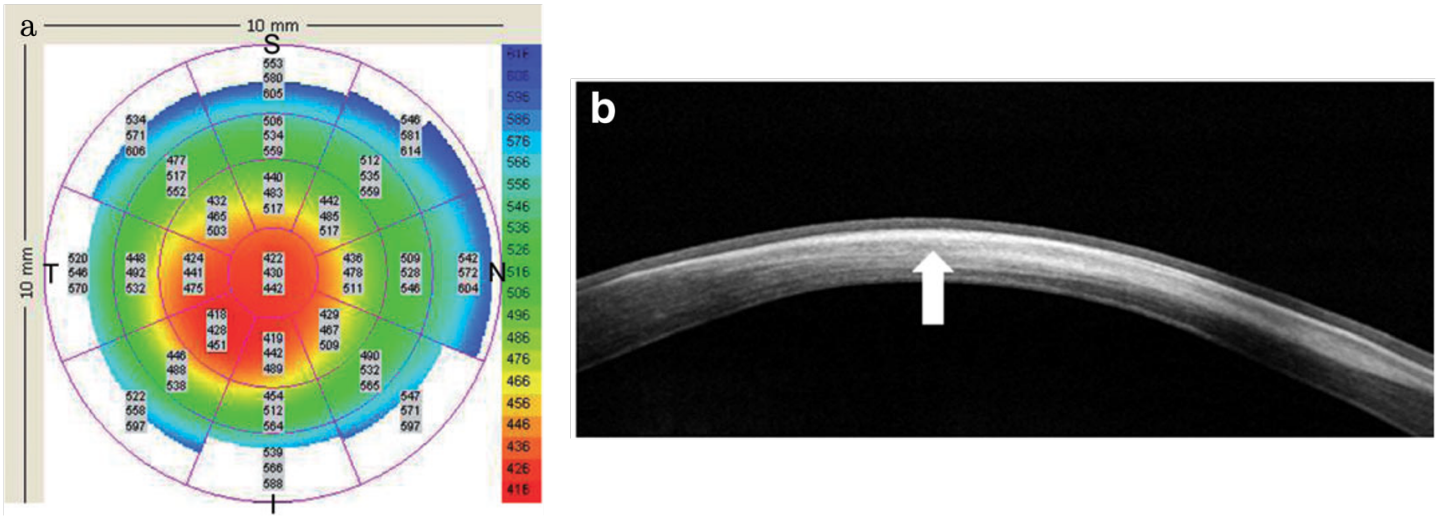

FIGURE 16. *a. Pachymetry (map of the corneal thicknesses) of a keratoconic cornea obtained using a Visante OCT (extracted from [Ramos et al., 2009]). b. OCT images of a keratoconic cornea showing a corneal scarring and thinning (arrow) (extracted from [Venkateswaran et al., 2018]).*

Treatment adaptation

Intrastromal rings Figures **17**.b–c present OCT cross-section images of keratoconic corneas after the implant of intrastromal corneal rings (Fig.**17**.a for the picture of the eye implanted with the corneal rings). Ophthalmic surgeons use those images post-operative to verify the depth and position of the implantation (Fig. **17**.c for a correct implantation). If the implants are too deep, they may perforate the anterior chamber (Fig. **17**.b) and if they are not deep enough, it may lead to serious complications on both the stroma and/or the epithelium.

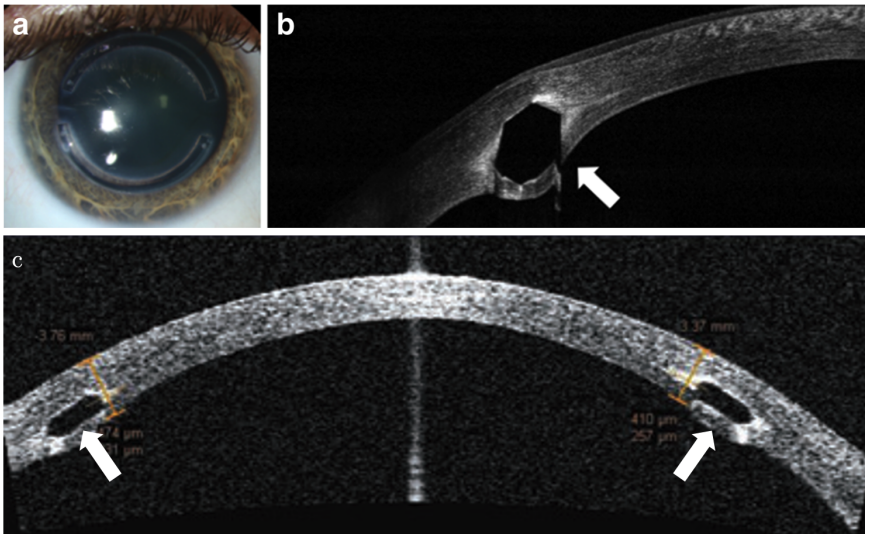

FIGURE 17. *Intrastromal ring segments. a. Photograph of intrastromal ring segments (extracted from [Venkateswaran et al., 2018]). b-c. OCT images of intrastromal ring segments (arrow) (extracted from [Venkateswaran et al., 2018, Ramos et al., 2009]).*

LASIK surgery Figures **18**.a shows an OCT scan after LASIK surgery. It shows a 198 μm flap – a cap created from the epithelium and a bit of stroma which is removed before LASIK surgery to access deeper stroma (where laser treatment is performed) and put back after the treatment – which was unexpectedly thick in this case and put the cornea at risk for ectasia. Here, OCT imaging helps the surgeon adapt the treatment rapidly. Figure **18**.b presents an OCT scan of a cornea after cross-linking treatment. The arrow points toward the demarcation line between the non-penetrated and the penetrated tissue. In this case, OCT images help measure the penetration depth of the collagen cross-linking treatment, and to study the influence of this depth on the response of the patient to the treatment.

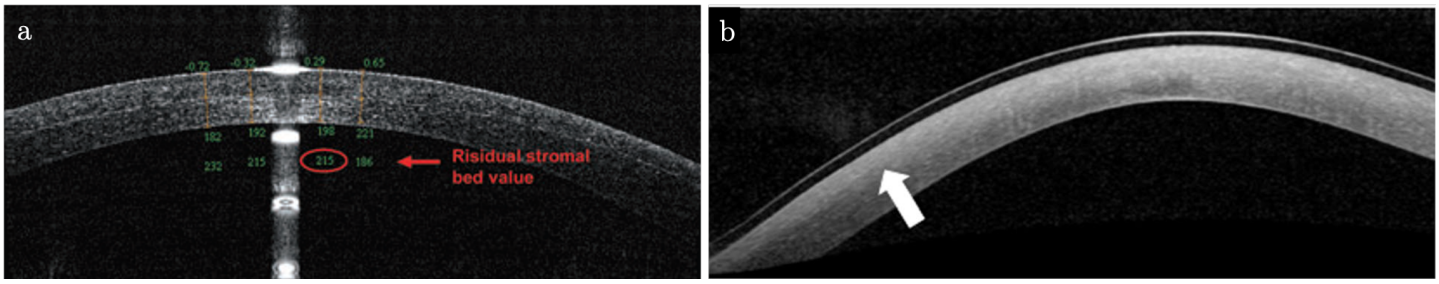

FIGURE 18. *OCT images after laser surgery and cross-linking. a. LASIK flap of 198 μm and residual stromal bed at 215 μm, (extracted from [Ramos et al., 2009]). b. Corneal haze three days after corneal collagen cross linking. The arrows point at the demarcation line in the corneal haze (extracted from [Venkateswaran et al., 2018]).*

Corneal transplant Figure **19** presents OCT scans of a cornea after keratoplasty (corneal transplant). Subfigure **19**.a shows a cornea and the graft after Descemet Stripping Automated Endothelial Keratoplasty (DSAEK), a type of lamellar transplant. The demarcation line between the graft and the original cornea is clearly visible on the OCT scan, allowing for a control of the interface and anticipating graft detachment. When the keratoplasty fails, OCT scan allows the graft edge detachment (red arrow on Fig. **19**.b) to be rapidly localized and the necessary action for the proper recovery of the eye to be taken.

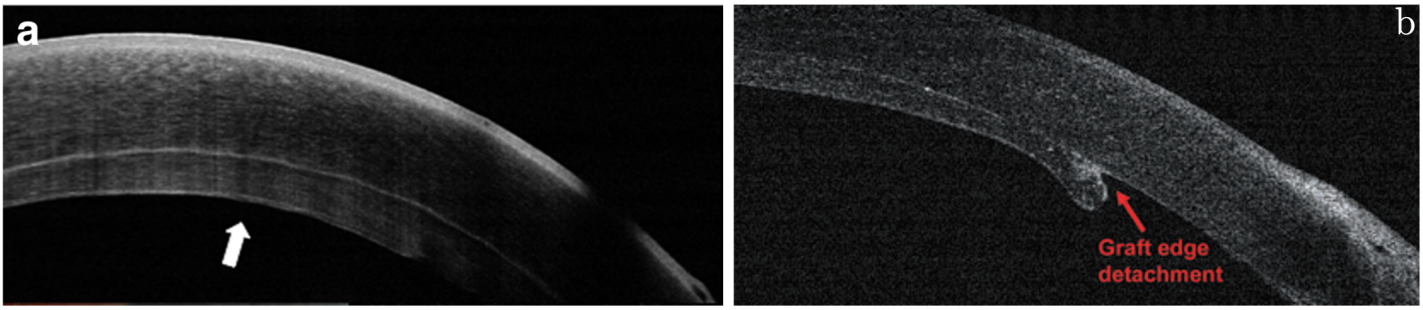

FIGURE 19. *OCT images after keratoplasty. a. Post-operative OCT image of an attached DSAEK graft (arrow) (extracted from [Venkateswaran et al., 2018]). b. OCT scan of a cornea after transplant showing a detachment of the graft (extracted from [Ramos et al., 2009]).*

Conclusion

In recent years, OCT has proven to be a very powerful tool for physicians. It allows both anterior and posterior chambers to be imaged (statically), pathologies such as keratoconus to be detected and the tissue pre- and post-operative to be imaged. The FD-OCT having a very high imaging speed, it opens a field of application on the characterization of the dynamics of the cornea in hospital. Finally, it can also be used to characterize the mechanics of the cornea using elastography coupled techniques (Sec. 3.2.2.). Although the resolution of OCT in hospitals may be lower than OCT used in the laboratory, clinical OCT images can be used to describe the geometry of a patient's cornea at physiological pressure, particularly via the pachymetry maps and especially in the case of keratoconus.

2.2. *Image analysis and strain measurement techniques*

Ophthalmologists use OCT techniques to measure and control the health of the eyes. Therefore, they produce a huge amount of images, which data are not fully exploited at the moment. New techniques, such as Optical Coherence Elastography (Sec. 3.2.2.), combining OCT with mechanical testing, have emerged to compute mechanical properties such as stiffness of the cornea. They rely mainly on two distinct types of image analysis: wavelength scanning interferometry and image correlation, introduced hereafter.

2.2.1. Phase contrast and Wavelength Scanning Interferometry (WSI)

This part is mainly based on [Ruiz et al., 2004, Chakraborty and Ruiz, 2012].

The phase contrast, or phase difference, technique is a method to compute the displacement in a material by comparing two interferogram-based images. Its suitability has been highlighted by Ruiz and colleagues [Ruiz et al., 2004, Chakraborty and Ruiz, 2012] using the technique of wavelength scanning interferometry (WSI). WSI is based on the same principles as the FD-OCT systems: a source with multiple wavelengths is used to image a sample at two different times. The source can be of different kinds: a low coherent source (like for OCT) associated with a prism, a swept source (considered the most expensive choice) or an optic splitter that divides power equally between the output channels. Interferences are

created using the different frequencies of the source. A Fourier Transform is then applied on the detected signal. Images could be then reconstructed, but it is the reconstruction of the phase between the two images $\mathbf{\Phi}$ that is interesting to determine the displacement: it gives the phase difference field $\Phi(\boldsymbol{x})$ in the direction of the light propagation. The phase difference is due to the displacement of the material, and thus Φ can be related to the displacement in the direction of the light propagation. Combining three non co-planar sources, the phase shifts can be measured in the three different directions. The displacement vector $\boldsymbol{r}$ is related to the phase difference vector through the relation $\boldsymbol{r}$: $\mathbf{\Phi} = \mathbf{S}\Delta\boldsymbol{r}$, which involves the senstivity matrix $\mathbf{S}$, which is a characteristic of the set-up (and thus can be known).

Therefore, it is possible to reconstruct displacement maps, as in Figure **20**, which presents the three components (u, v, w) of the displacement (rows) for different planes of the sample (columns) after an in-plane rotation and an out-of-plane tilt. Figures **20**.a, c, e and f show a gradient in the u and v components, which is expected from the in-plane rotation. Figures **20**.g and i present also an expected gradient from the out-of-plane tilt.

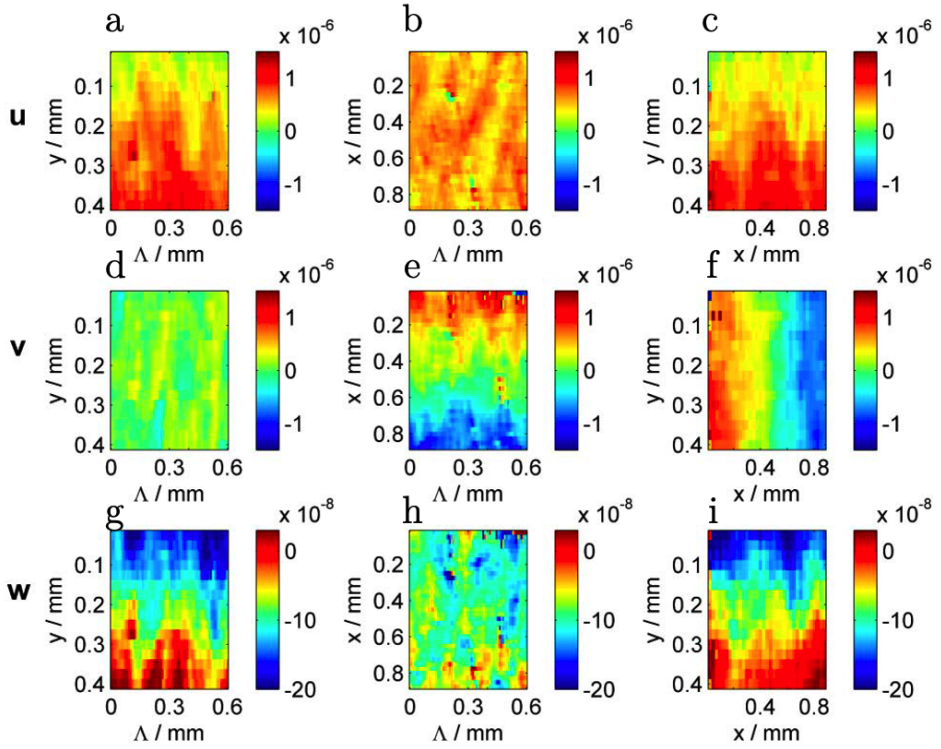

FIGURE 20. *Cross sections of the measured 3D displacement field corresponding to an epoxy sample under in-plane rotation and out-of-plane tilt. The rows indicate the three displacement components u, v, and w. The columns show sections of the data volume on different planes. Displacements are in meters (Extracted from [Chakraborty and Ruiz, 2012]).*

The same principle of phase contrast will be applied with OCT systems to compute displacement fields in the case of Optical Coherence Elastography (Sec. 3.2.2.) [Wang and Larin, 2014, Ramier et al., 2020]. However, the main method in mechanics remains the Digital Image Correlation, which is presented in the next section.

2.2.2. Digital Image/Volume Correlation (DIC/DVC)

This part is mainly based on [Pan et al., 2009, Buljac et al., 2018].

Context

Digital Image Correlation (DIC) is a commonly used technique to compute surface strain maps of a material under load. It became very popular with the evolution of digital camera technology with higher resolutions, and also with the evolution of computing power, allowing for faster computation on many images corresponding to the material loading stages. It is usually based on the tracking and matching of speckled samples between a reference and a deformed state. Figure 21 presents an example of the experimental methodology for a classical traction test on Achilles tendon (from [Luyckx et al., 2014]). First, the sample was dyed with methylene blue (Fig. 21.a). Then, it was speckled with white paint (Fig. 21.b) to give random contrast to the tissue. Finally, the longitudinal strain map was computed between two levels of load using DIC (Fig. 21.c).

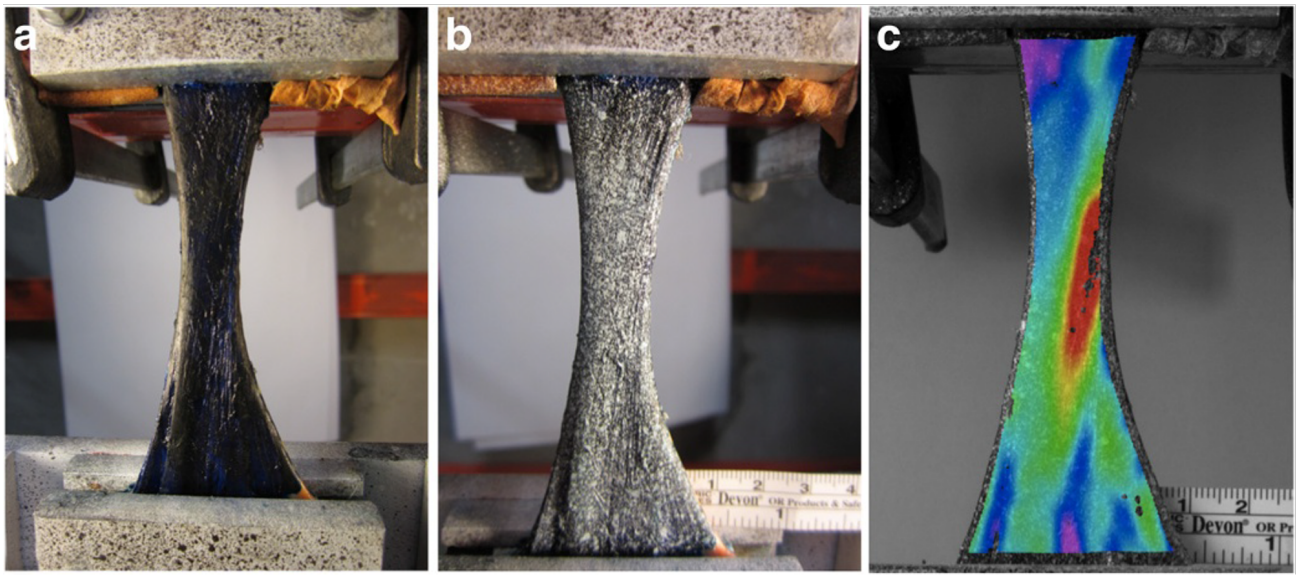

FIGURE 21. *Example of DIC on Achilles tendon. a. The Achilles tendon in the clamps dyed with methylene blue, b. speckled with white paint and c. longitudinal strain map computed by DIC (extracted from [Luyckx et al., 2014]).*

Principle

Figure 22 presents the principle of DIC. A correlation domain (framed in pink on Fig. 22) is composed of a certain number of pixels (here 9) associated with gray levels in the reference configuration. The goal is to track the evolution of this correlation domain in the deformed configuration, using the gray levels of the pixels in the so-called search domain of the deformed configuration. Denoting $f(\boldsymbol{x})$ and $g(\boldsymbol{x})$ the known gray levels of the pixels on the reference and deformed configurations respectively, image correlation relies on the existence of a displacement field $\boldsymbol{u}(\boldsymbol{x})$ such that:

$$g(\boldsymbol{x}+\boldsymbol{u}(\boldsymbol{x}))=f(\boldsymbol{x}) \tag{4}$$

with $\boldsymbol{x}$ the location of the pixel. Figure 22 illustrates an idealized, simple, case of DIC (with a simple field $\boldsymbol{u}(\boldsymbol{x})$ of a vertical displacement leading to a vertical strain), which hides the complexity that entail actual experimental setups. First, the displacement $\boldsymbol{u}(\boldsymbol{x})$ can be of any values, resulting in the need to compute the displacement at the sub-pixel scale, to allow displacements of a non-integer pixels. Then,

to have a precise computation, a large range of image gray dynamic should be used. In particular in each correlation domain and between a correlation domain and its neighbors, the gray levels must be varied enough so that the pattern can be easily recognizable between the reference and the deformed configuration. In practice, it means that the quality of the image should be sufficient and the speckling of the sample should be randomly distributed, so that the contrast of the image can be sufficient to perform the correlation. Finally, even if sub-pixel gray level computation is done and contrast is good, images are naturally noisy. Even for two images taken at the same levels of load (i.e. where $\boldsymbol{u}(\boldsymbol{x})$ should be $\mathbf{0}$), f and g are not perfectly equal and the difference between them is related to the noise coming from the experimental apparatus.

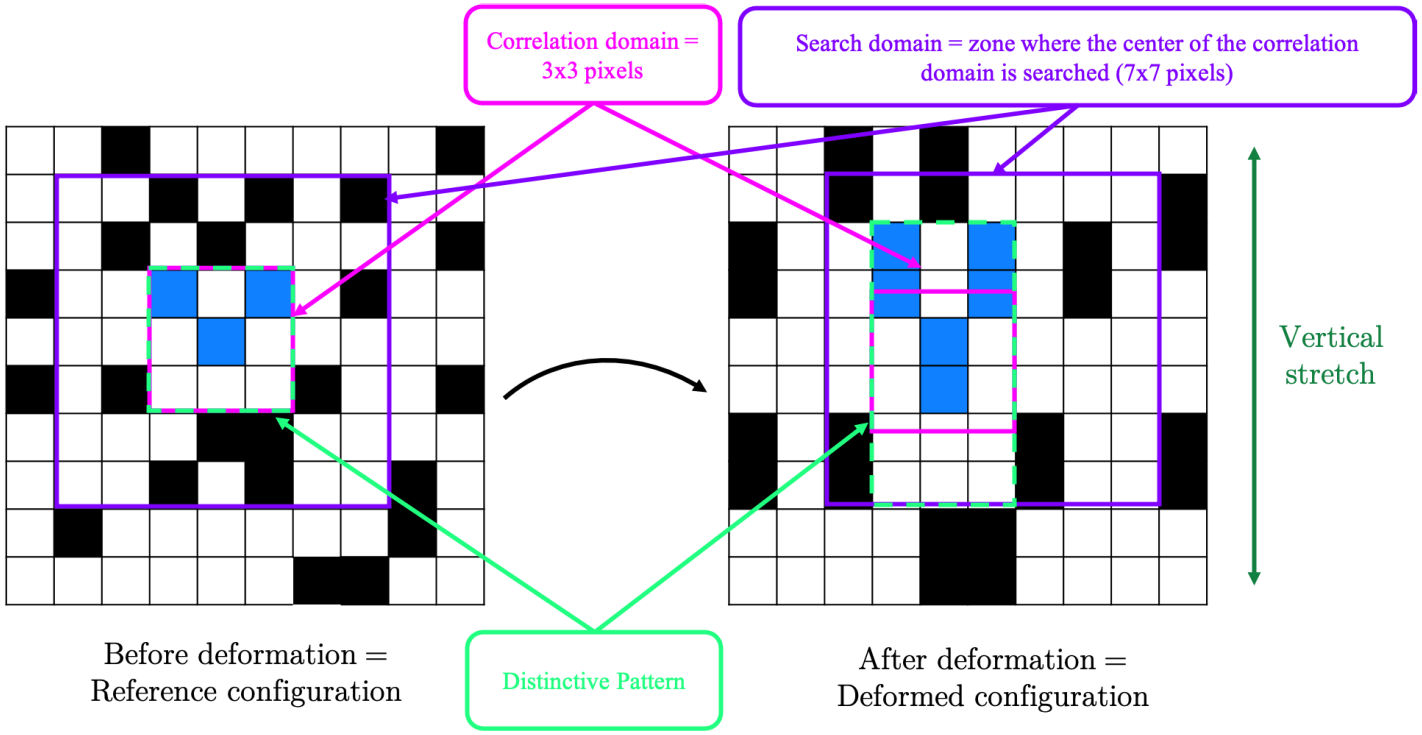

FIGURE 22. *DIC Principle. The distinctive pattern of pixels of the reference correlation domain (pink square) will be compared using gray levels and correlation criterion with the deformed configuration pack of pixels. Then the correlation domain of the deformed configuration can be computed and with it the displacement between the two configurations.*

To compare f and g taking into account these issues, a correlation criterion is created, estimating the similarity of the correlation domain of the reference configuration with the corresponding area of pixels in the deformed configuration: the center of the correlation reference domain is searched in the deformed configuration within the search domain. A typical correlation criterion on a square correlation domain of $(2M+1)$x$(2M+1)$ pixels is the zero-normalized cross-correlation criterion C_{ZNCC} defined as:

$$C_{ZNCC} = \sum_{i=-M}^{M} \sum_{j=-M}^{M} \frac{[f(x_i, y_j) - \bar{f}][g(x'_i, y'_j) - \bar{g}]}{\Delta f \Delta g} \tag{5}$$

with (x_i, y_j) and (x'_i, y'_j) the positions of the same pixel in the reference and the deformed configurations, respectively,

$$\bar{f} = \frac{1}{(2M+1)^2} \sum_{i=-M}^{M} \sum_{j=-M}^{M} f(x_i, y_j), \bar{g} = \frac{1}{(2M+1)^2} \sum_{i=-M}^{M} \sum_{j=-M}^{M} g(x'_i, y'_j)$$

the mean values of the gray levels and

$$\Delta f = \sqrt{\sum_{i=-M}^{M} \sum_{j=-M}^{M} [f(x_i, y_j) - \bar{f}]^2} \text{ and } \Delta g = \sqrt{\sum_{i=-M}^{M} \sum_{j=-M}^{M} [g(x'_i, y'_j) - \bar{g}]^2}.$$

A ZNCC criterion close to 1 corresponds to a very good correlation whereas a ZNCC criterion tending to -1 means a very poor correlation. Most DIC softwares allow a minimal acceptable value for the correlation criterion to be given, to consider that the correlation is good enough.

Local and global DIC

Local DIC consists in correlating each correlation domain between its reference state and its deformed state. A global DIC consists in looking at the region of interest as a whole. One of the main advantage is that it ensures the continuity of the measured displacement. Also a regularization process can be added when looking at materials for which there is an a priori on the displacement. Local DIC/DVC has advantage of being determined at a controlled scale, without regularization or *a priori* on the material behavior. Although one can try to point strength/weakness of each method, both are used intensively in mechanics. We are going to present here the local approach, which is simpler to explain.

From DIC to DVC

DIC is a surface method applied to 2D images. Historically, only such images provided enough contrast (due to the speckling for example). With the emergence of 3D imaging techniques in the 2000s however, such as X-ray tomography [Bay et al., 1999] or OCT [Fu et al., 2013], 3D images of materials with internal contrast are now available. The methodology of DIC can then be easily transposed to the third spatial dimension. Pixels become voxels, DIC becomes Digital Volume Correlation (DVC) and 2D cross-correlation algorithms become 3D. Similarly, WSI can be done in 3D. Thus, both offer the possibility to characterize the response of a material to loads. The use of 3D instead of 2D is interesting for complex materials, such as collagen-rich tissues (muscle, tendon, cornea...): the full deformation tensor can be measured. While WSI is more commonly used in optics laboratories, DVC is well implemented in the mechanics field.

Figure **23** presents the typical results for 3D displacements (A-C), 3D normal strain (D-F) and 3D shear strains (G-I) of chicken breast tissue under vertical compression obtained by DVC on 3D SS-OCT images [Meng et al., 2019]. During the test, muscle fibers were aligned along the x-direction. Results show an anisotropy in the mechanical deformation of the breast tissue: linear reduction along the z-direction, diagonal linear distribution along the x-direction and a near linear distribution along the y-direction.

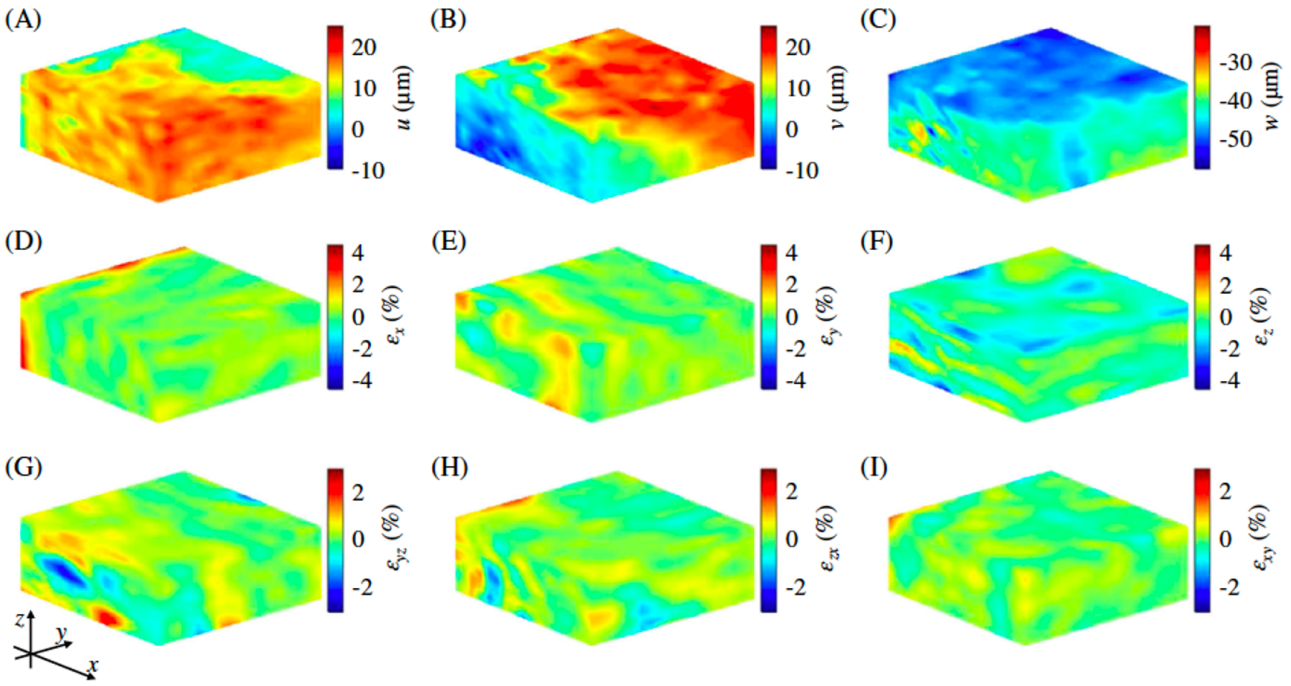

FIGURE 23. *Example of DVC on SS-OCT images of chicken breast tissue under vertical compression (6mm in both the width and lenght directions were scanned). (A-C) the 3D displacements in the x, y and z directions, respectively, (D-F) the 3D normal strains ε_x, ε_y and ε_z in the x, y and z directions respectively and (G-I) the 3D shear strains ε_{yz}, ε_{zx} and ε_{xy} (extracted from [Meng et al., 2019]).*

3. Mechanical characterization of the human cornea

In order to model the response of the cornea to pressure, one needs values for the mechanical parameters of the tissue, such as stiffness, viscous modulus... To do so, one of the newest experimental approach is called Elastography. It can be defined as any imaging process allowing to extract elasticity or stiffness of a material. It usually couples a mechanical exciter to create a perturbation in the tissue, with an imaging apparatus to measure the induced perturbation. Finally, to extract the mechanical properties of the material, one needs a model of the tissue (*i.e.* a constitutive law).

Even though it is usually easier to perform mechanical tests *ex-vivo* (repeatability of experimental conditions, sampling, availability of samples and the experimental apparatus, larger range of experimental conditions...), the cornea is a tissue that has the advantage of being accessible *in-vivo*. As a result, although the classical characterization tests of healthy tissues are usually performed *ex-vivo*, the characterization of pathological corneas can be done *in-vivo* thanks to new elastography techniques, which compare their properties with healthy ones.

3.1. *Ex-vivo mechanical characterization of cornea*

This section presents the most common tests performed *ex-vivo* on corneas to measure and characterize the mechanical properties of the tissue. The inflation test is the experiment that mimics best the physiological action of pressure on the cornea. Strip extensometry has been used for decades to measure Young's modulus of all types of materials. Nanoindentation and acoustic radiation force elasticity microscopy

(ARFEM) are two more recent techniques for the evaluation of the Young's modulus, the latter having the advantage of being non destructive. Note that many of these tests apply only a small deformation of the tissue, leading to a linear relation between applied stress and strain. So, they can determine only a "tangent modulus", which is generally called Young's modulus.

3.1.1. Inflation test

Principle of the method

The inflation test is an experimental method to characterize the mechanical properties of cornea. It mimics the action of intraocular pressure on the tissue. Elsheikh and coauthors have studied the mechanical properties of porcine and human corneas using the experimental apparatus represented in Fig. **24** [Elsheikh and Anderson, 2005]. The cornea is attached to a pressure chamber by the sclera, and saline solution is injected under the cornea via the pressure chamber to put the tissue under pressure. The pressure in the chamber is monitored using a pressure sensor and the displacement of the apex of the cornea is measured via a laser displacement sensor. The biomechanics of the cornea is then analyzed using the pressure versus apex displacement curve.

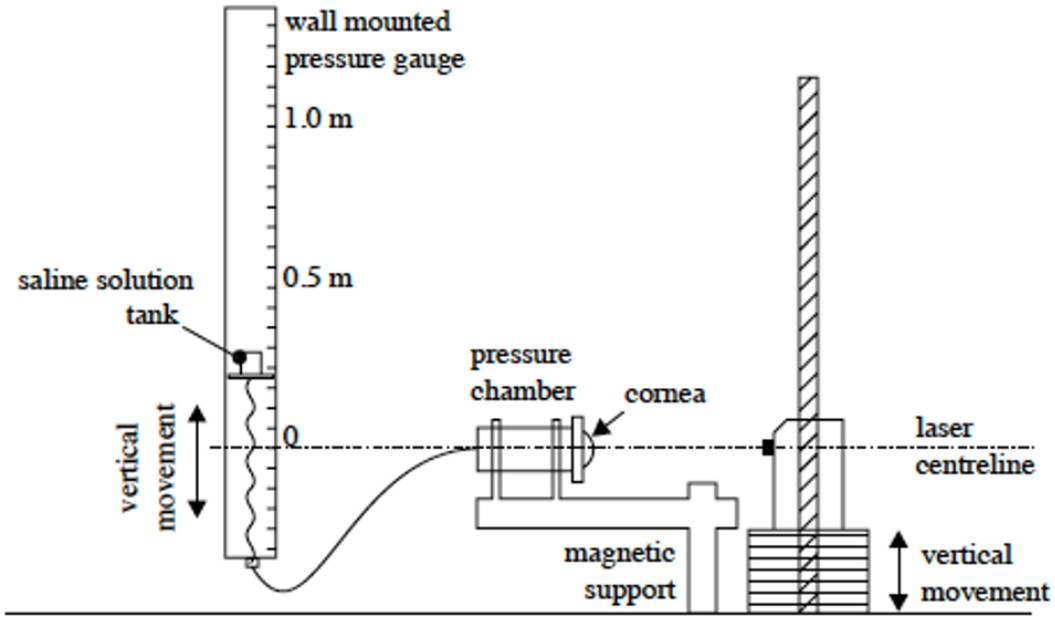

FIGURE 24. *Schematic view of the different components of the inflation test (extracted from [Elsheikh and Anderson, 2005]).*

Main results

Figure **25** presents the pressure with apical rise curves for six human corneas [Elsheikh et al., 2008]. At low pressure (under approximately 15 mmHg), the cornea exhibits a low stiffness. Then, with the increasing pressure, a sudden change of stiffness appears. Elsheikh and Anderson explain these two regimes by a domination of the mechanical response by the matrix (of low stiffness) at low pressure, and a domination by the collagen lamellae (high stiffness) at higher pressures [Elsheikh and Anderson, 2005].

Such behavior is similar phenomenologically to the mechanical response of other collagen-rich tissues as tendon, skin or aorta [Fratzl et al., 2008].

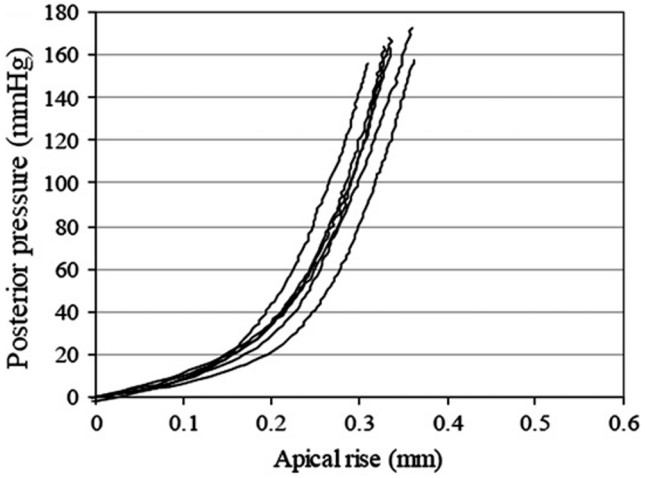

FIGURE 25. *Pressure with apical rise during inflation test for 6 human corneas (from [Elsheikh et al., 2008]).*

In the same article [Elsheikh et al., 2008], the authors also show that porcine and human corneas do respond the same way to pressure (low stiffness at low pressure and sudden change of stiffness at higher pressure) but that human corneas are stiffer than porcine ones, and also that human corneas stiffen with age.

Although the article of Elsheikh *et al.* proposes a first global mechanical behavior of the cornea using the displacement of the apex, it may seem reductive to consider that the whole biomechanics of the cornea is governed by what happens at the highest point, in particular in view of the complex microstructure. That's why other groups – particularly Boyce and coauthors [Boyce et al., 2008] – measured the displacement of the whole anterior surface of the cornea by stereo-correlation (a 3D displacement field measurement of a surface). Figure **26**.a presents the results for the out-of-plane displacement (in the z-axis direction of Figure **26**.a) at a particular pressure (60 mmHg). Figure **26**.b presents the results for the out-of-plane displacement for various location over a loading cycle. Those maps show that the out-of-plane displacement is homogeneous for the central part of the bovine cornea at 60 mmHg and also relatively homogeneous over the loading cycle (the displacement at the different locations is similar).

It confirms that one could consider the apex displacement as a proxy for the anterior surface displacement of the cornea, at least for bovine eyes, when the surface geometry is known. But there is still a lack of information on the material behavior through thickness. Fu [Fu, 2014] tried to tackle this issue by measuring full-field displacement and strain maps using digital volume correlation (DVC) on OCT images of porcine corneas during an inflation test between 2 and 2.5 kPa (15–18.75 mmHg).

Figure **27**.a shows displacement maps for a variation of pressure from 15 to 18.75 mmHg. The order of magnitude of the vertical displacement u_y at the apex of the cornea seems to be in agreement with the apex displacement found by Elsheikh *et al.* [Elsheikh et al., 2008], *i.e.* approximately 0.01 mm. Figure **27**.b shows the associated strain maps. A clear contraction (approximately -2% of ε_{yy} strain) can be observed at the center of the cornea along the vertical direction (y-axis), while the cornea inflates in the peripheral zone (of approximately 2% also). ε_{xx} strain maps show a extensional deformation along the x-axis and clear heterogeneity between the anterior and posterior parts (almost all of the deformation

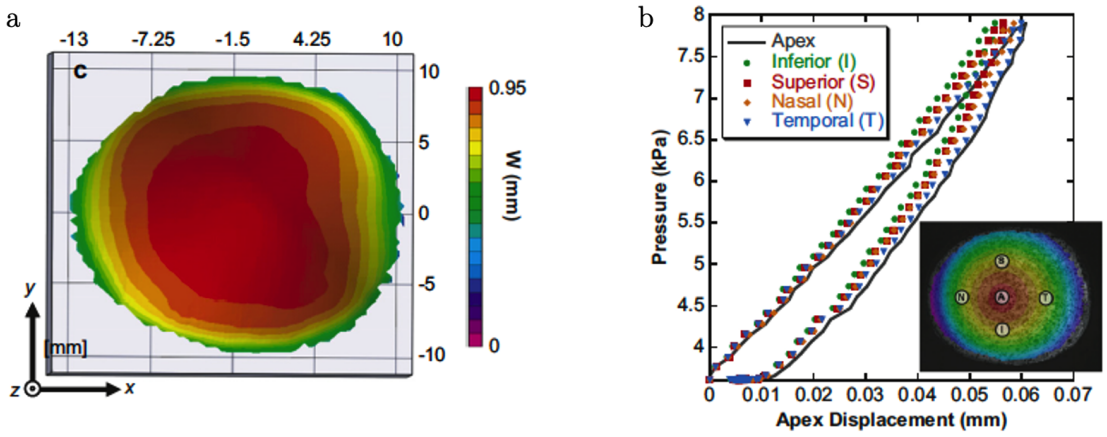

FIGURE 26. *a. Typical out-of-plane displacement at a pressure of 8 kPa (60 mmHg) for bovine cornea. b. Typical out-of-plane displacement at different locations during a loading cycle over a pressure range of 3.6–8.0 kPa (27–60 mmHg). (Both images are extracted from [Boyce et al., 2008]).*

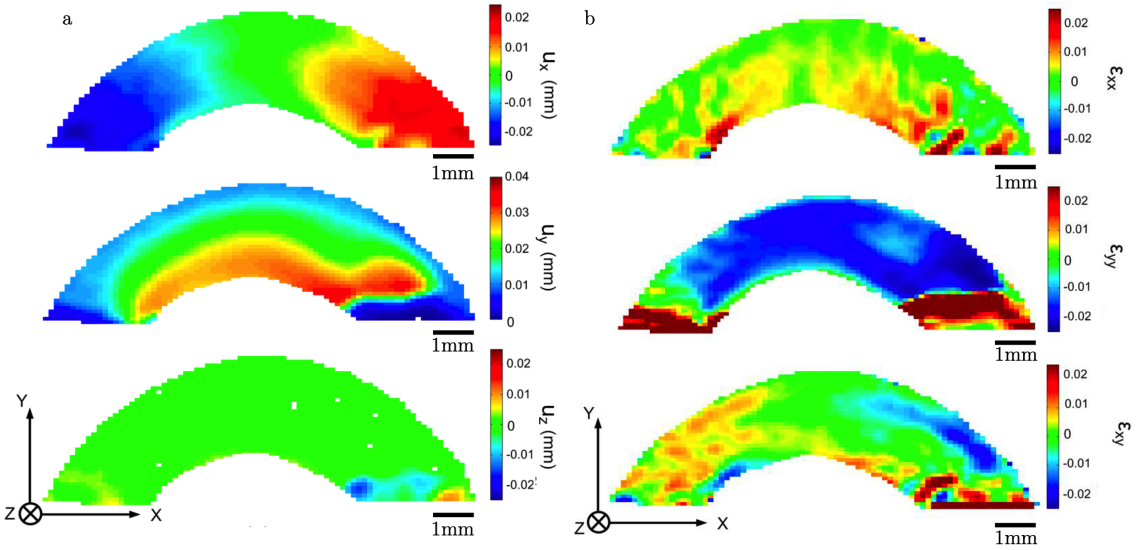

FIGURE 27. *a. Displacement and b. strain maps measured with DVC for the central z-slice of a porcine cornea under pressure from 2 to 2.5 kPa (15 to 18.75 mmHg) (extracted from [Fu, 2014] – Scale bar: 1 mm).*

appears in the posterior stroma) while the cornea is submitted to shear strain in the periphery (and mostly on the anterior part of the cornea), which may be due to the computation of the strain in Cartesian while the cornea is curved (and thus would have a rather radial deformation).

Keratoconic corneas and treatment

To our knowledge, there is no mechanical characterization of a whole human cornea (healthy or pathological) using inflation tests.

To test the effect of the cross-linking treatment, inflation tests have been performed on porcine corneas treated with a riboflavin solution (see Sec. 1.3.). Kling *et al.* [Kling et al., 2010] used a Scheimpflug corneal three-dimensional topographer (similar to an ultrafast OCT limited to 2D acquisition) to image the cornea. The Young's modulus was determined using the classical Laplace's law for the stress $\sigma = Rp/2d$ (with R the mean radii of curvature, p the applied pressure and d the corneal thickness) and $\varepsilon = \Delta R/R$ for the strain. They show that the Young's modulus in a cross-linked cornea is significantly higher (1.10 ± 0.30 kPa) than the one found in non-cross-linked eyes (0.69 ± 0.30 kPa). They also show that the cross-linking treatment influences the thickness of porcine corneas, especially 24 hours after the treatment. A strong dehydration was observed on porcine corneas with classical hyperosmolar riboflavin instillation, while swelling occurred for hyposmolar riboflavin treatment. In another study, Chang *et al.* [Chang et al., 2020] found that the shear modulus μ at a stress of 0.03 MPa shows an increase of $43\% \pm 24\%$ in a cornea treated by cross-linking with respect to non-treated porcine corneas. One can conclude that the cross-linking process tends to stiffen the tissue and also to influence the thickness of the cornea.

3.1.2. Strip extensometry

Principle of the method

Strip extensometry is one of the most classical experiments designed to obtain mechanical properties of a material and especially the Young's modulus, which is obtained from the slope of the stress-strain curve as $E = \sigma/\varepsilon$ (with σ the axial stress and ε the axial strain). Elsheikh and Anderson [Elsheikh and Anderson, 2005] have performed tensile tests until rupture on porcine cornea while Boyce *et al.* have carried out creep tests on bovine cornea [Boyce et al., 2007]. Figure **28** presents the experimental apparatus used by Boyce *et al.* (Fig. **28**.a–d) and by Elsheikh and Anderson (Fig. **28**.e–f). They both cut a strip going through the apex diagonal out of a cornea (bovine and porcine respectively) and applied uniaxial load on the coupon.

Main results

Figure **29** presents the stress-strain curve (a and c) and the load-extension curve (b) of the strip extensometry tests. In all the cases, the non-linear responses with two regimes is obtained, similar to the inflation test response. Figure **29**.c shows the comparison between the averaged stress-strain curve for strip extensometry and inflation tests on porcine corneas. Strip test has a shorter first regime (of large stretch at low stress) than the inflation test. Then the second part (large stress for large stretch) seems

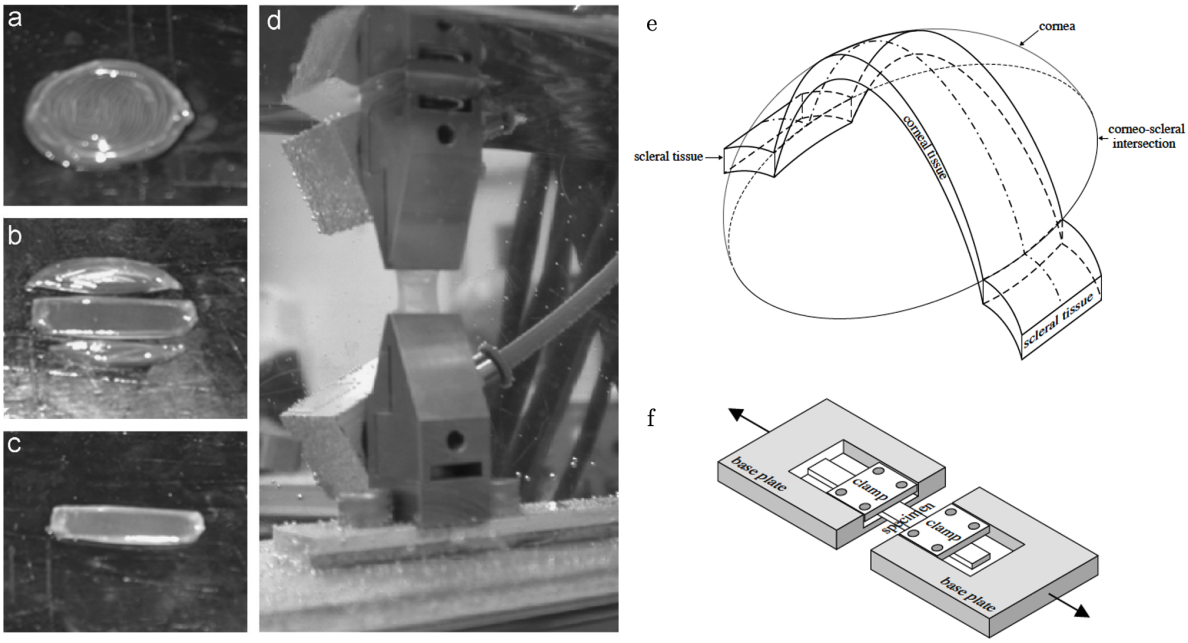

FIGURE 28. *a-d. Experimental apparatus used in (and extracted from) [Boyce et al., 2007]. a. Bovine cornea, b. and c. cut of the strip and d. tensile test. e. Schematic of the specimen and f. the strip extensometry test rig used in (and extracted from) [Elsheikh and Anderson, 2005].*

much more similar in term of rigidity.

Even though the stress-strain curves of the strip extensometry tests have a similar shape to those of the inflation test, three sources of errors due to the geometry of the cornea can be identified in the strip test. First, the cornea being almost spherical, the length of the anterior and posterior surfaces of the strip are not equal and so the usual area used has to be adapted to compute the Young's modulus [Elsheikh and Anderson, 2005] to take into account the non uniform stress distribution. Second, the corneal strip is flattened, so its initial curvature has to be taken into account in the computation of the Young's modulus, especially for pre-strain (extensional strain in the posterior surface and contractile strain in the anterior surface). Finally, the thickness is not homogeneous along the strip (the cornea is thinner in the central part than in the periphery) and this third geometrical effect has to be considered in the computation of the area. Anderson and Elsheikh [Elsheikh and Anderson, 2005] have built a model to correct the results of the strip extensometry test to match the inflation test results (the difference between the two sets is reduced to 5% in average) so that future work on the characterization of the mechanical properties of the cornea can be done using strip extensometry. Other sources of difference may be important, as the heterogeneity of stretch in the inflation test, contrary to the strip test, and so on.

Keratoconic corneas and treatment

In the case of pathological corneas, there is only a few studies of strip extensometry comparing the Young's modulus of healthy and keratoconic human corneas. Andreassen and his colleagues [Andreassen et al., 1980] have shown that the Young's modulus of a keratoconic cornea is significantly lower than the one of a healthy cornea. However, Nash *et al.* [Nash et al., 1982] shows that this assertion is true for high level of stress but not at physiological pressure, where no significant difference is

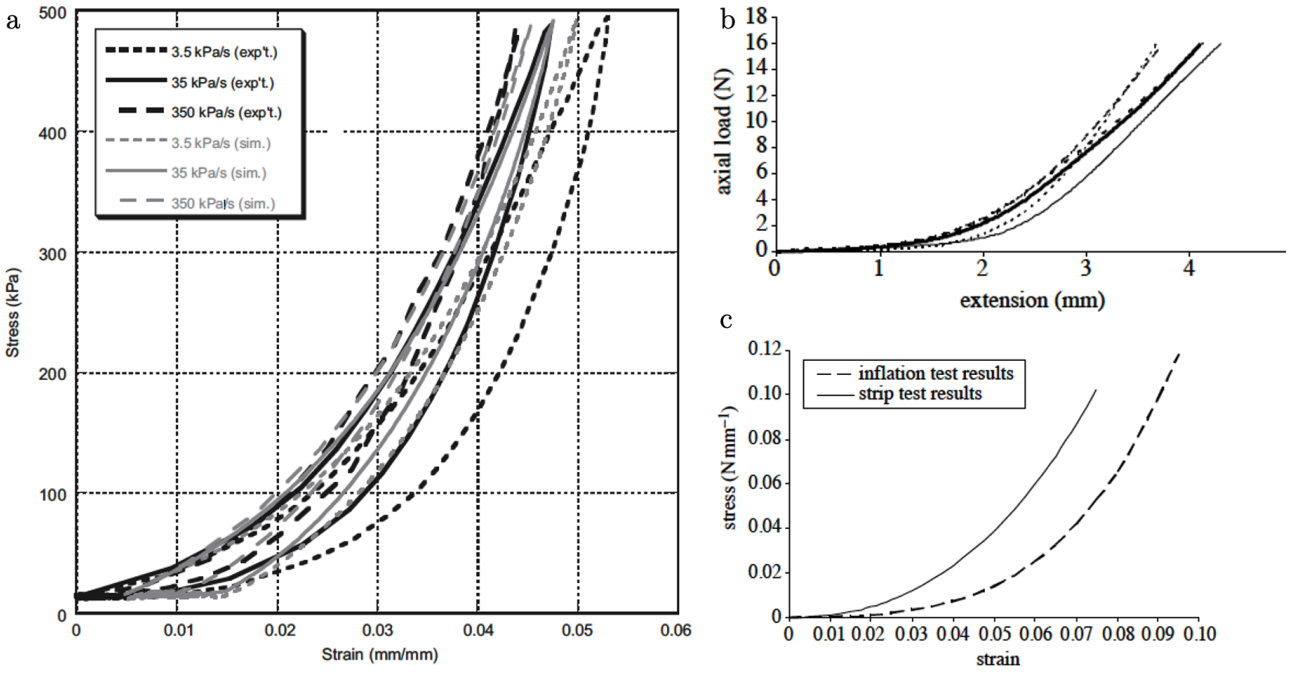

FIGURE 29. *a. Average tensile stress–strain response of bovine cornea tissue in the naso-temporal orientation at each of three different strain rates (extracted from [Boyce et al., 2007]). b. Load-elongation behavior of a selection of strip tests on porcine corneas and c. Material constitutive relationship obtained using both inflation and strip tests on porcine corneas (extracted from [Elsheikh and Anderson, 2005]).*

found between healthy and pathological corneas. Finally, Spoerl *et al.* [Spoerl et al., 1998] studied very early the effect of cross-linking by using strip extensometry on treated and non treated porcine specimen and showed that the cross-linking resulted in an increased stiffness. More recently, Wollensak *et al.* [Wollensak et al., 2003] performed extensometry tests on human and porcine corneas and showed that the Young's modulus was higher when the corneas have been treated with riboflavin (4.5 higher and 1.8 higher, respectively).

3.1.3. Nanoindentation

Principle of the method

The test of indentation consists in penetrating a tip (the indenter) in a flat surface of the tested material, and monitoring the height of penetration (h in Fig. **30**) as a function of the applied load (P on Fig. **30**). The mechanical properties – such as hardness – can then be determined.

Main results

Dias and Ziebarth [Dias and Ziebarth, 2013], and Last *et al.* [Last et al., 2012] measured the Young's modulus of corneal stroma using atomic force microscopy (AFM) as nanoindentor. Dias and Ziebarth found that the posterior stromal elasticity is 39.3% of the anterior stromal elasticity, with an anterior Young's modulus of 281 $\pm$ 214 kPa. Last *et al.* , on their side, measured an anterior stromal Young's

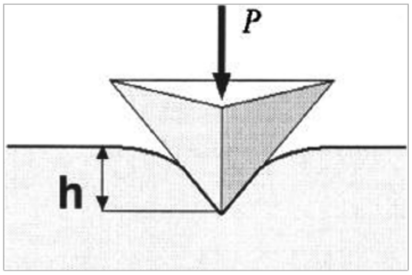

FIGURE 30. *The principle of nanoindentation (extracted from [den Toonder et al., 2005]).*

modulus of 33.1 $\pm$ 6.1 kPa. The difference in the order of magnitude may come from experimental protocols, especially the preparation of the exposition of the anterior stroma. Eberwein and coauthors [Eberwein et al., 2014] used an indenter (called Bioindenter) to measure the properties of cornea, limbus and sclera. Figure **31** presents the typical force with displacement curve obtained on the three tissues. Young's modulus measured was approximately 19 kPa for the central cornea, 10k Pa in the limbal region and 17 kPa in the scleral region.

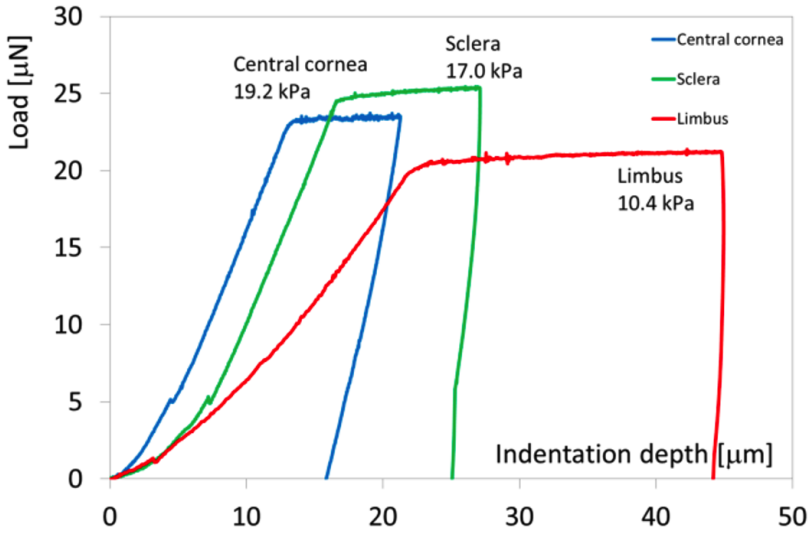

FIGURE 31. *Typical force with displacement curves obtained using nanoindentation for the cornea (blue), the limbus (red) and the sclera (green) (extracted from [Eberwein et al., 2014]).*

Keratoconic corneas and treatment

The same groups used nanoindentation to measure the elasticity of healthy corneas after cross-linking. Dias *et al.* [Dias et al., 2015] showed that porcine corneas treated with riboflavin were stiffer and less viscous than the control ones. Nohava *et al.* [Nohava et al., 2018] used the Bioindenter on human corneas and measured that the stiffness of the central cornea is two times higher after riboflavin treatment. In both articles, the authors show that the region of higher stiffness is centered around the riboflavin application and does not extend significantly towards the periphery.

3.1.4. Acoustic Radiation Force Elasticity Microscopy (ARFEM)

One of the most recent techniques used to measure the mechanical properties of the cornea (and other soft tissues) is the acoustic radiation force elasticity microscopy (ARFEM). Figure **32** presents the setup used in Mikula *et al.* [Mikula et al., 2014, Mikula et al., 2018]. Details of the experimental apparatus can be found in [Mikula et al., 2014]. Only the main components are described below.

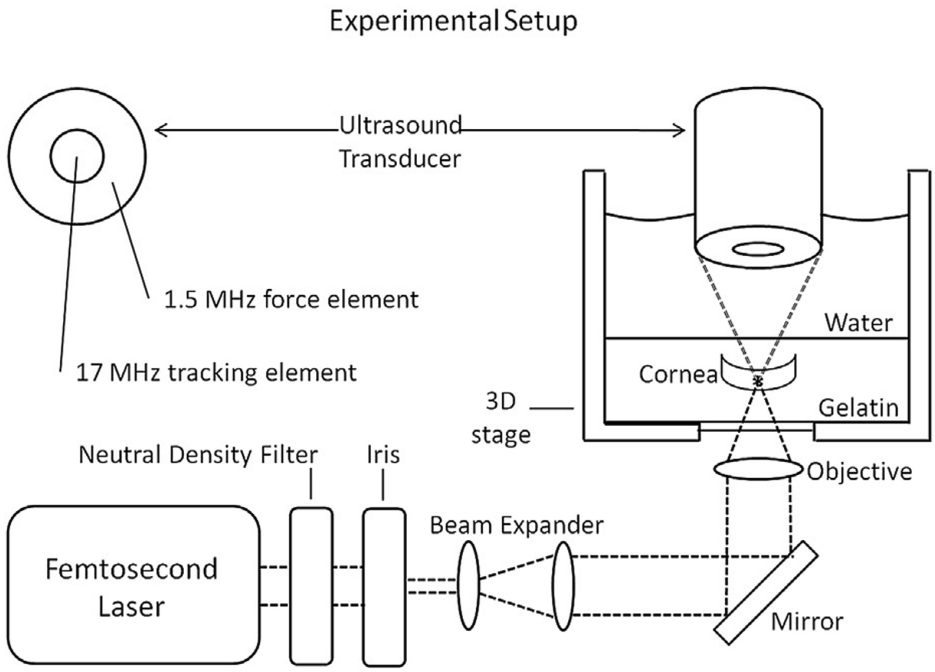

FIGURE 32. *ARFEM setup (extracted from [Mikula et al., 2014]).*

A femtosecond laser generates a micro-bubble inside the sample with one pulse. Then an acoustic force (low-frequency, high-intensity) displaces the bubble while an ultrasound probe (high-frequency, low-intensity) monitors the displacement of the bubble. The Young's modulus is related to the displacement of the bubble using the following relationship [Mikula et al., 2014]:

$$E = Ia/2cx_{max}, \tag{1}$$

where I is the acoustic intensity, a the bubble radius, c the speed of sound in the medium, and x_{max} the maximum displacement of the bubble.

With this technique Mikula *et al.* managed to measure the Young's modulus in healthy [Mikula et al., 2016] and keratoconic [Mikula et al., 2018] corneas. They found that the anterior central part is stiffer (E = 4.2 $\pm$ 1.2 kPa and E = 1.67 $\pm$ 0.44 kPa for healthy and keratoconic corneas, respectively) than the posterior central part of the cornea (E = 2.3 $\pm$ 0.7 kPa and E = 0.97 $\pm$ 0.3 kPa for healthy and keratoconic corneas, respectively). They also show that keratoconic corneas are significantly less stiff than healthy tissues.

3.1.5. Summary of *ex-vivo* mechanical characterization without microscopic imaging

To conclude, although all these techniques give quite different results in terms of numerical values, significant trends emerge with respect to *ex-vivo* measurements.

Figure 33 presents a summary of the previous results on characteristic stiffness measured using the different techniques presented, which definition varies across experiments (see Table 3.1 at the end of this section for a summary of all mechanical measures). First, in all cases, porcine corneas (in pink on Fig. 33) are globally less stiff than human corneas (in blue on Fig. 33). Then, keratoconic corneas (△ on Fig. 33) are significantly softer than healthy tissue (□ on Fig. 33), but cross-linked corneas (⬡ on Fig. 33) are significantly stiffer than healthy tissue. The lack of rigidity of pathological corneas can thus be counterbalanced by the increase of stiffness brought by cross-linking treatment. Finally, anterior stroma (middle blue and pink) is stiffer than posterior stroma (light blue and pink) either for humans and pigs. However, no study compared the measure on the whole cornea to those on anterior and/or posterior parts only.

Based on Figure 33, we conclude that it is difficult to choose a single value for a given mechanical property of the cornea. The scatter across the results available in the literature is very large: the scale of Figure 33 being logarithmic, the range of possible values comprises almost four orders of magnitude for human corneas. Furthermore, it shows that there are discrepancies between the anterior and posterior parts and that local information on the whole organ is therefore missing.

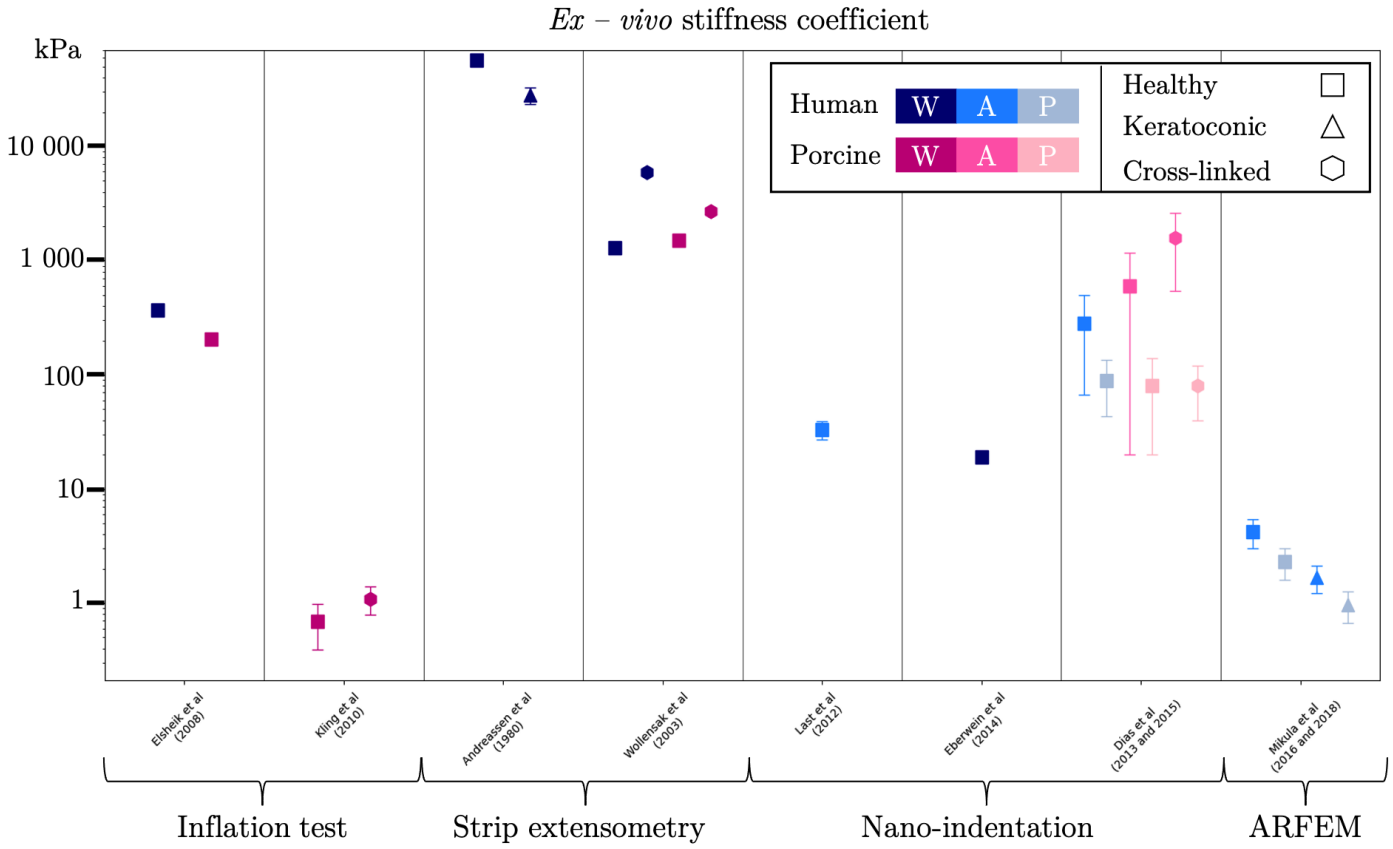

FIGURE 33. *Ex-vivo measured corneal stiffness coefficient using the different methods previously presented: inflation test (Sec. 3.1.1.), strip extensometry (Sec. 3.1.2.), nano-indentation (Sec. 3.1.3.) and ARFEM technique (Sec. 3.1.4.). Notation: W = whole cornea, A = anterior stroma, P = posterior stroma.*

The inflation test is the most physiological one. It has enable to show that (i) the cornea presents two very distinct regimes of mechanical responses depending on the applied pressure, (ii) cross-linking can be a suitable treatment approach for keratoconus because it stiffens the weakened pathological corneas.

However, the characterization remains limited at the moment, with partial measures of the stretch: at best on the external surface but generally limited to the apex displacement, despite the complexity of the tissue and of the imposed loading.

Strip extensometry is easier to perform. However, the naturally-bend shape of the human cornea make its analysis quite complex: the transition from plane properties (of the strip) to 3D properties (of the half-sphere) is not obvious. On top of that, these assays have been limited to strip going through the cornea apex. So, they may miss the effect of the heterogeneity in the lamellae distribution. That is why this test has become less popular recently.

Nano-indentation and ARFEM are recent techniques that allow direct measurements of the Young's modulus of the anterior and posterior cornea. They have the advantage of being in principle quite simple to implement, and not very invasive than. They also allows to test the cornea at different depths, working on cutted tissues. However, they are limited to small deformations, which means that only Young's modulus can be determined and not the full non-linear stress-strain curve. Also, they are very sensitive to the preparation of the surface (flatness, humidity, *etc*.); This explains partly the high variability in their results.

3.1.6. Mechanical testing coupled with imaging of the microstructure

Two founding papers have studied the response of the cornea to mechanical load whilst imaging the microstructure: one using Second Harmonic Generation (SHG) microscopy coupled with inflation test [Benoit et al., 2016] and one using X-ray diffraction coupled with strip extensometry [Bell et al., 2018]. In these papers, macroscopic strains are compared to the distribution of the lamellae during the mechanical tests.

Macroscopic strain response

Figure **34**.a.1 presents the scan positions used for the X-ray analysis and Figure **34**.b.1 the different volumes of interest for the SHG study, in particular Stack#2 (2PEF) that was used to perform the strain analysis.

Figures **34**.a.2 and b.3 present the local strain results measured by DIC. Figure **34**.a.2 shows the computed parallel strain on the strip cut along the vertical meridian at 5% of strain during tensile test [Bell et al., 2018]. Figure **34**.b.3 illustrates the strain on the corneal surface between the loading steps of the inflation test along the two preferential directions of the collagen lamellae φ_1 and φ_2 presented in Figure **34**.b.2 [Benoit et al., 2016]. Figure **34**.a.2 shows a relatively symmetric distribution of strain with respect to the center of the sample with a bigger parallel strain in the center (around 7%) than in its closest periphery (around 3-4% at positions of 6 and 10 mm). The end of the strip is subject to higher strain, up to 10%. Normal strain maps (ε_{11} and ε_{22} in Fig. **34**.b.3) and shear strain maps (ε_{12}) show, respectively, the progressive stretching and shearing of the cornea along dominant orientations with increasing pressure. The strain appears rather uniform, leading to homogeneous deformations at the sub-millimeter scale.

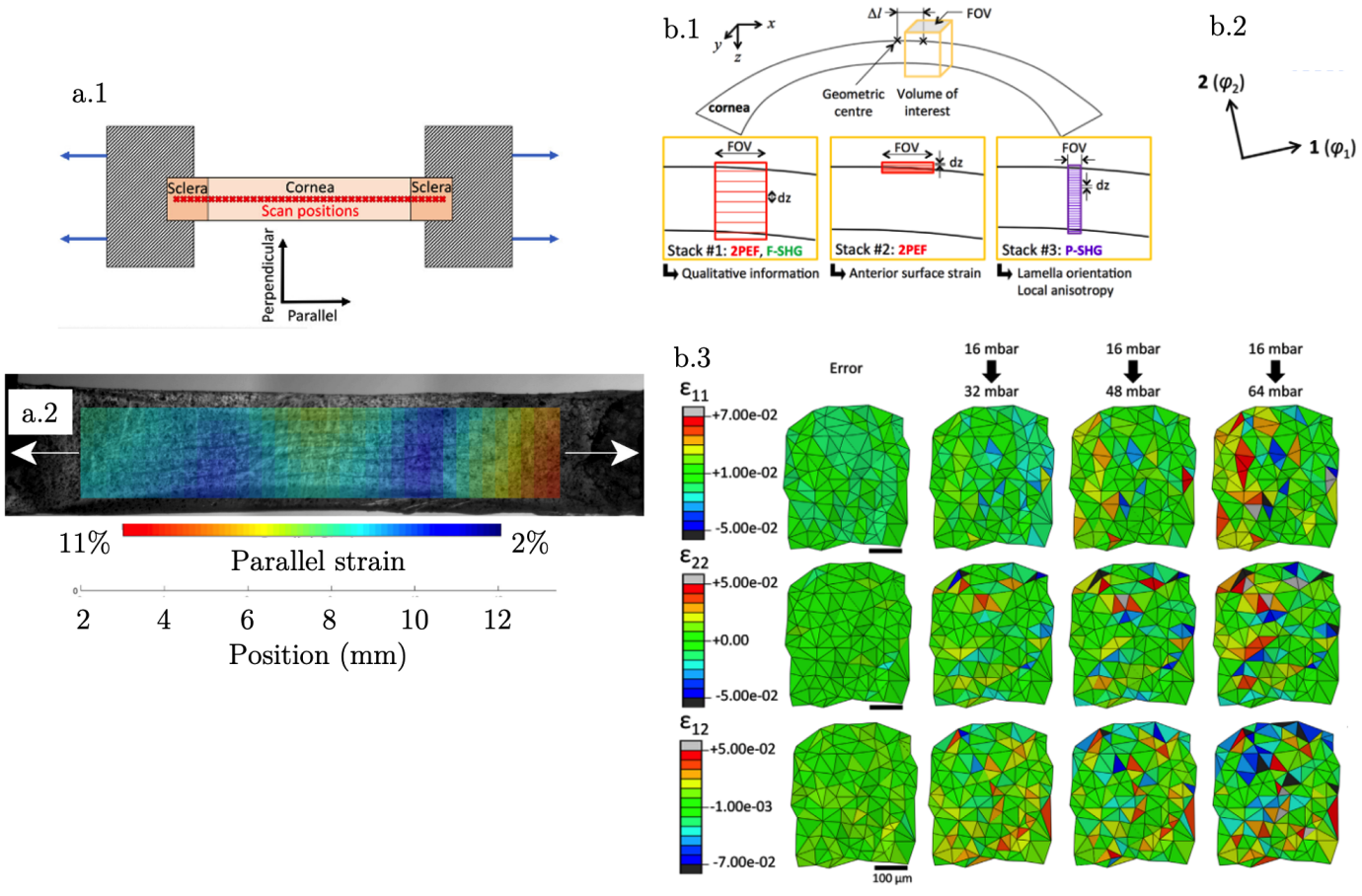

FIGURE 34. *a.1. Scan positions used for the X-ray analysis during tensile test. a.2. Parallel strain computed by DIC at 5% of strain – scale bar 11% (red) to 2% (blue) (extracted from [Bell et al., 2018]). b.1. Volumes of interest considered in the SHG study. b.2. Main direction of the lamellae used to compute b.3. the local normal (ε_{11} and ε_{22}) and shear (ε_{12}) strains (extracted from [Benoit et al., 2016]).*

Lamellae orientation

Figure **35** presents the results on lamellae orientation during the two loading tests. Figure **35**.a shows the analysis for the tensile test and Figure **35**.b for the inflation test. WAXS analysis (Fig **35**.a) shows the polar plot of the aligned collagen lamellae. It shows a clear alignment of the lamellae along the stretching direction with increasing strain. The anisotropy value, representing the ratio of maximum parallel collagen to maximum orthogonal collagen peaks, is clearly increasing in the middle of the sample, which leads to a rearrangement of the collagen lamellae along the stretch direction. However, the pattern of the macroscopic strain at 5% is not completely recovered in these WAXS results. In particular, there is no clear difference between the center of the sample and its nearest periphery (around 6 and 10 mm). Figure **35**.b.1 presents the results of SHG image analysis determining the distribution of the orientation probability of the lamellae on the whole thickness of the cornea and on the anterior, middle and posterior stroma with increasing pressure. It shows first that the main orientation remains the same during the whole experiment and, second, that the probability distribution is changing with pressure, especially in the middle and posterior stroma. Figures **35**.b.2 and b.3 detail the percentage of lamellae oriented along the two main directions (with a margin of $\pm$ 15°) in the same zones of the cornea with increasing pressure. It is interesting to note that the proportion of lamellae oriented along the main direction φ_1 decreases with pressure, whereas the proportion of lamellae oriented along the second main direction φ_2 slightly increases, as if the lamellae reoriented themselves to be less anisotropically distributed. More particularly, this reorientation happens in the middle and posterior stroma, contrary to the collagen lamellae of the anterior stroma which tend to keep their quasi-isotropic orientation. Again, no direct link can be established between the observed macroscopic strain and the response of the collagen lamellae to increasing pressure.

Summary

These experiments have shown that collagen lamellae reorganize themselves when the cornea is submitted to mechanical load, in the stretch direction for the tensile test, and with a flip in orientation during inflation test, but in all cases, although the fraction of lamellae changes between the two main orientations, these main directions do not change. However, there is no clear and simple relationship between the reorientation of the lamellae and the macroscopic strain measured by DIC. For this reason, microscopic observations are interesting and suitable when it comes to understanding a part of the response of the cornea, but they do not fully explain the behavior of the tissue.

3.2. *In-vivo mechanical characterization of cornea*

Even though *ex-vivo* experiments can give insight into the mechanical properties, *in-vivo* properties are the one ophthalmologists look at to detect pathology in hospitals. In the past few years, two main methods have emerged to measure the response of the cornea to intraocular pressure: Brillouin optical microscopy and optical coherence elastography (OCE). Although it has been shown that these methods can be used *in-vivo*, their clinical development is not yet complete and the authors who attempted to use it so far only have results on a very limited number of patients, if any.

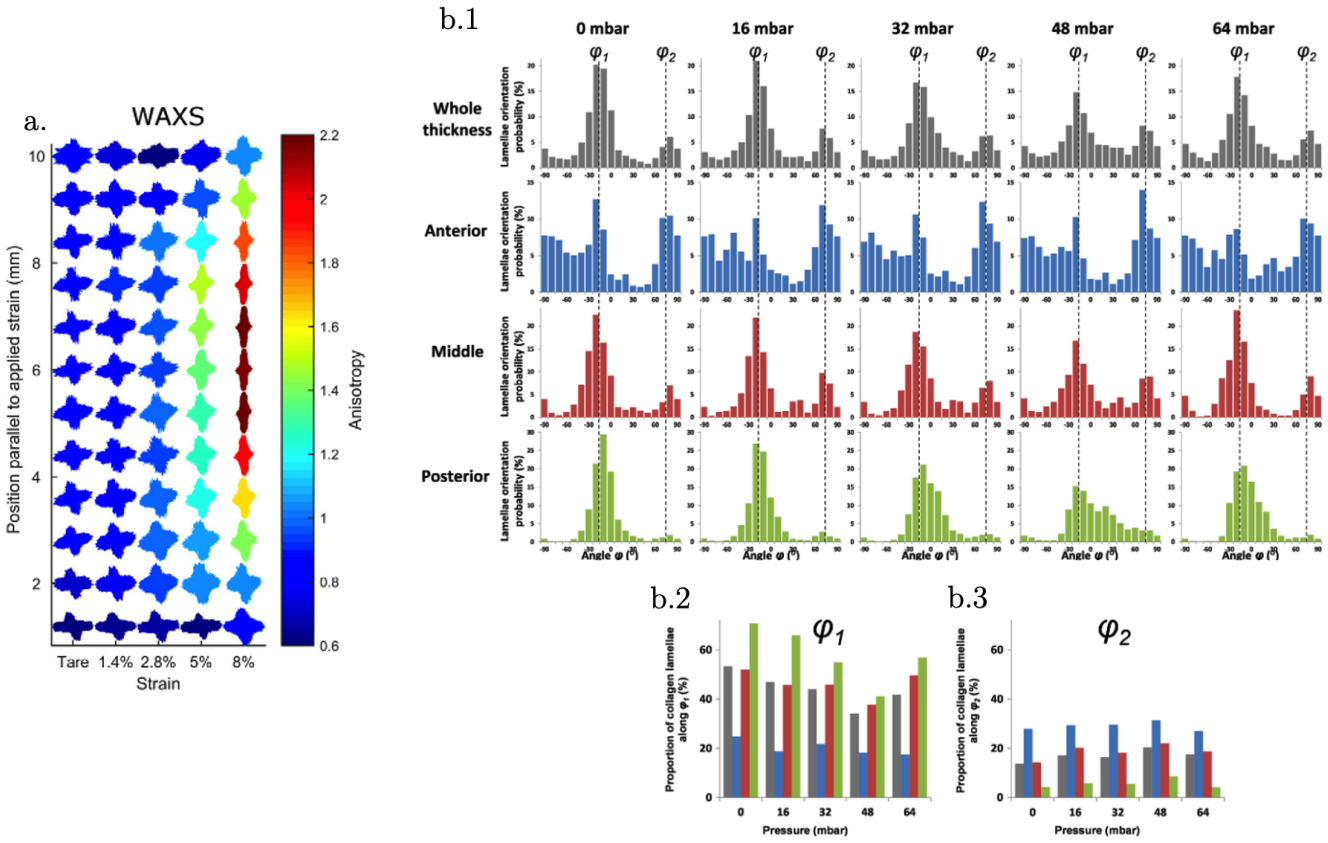

FIGURE 35. *a. Polar plot of the lamellae orientation drawn from the X-ray analysis (extracted from [Bell et al., 2018]). b.1. Distribution of the orientation probability of the collagen lamellae on the whole thickness of the cornea and on the anterior, middle and posterior stroma.* φ_1 *and* φ_2 *represent the two main orientations. b.2. and b.3. Proportions of collagen lamellae oriented along* φ_1 *and* φ_2 *(*$\pm$ *15°) (extracted from [Benoit et al., 2016]).*

3.2.1. Brillouin optical microscopy

Principle of the method

Brillouin optical microscopy is a non-invasive technique used to characterize the tissue. It has been used for the first time on human by Scarcelli *et al.* [Scarcelli et al., 2012]. The principle is presented in Figure **36** and briefly explained hereafter. A near-infrared laser light is focused on the sample and creates a local thermodynamic acoustic wave. The Doppler Brillouin frequency shift Ω is then analyzed by a confocal spectrometer and can be directly linked to the real part of longitudinal viscoelastic modulus M' [Scarcelli et al., 2014] using the relationship $M' = \rho\lambda^2\Omega^2/4n^2$ with ρ the density of the material, λ the optical wavelength and n the refractive index. At low frequencies (around 1 Hz), the variation of the longitudinal modulus M' can be easily linked to the variation of the classical Young's modulus E' using this relationship: $\delta E'/E' = (1/a)\delta M'/M'$, with $(1/a)$ a conversion factor dependent on the material.

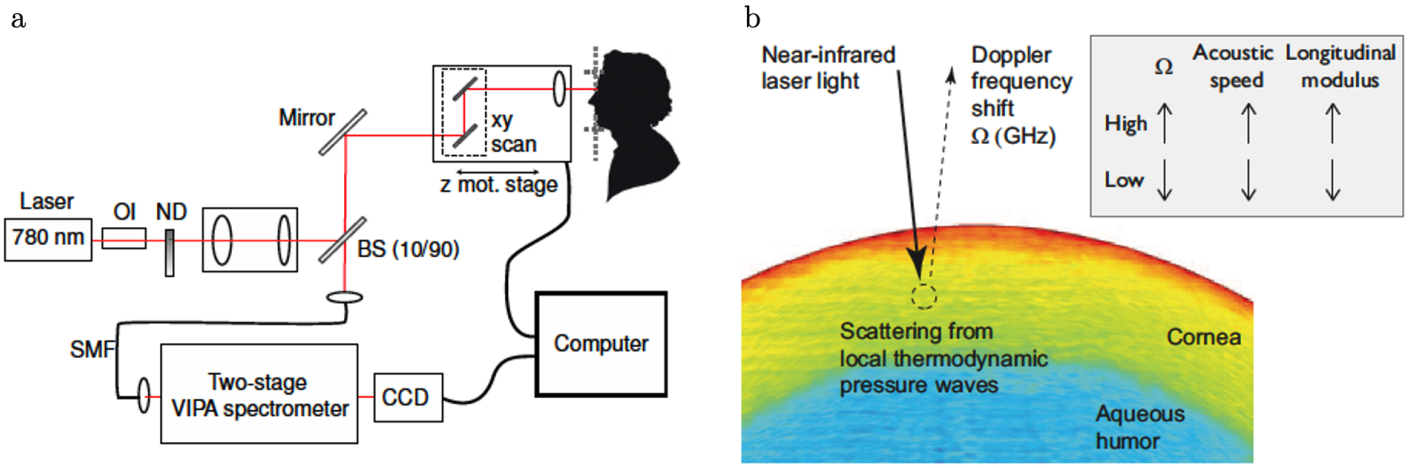

FIGURE 36. *a. Brillouin microscopy setup (extracted from [Scarcelli et al., 2012]) and b. Brillouin microscopy principle (extracted from [Yun and Chernyak, 2018]).*

Main results on healthy and pathological cases

So far, Brillouin microscopy has not been extensively used to measure the mechanical properties of corneas. A few examples exist however, first *ex-vivo* [Scarcelli et al., 2013] on healthy and keratoconic corneas and then *in-vivo* [Scarcelli et al., 2014, Shao et al., 2019, Seiler et al., 2019]. Figure **37** presents the typical sagittal curvature (in Diopter), thickness and Brillouin shift maps for a 53-year-old person with normal corneas (Fig. **37**.a) and a 40-year-old patient with advanced keratoconus (Fig. **37**.b) [Scarcelli et al., 2015]. *In-vivo* data reveal homogeneous Brillouin shift in healthy corneas while keratoconic corneas present an heterogeneous dispersion of the shift. Moreover a statistically significant decrease of Brillouin shift (and with it a decrease of stiffness) was observed in keratoconic corneas compared to healthy corneas [Scarcelli et al., 2015].

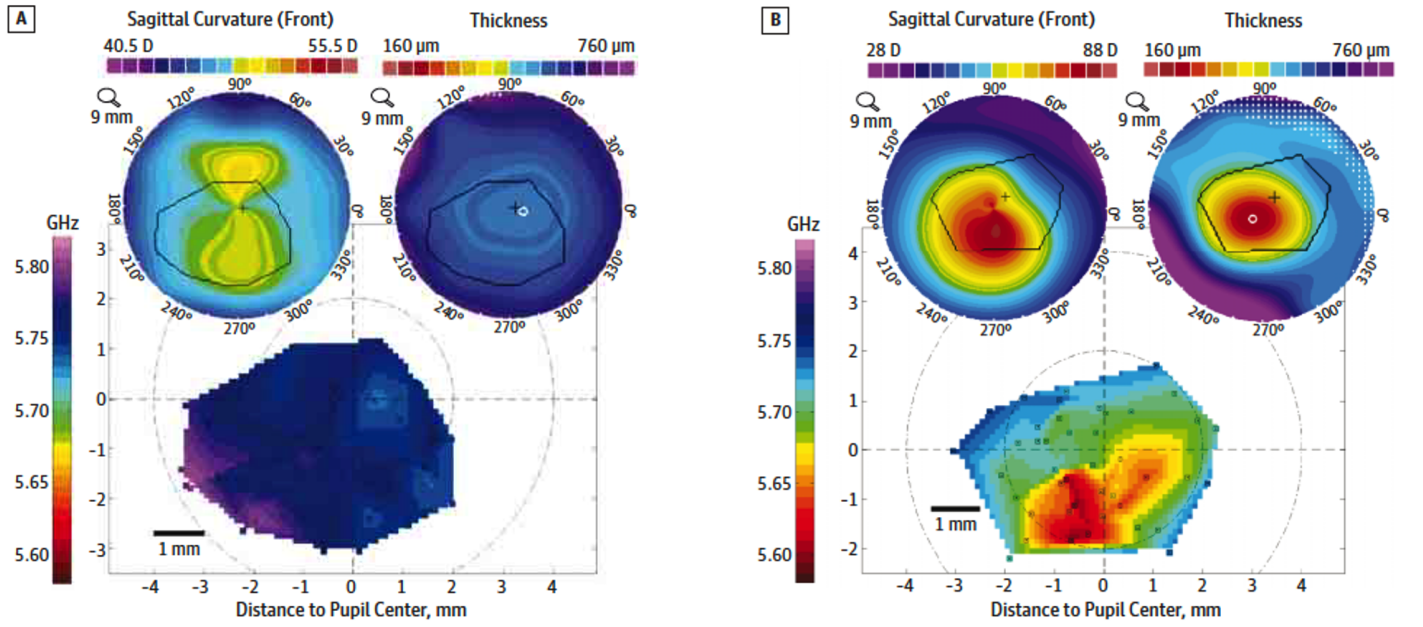

FIGURE 37. *Typical sagittal curvature (in Diopter), thickness and Brillouin shift Ω maps for a. a 53-year-old patient with normal corneas and b. a 40-year-old patient with advanced keratoconus (extracted from [Scarcelli et al., 2015]).*

Summary

Brillouin microscopy being a non-invasive method showing significant differences in mechanical elasticity of normal and pathological corneas is a promising tool to detect early stage keratoconus. However, it is a relatively new technique that only a few people have expertise on, and is therefore not used in hospitals yet. An interesting point will be to determine precisely the scale which is probed with this method, which may be very small: is the lamellae, the fibrils or even smaller structure?

3.2.2. Optical coherence elastography (OCE)

Principle of the method

Optical coherence elastography is a class of imaging techniques based on an elastography system, whose imaging device is an Optical Coherence Tomography (OCT) microscope (Sec. 2.1.). Kennedy *et al.* and Larin and Sampson reviewed the different techniques of OCE [Kennedy et al., 2014, Larin and Sampson, 2017].

Here the focus is on the methods actually applied to the cornea. The mechanical exciter can be of two main kinds: a compression load (Fig. **38**.a) or an acoustic wave perturbation (Fig. **38**.b). The two mechanical perturbations are associated with different constitutive laws, which relate the Young's modulus to a characteristics of the response to the perturbation (the observed strain ε_l – Fig. **38**.a or the phase velocity c_p – Fig. **38**.b). In the first case, tissue displacement can be obtained using one of two methods: the OCT speckle-tracking method or the phase-resolved OCT approach [Wang and Larin, 2015]. Similarly, phase velocity can be derived from the phase of the complex OCT signals in the case of acoustic wave

excitation (details on the computation can be found in [Wang and Larin, 2015]).

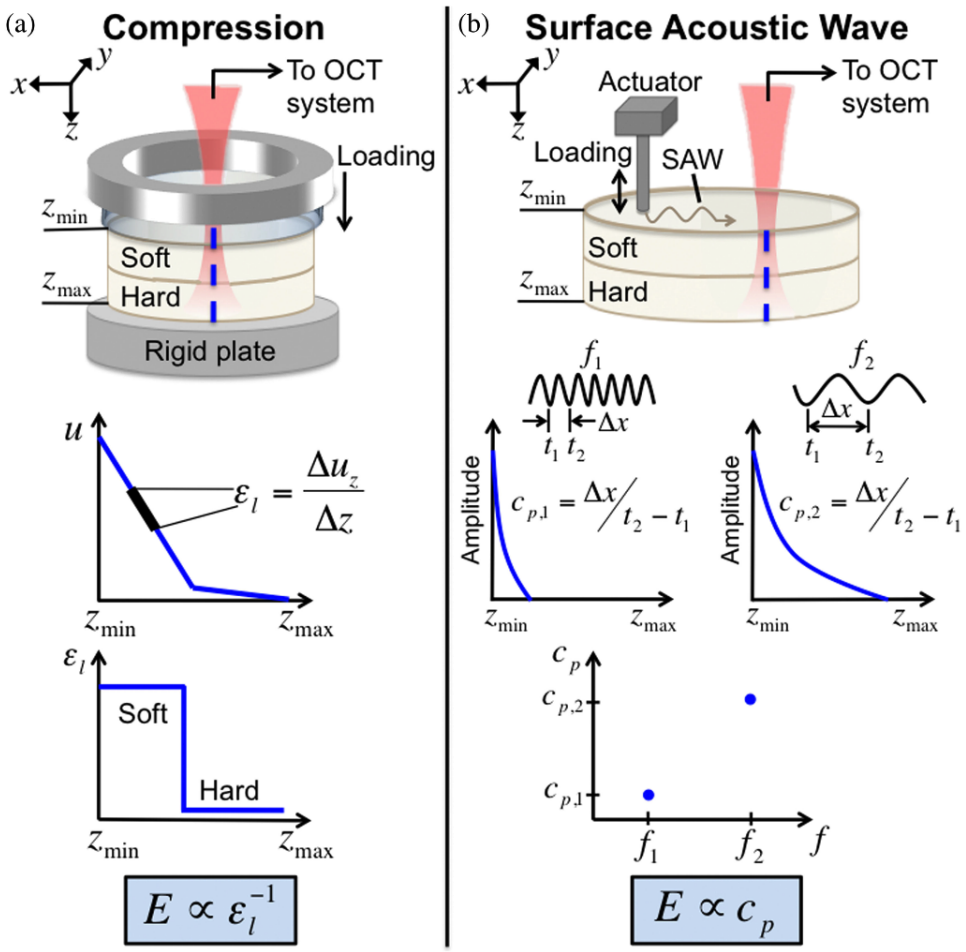

FIGURE 38. *Loading schemes and elasticity estimation for the two OCE techniques presented: (a) Compression: a mechanical load is applied and the corresponding strain is measured ε_l. (b) Surface Acoustic Wave: an acoustic wave is generated in the tissue and its phase velocity c_p is measured (extracted from [Kennedy et al., 2014]).*

Main results on healthy and pathological cases

Ford *et al.* demonstrated [Ford et al., 2011] that OCE based on speckle tracking can be used on corneas to produce 2D maps of heterogeneous displacement, using IOP as a mechanical load (Fig. **39**.a). They used a 2D cross-correlation algorithm to compute the displacement. The observed vertical displacement is consistent with the axial displacement they imposed (20 μm), and the horizontal displacement shows heterogeneity among the central region and the periphery. In a following study, they used the same speckle tracking procedure to compute the displacement resulting from the application of a flat lens on the corneas, in a clinical study with healthy (21 eyes of 12 patients) and keratoconic (15 eyes of 12 patients) corneas [De Stefano et al., 2020]. A biomechanical indicator was created to compare anterior and posterior mechanical responses. They showed that the ratio of anterior to posterior surface stiffness was smaller in keratoconic corneas, creating a novel method, clinically applicable, for the detection of the pathology.

Nahas *et al.* [Nahas et al., 2013] also used speckle-tracking to reveal the presence of two zones in the

response of porcine corneas *ex-vivo* at 1% mean strain of deformation (induced by a piston system). Figure **39**.b shows clearly a difference in the 2D vertical strain maps (computed by digital volume correlation) between the epithelium (1.6% of strain – red color) and the other regions of the cornea (less than 1% of strain). However, this technique has not yet been used *in-vivo*.

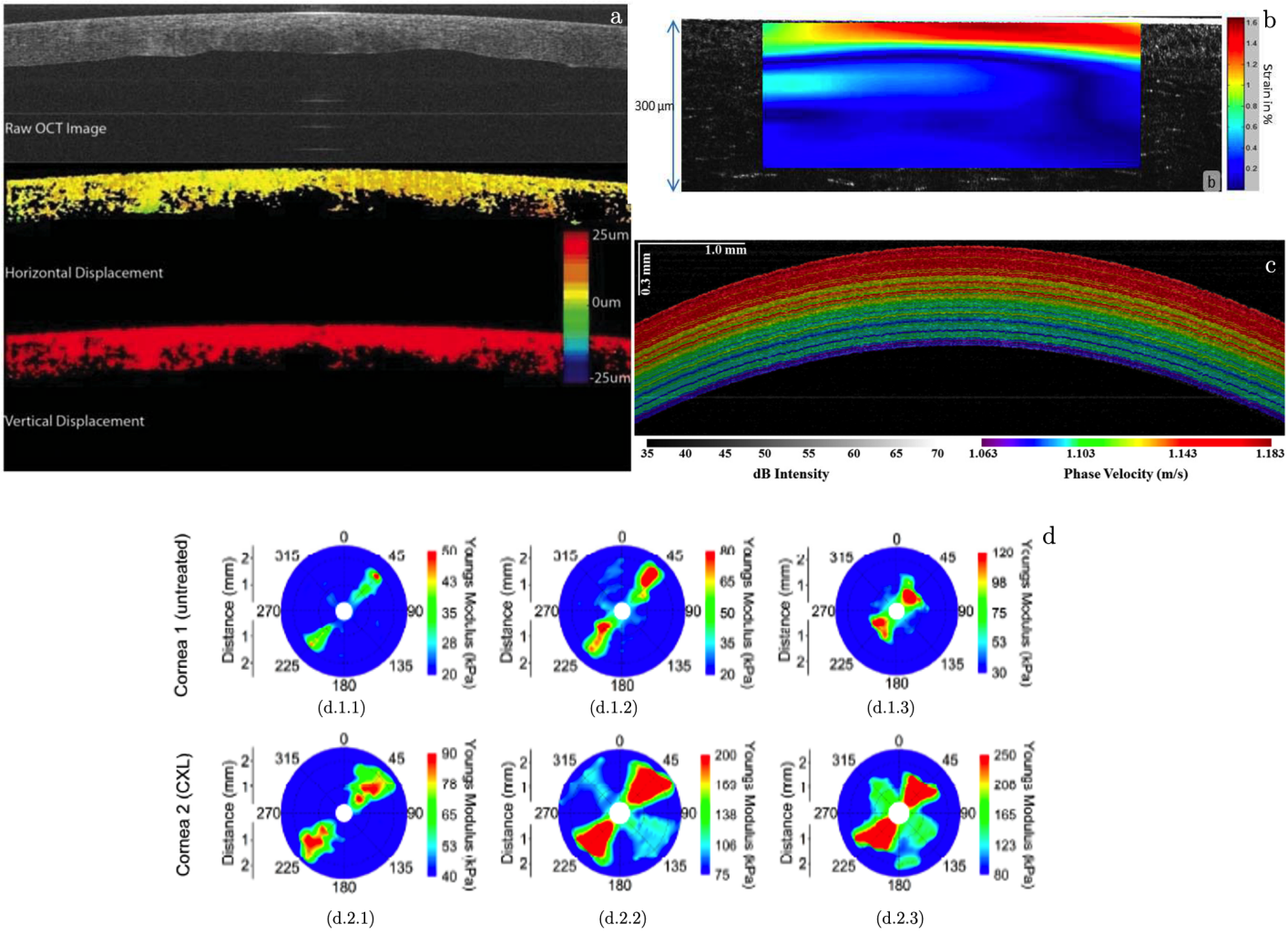

FIGURE 39. *Computation of OCE results. a. Horizontal and vertical displacement maps (middle and bottom) computed by a 2D cross-correlation algorithm corresponding to the cornea imaged by OCT (top) and submitted to axial displacement generated by IOP (extracted from [Ford et al., 2011]). b. Lamb phase velocity computed during air-puff experiment on rabbit eye (extracted from [Wang and Larin, 2014]). c. FF-OCT cross-sectional image of porcine cornea superimposed with the corresponding computing strain maps (in %) under a 1% strain application (extracted from [Nahas et al., 2013]). d. Young's modulus for untreated (d.1) and cross-linking-treated (d.2) porcine corneas at 15 (d.1.1 and d.2.1), 20 (d.1.2 and d.2.2) and 25 mmHg (d.1.3 and d.2.3) (extracted from [Singh et al., 2017]).*

Wang and Larin [Wang and Larin, 2014] used the clinical air-puff test to create dynamical loading on the cornea, and used spectral analysis of Lamb wave propagation combined with phase signal to compute the displacement of the rabbit eye, first *ex-vivo*. They have highlighted the presence of four regions of different elasticity (refining Nahas et al. study [Nahas et al., 2013]): the epithelium, the anterior stroma, the posterior stroma and the innermost region. Figure **39**.c shows the Lamb velocity computed during the experiment. The four regions appear (in accordance with the phase velocity profile

[Wang and Larin, 2014]): the epithelium corresponds to the dark red, the anterior stroma goes from red to green, the posterior stroma from green to blue, and the innermost region is in purple. Lan *et al.* [Lan et al., 2021] then conducted a clinical trial on 18 healthy eyes of 9 patients to assess the mechanical properties of human cornea *in-vivo*. A microliter air-pulse stimulator was used to generate corneal displacements, during which the wave velocity was recorded. Corneal elastic speed was found to increase with IOP and to be positively correlated with central corneal thickness. Ramier *et al.* [Ramier et al., 2020] used a similar technique to measure the shear modulus on 12 human corneas *in-vivo* using Rayleigh wave theory instead of Lamb wave theory. The shear modulus was found to be of 72 ± 14 kPa and decreasing with age.

Singh *et al.* [Singh et al., 2017] managed to obtain Young's modulus maps using an air-pulse delivery system while monitoring the intraocular pressure and imaging porcine corneas *ex-vivo* with an SS-OCT. Figure **39**.d presents Young's modulus maps at 15, 20 and 25 mmHg for healthy and CXL-treated corneas. They showed that the technique they adopted was able to quantify changes in Young's modulus between healthy and treated corneas and that cross-linked corneas were stiffer than untreated ones. This technique remains to be applied *in-vivo*.

OCE can also be coupled to acoustic/ultrasound methods to determine corneal elasticity. For example Qu *et al.* [Qu et al., 2016] have coupled Acoustic Radiation Force (ARF – see Sec. 3.1.4.) to an OCE system to compare healthy and cross-linked rabbit corneas *ex-vivo*. They showed that the elastic wave shift dropped for cross-linked corneas, corresponding to a change of stiffness in the tissue. A few years later, they used Lamb wave model to compute the wave velocity resulting from the ultrasound excitation on rabbit eyes *in-vivo* [Jin et al., 2019]. They demonstrated in those two papers the interest of the methodology to assess corneal elasticity *in-vivo*.

Summary

Similarly to Brillouin microscopy, OCE can be used to detect a pathology associated to a mechanical defect. The main limitation to determine actual values of mechanical properties in the case of cornea is that the mechanical excitation may lead to large deformations. Thus, they cannot be captured by simple linear models that are usually used in OCE. Also, most times the tissue is assumed to be homogeneous, which is not the case for cornea, especially for pathological ones. As a result, the models used to describe the mechanical response of the cornea may have to be adapted to tackle these issues.

3.2.3. Conclusion of *in-vivo* mechanical characterization of the cornea

To conclude, even if all the authors have not yet applied their methods *in-vivo* on human, it is only a question on *when* and not *how*. Brillouin microscopy and OCE are very promising techniques to determine mechanical properties of the cornea *in-vivo*, if not quantitatively, at least qualitatively. To this end, they can be used to detect pathology by comparing the measured data with healthy corneas. But as promising as they are, they cannot be used to measure the parameters that are used in mechanical modeling. The table **3.1** summarizes the measures obtained with these *in-vivo* approaches, as well as with the *ex-vivo* ones.

Scale	Imaging Technique	Data measured	Typical measure	Nature of the cornea	Local / Global measure	Stress applied	Stiffness coefficient	In-vivo / Ex-vivo
Tissue scale	Laser	Apex displacement (VS pressure)	~1/10 mm	Human	Local – on surface	Global	$\sigma = A(e^{B\varepsilon} - 1)$, $E = Cp + D$	Ex-vivo
	Stereo-correlation	Surface displacement (VS pressure)	~1/10 mm	Bovine	Local – on surface	Global	NA	Ex-vivo
	Strain / stress gauge + camera	Strip displacement / strain (VS force applied)	~1/10 mm / ~%	Porcine / bovine	Global & Local – on surface	Global	$E = {}^{\sigma}/_{\varepsilon}$	Ex-vivo
	Brillouin microscopy	Brillouin shift	~GHz	Human	Local – through thickness	Global	$M = \rho\lambda^2 \frac{\Omega^2}{4n^2}$, $\frac{\delta E}{E} = \frac{\left(\frac{1}{a}\right)\delta M}{M}$	In-vivo
Meso-scale	OCT / OCE	3D displacement / strain	~10 microns / ~%	Porcine / rabbit	Local – through thickness	Global	Based on wave theory or elasticity	Ex-vivo / In-vivo
	Scheimpflung 3D topographer	Corneal deformation -- curvature radius	~1/10 mm	Porcine	Local – on surface	Global	$\sigma = \frac{Rp}{2d}$, $\varepsilon = \Delta R/R$	Ex-vivo
	AFM as nanoindenter	Anterior / posterior elasticity	10's kPa	Human	Local – on multiple surfaces	Local	$F = \frac{4E\sqrt{R}}{3(1-\upsilon^2)} D^{3/2}$	Ex-vivo
	Bio-indenter	Young's modulus	10's kPa	Human	Local – on surface	Local	$F = \frac{4E\sqrt{R}}{3(1-\upsilon^2)} D^{3/2}$	Ex-vivo
	ARFEM	Anterior / posterior Young's modulus	~ kPa	Human	Local – on multiple location through thickness	Local	$E = \frac{Ia}{2cx_{max}}$	Ex-vivo
Micro-scale	SHG	Distribution of the lamellae orientation		Human	Local – through thickness	Global	NA	Ex-vivo
	X-rays (WAXS)	Mean orientation of the lamellae		Human	Local – averaged on thickness	Global	NA	Ex-vivo

TABLEAU 3.1. *Summary of the different techniques and data measured for the mechanical characterization of the cornea.*

4. Mechanical modeling of the human cornea

We have shown in the previous sections that we have access to the geometry and/or to the microstructure of the cornea. Similarly, it is possible to determine, at least to some extend, the strain in the cornea. However, data are sparse due to limited numbers of cornea tested. This is particularly true for the keratoconic corneas. As it is interesting to be able to predict the consequences of a change in the microstructure, in the geometry or in the mechanical properties (either pathological or due a treatment), models of cornea have been developped in the past decades.

4.1. *Mechanical response of cornea*

The stroma is considered to be the main contributor to the mechanical response of cornea. In parallel, there is also a lack of data on the other layers of cornea. As a result, "stroma" and "cornea" will be used indifferently in the framework of mechanical modeling. Similarly, fibrils or fibers are sometime used instead of lamellae, as the models are inspired from ones for fiber-enrich composites.

4.1.1. Constitutive behavior of cornea

Cornea is usually considered as a quasi-incompressible material reinforced by fibers – the two families of lamellae can be considered each as a family of fibers – which may sustain very large deformations. As such, it is generally modeled as a hyperelastic material [Alastrué et al., 2006, Pandolfi and Holzapfel, 2008, Gefen et al., 2009, Studer et al., 2010, Simonini and Pandolfi, 2015, Giraudet et al., 2022] – with the possible addition of viscous terms to introduce history dependence and dissipation [Nguyen et al., 2008, Kling et al., 2014, Whitford et al., 2018] when considering the static or dynamic cases, respectively. Dynamic cases are usually used to model air-puff clinical tests. Here the emphasis will be placed on the static response as it is simpler but alreay quite complex. In this case, the associated strain energy density ψ is then splitted into three contributions:

$$\psi = \psi^{iso} + \psi^{vol} + \psi^{lam}, \tag{1}$$

with an isotropic part ψ^{iso} corresponding to the matrix, the keratocytes and the randomly distributed lamellae, a volumetric part ψ^{vol} penalizing any change of volume and an anisotropic part ψ^{lam}, taking into account the mechanical role of oriented lamellae.

The isotropic part depends generally on the first three invariants I_1, I_2 and I_3 or reduced invariants ($\bar{I}_1 = I_1 I_3^{-1/3}$, $\bar{I}_2 = I_2 I_3^{-2/3}$) and is usually chosen as a Mooney-Rivlin or neo-Hookean like energy density [Alastrué et al., 2006, Pandolfi and Holzapfel, 2008, Studer et al., 2010, Simonini and Pandolfi, 2015, Giraudet et al., 2022]:

$$\psi^{iso}(\boldsymbol{\xi}, \mathbf{C}) = \frac{1}{2} C_1 (\bar{I}_1 - 3) + \frac{1}{2} C_2 (\bar{I}_2 - 3) \tag{2}$$

with C_1 and C_2 two parameters of the model characterizing the isotropic part of the tissue.

The volumic part penalizes any change of volume and can have several expression, function only of J:

typically, it can be based on the work of P. Ciarlet and G. Geymonat [Ciarlet and Geymonat, 1982].

$$\psi^{vol}(\boldsymbol{\xi}, \mathbf{C}) = \begin{cases} K \log^2(J) \text{ [Alastrué et al., 2006, Pandolfi and Holzapfel, 2008]} \\ \frac{1}{D}(J-1)^2 \text{ [Studer et al., 2010]} \\ \frac{1}{4}K(J^2 - 1 - 2\log(J)) \text{ [Simonini and Pandolfi, 2015]} \end{cases} \tag{3}$$

with K the bulk modulus (or the corresponding $1/D$). Minimizing the energy ψ^{vol} leads to $J = 1$, so that the volume of the material does not change. So, to obtain a quasi-incompressible material, most of the models consider a high bulk modulus compared to the other moduli of the energy density. A notable exception is the model of Studer *et al.* [Studer et al., 2010], which has a bulk modulus of the same order of magnitude as the isotropic material constant.

For the anisotropic part, there are two classical ways of taking into account the contribution of fibers in biological tissues [Holzapfel et al., 2019]:

— the 'generalized structure tensor' (GST) approach, which is widely used in Holzapfel-like models for many different tissues reinforced by fibers such as arteries or other blood vessels [Gasser et al., 2006, Alastrué et al., 2008, Bols et al., 2013, Holzapfel et al., 2015], myocardium [Holzapfel and Ogden, 2009] or skin [Jor et al., 2011] and cornea [Pandolfi and Holzapfel, 2008, Montanino et al., 2018, Whitford et al., 2015];

— the 'angular integration' (AI) approach, used for arteries [Sacks, 2003, Billiar and Sacks, 2000], cartilage [Ateshian et al., 2009, Pierce et al., 2016] or cornea [Studer et al., 2010, Nguyen and Boyce, 2011], with 2D data and with 3D data [Petsche and Pinsky, 2013, Giraudet et al., 2022].

The anisotropic energy density used in GST models is usually based on the fourth and sixth invariants (I_4 and I_6 respectively, considering each family of fiber). Calling $\boldsymbol{M}_{01}$ and $\boldsymbol{M}_{02}$ the mean fiber directions on the reference configuration, the reduced invariants are defined as follow: $\bar{I}_4 = \boldsymbol{M}_{01}.\bar{\mathbf{C}}.\boldsymbol{M}_{01}$ and $\bar{I}_6 = \boldsymbol{M}_{02}.\bar{\mathbf{C}}.\boldsymbol{M}_{02}$, with $\mathbf{C} = J^{2/3}\bar{\mathbf{C}}$. The associated energy density takes the following form (or a variation there of) [Alastrué et al., 2006, Pandolfi and Holzapfel, 2008]:

$$\psi^{lam}(\boldsymbol{\xi}, \mathbf{C}) = \frac{k_{11}}{2k_{21}}\{\exp[k_{21}(\bar{I}_4 - 1)^2] - 1\} + \frac{k_{12}}{2k_{22}}\{\exp[k_{22}(\bar{I}_6 - 1)^2] - 1\}. \tag{4}$$

An exponential function is generally used to mimic the mean response of the collagen lamellae, as they are considered to behave like collagen fibrils, with a low stiffness response at low strain and a rapid change of response leading to a high stiffness at high strain (Fig. **40**).

In particular, it allows to have a quasi null response of the collagen lamellae when they are crimped (toe region in Fig. **40**). It is also consistent with the pressure with apex displacement results from inflation tests [Elsheikh et al., 2008]. Considering the whole cornea, a parameter (κ in [Pandolfi and Holzapfel, 2008]) can be added to take into account the variation of the scatter of the fibers in the tissue. In this approach, at each point of computation, the mean and the scatter of the fiber direction are assessed, and a global mechanical contribution is computed based on these two parameters, for each family of fibers.

In the AI case, the approach is reversed. An elementary response for collagen lamellae $\delta\psi^{lam}$ is consi-

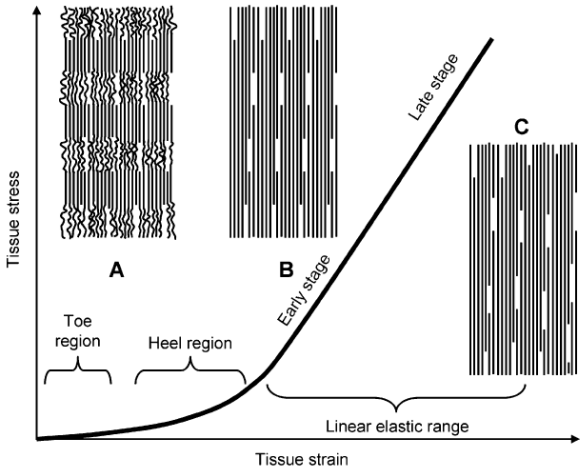

FIGURE 40. *Collagen fibril response to tension (from [Fratzl et al., 2008]). At low strain, the fibrils are crimped and thus oppose practically no resistance to tension (toe region). In the transitional regime (heel region), fibrils tend to align one next to the other and to straighten. They begin to oppose resistance to tension. In the linear elastic range region, fibrils are not crimped anymore – their stiffness can be measured using a tension test along the direction of the fibrils.*

dered, and the total mechanical response on a particular location $\psi^{lam}(\boldsymbol{\xi}, \mathbf{C})$ is the integral over the unit sphere ω (for the most complete 3D model [Petsche and Pinsky, 2013]) of the elementary contribution weighted by the density distribution $\rho(\boldsymbol{\xi}, \theta, \phi)$ of the fiber at this location,

$$\psi^{lam}(\boldsymbol{\xi}, \mathbf{C}) = \int_{\omega} \rho(\boldsymbol{\xi}, \theta, \phi) \delta\psi^{lam}(\boldsymbol{\xi}, \theta, \phi) \mathrm{d}\omega. \tag{5}$$

In that case also, all the models found in the literature on cornea for the elementary mechanical response of lamellae $\delta\psi^{lam}$ are based on exponential (or logarithmic) or bi-slope functions:

$$\delta\psi^{lam}(\boldsymbol{\xi}, \theta, \phi) = \begin{cases} \dfrac{\alpha}{\beta}[\exp(\beta\{\lambda_f^2 - 1\}) - \beta\lambda_f^2] \text{ [Nguyen and Boyce, 2011]} \\ \dfrac{\alpha_1}{2\alpha_2}[\exp(\alpha_2\{I_4 - 1\}^2) - 1] \text{ [Petsche and Pinsky, 2013]} \\ \dfrac{\mu}{\gamma}(\bar{I}_4^{\gamma/2} - 1) - \mu \ln(\bar{I}_4^{1/2}) \text{ [Studer et al., 2010]} \\ \dfrac{1}{2} k l_u (\dfrac{\lambda}{\lambda_u} - 1)_+^2 \text{ [Giraudet et al., 2022]} \end{cases} \tag{6}$$

with

$$\begin{cases} \lambda_f^2 = I_4 = \lambda^2 = \boldsymbol{a}.\mathbf{C}.\boldsymbol{a} \\ \bar{I}_4 = \boldsymbol{a}.\bar{\mathbf{C}}.\boldsymbol{a} \\ \boldsymbol{a}(\theta, \phi) \quad \text{the local integrating direction} \end{cases} \tag{7}$$

In the case of Studer *et al.* [Studer et al., 2010], they use a modified version of the polynomial Odgen law [Markert et al., 2005] to include one direction of anisotropy, giving a logarithmic formula which cannot be linked directly to the collagen fibril response of Figure **40**.

Whether using GST or AI approaches, these models do not take into account the energy due to water exchange, except for [Cheng et al., 2015], so that the action of the endothelium is not considered. Also, validations of these models are based on very few experiments – as the quantity of data on cornea is limited – measuring apex displacement ([Elsheikh et al., 2008, Lombardo et al., 2014] for the human cornea) or 3D displacement of the anterior surface ([Boyce et al., 2008] for bovine cornea), and performed exclusively on healthy subjects.

4.1.2. Density distribution of fibers

The 3D density distribution of fibers is not available for the whole cornea. However, X-ray scattering (Fig. **7** – [Aghamohammadzadeh et al., 2004, Boote et al., 2006]) allows a 2D mean representation of the oriented lamellae to be obtained. Two ways of incorporating these data are found in the literature. The first option is to look at the data at each measurement point – an example is given Figure **41**. It is well known that the intensity at each point of measurement I_{exp} of X-ray scattering can be represented by a function I_m,

$$I_m(\phi|\kappa_{ip,1},\kappa_{ip,2},\mu_1,\mu_2) = I_{iso} + C_1\mathrm{VM}_{ip}(\phi|\kappa_{ip,1},\mu_1) + C_2\mathrm{VM}_{ip}(\phi|\kappa_{ip,2},\mu_2), \tag{8}$$

depending on I_{iso}, a constant component representing the isotropic part of the measure and C_1 and C_2, the measures of the number of oriented lamellae in each direction at the point of measure. The distributions of lamellae is described by Von Mises distributions:

$$\mathrm{VM}_{ip}(\phi|\kappa_{ip},\mu) = \frac{e^{\kappa_{ip}\cos(2(\phi-\mu))}}{C(\kappa_{ip})}, \tag{9}$$

where μ is the main direction of the fiber family, κ_{ip} represents a measure of the scatter of the lamellae, and $C(\kappa_{ip})$ is a normalization factor.

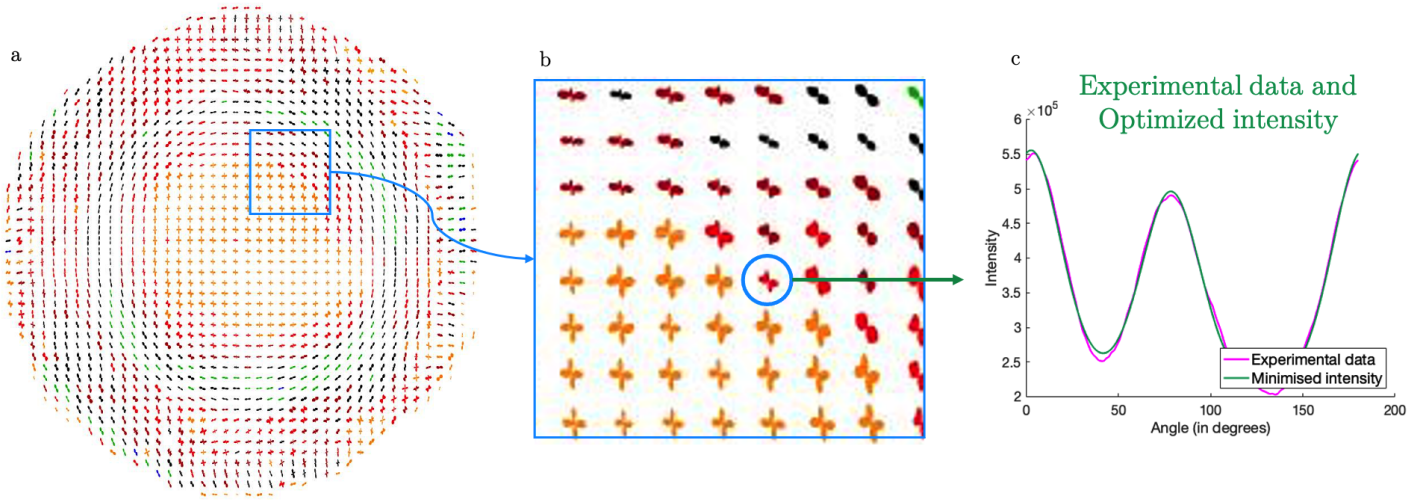

FIGURE 41. *Determination of the 2D density distribution. a. Polar plot of the direction of the lamella [Aghamohammadzadeh et al., 2004], b. zoom on a particular measurement point, and c. experimental and corresponding optimized intensity (extracted from [Giraudet et al., 2022]).*

Minimizing the error $|I_m - I_{exp}|$ at each point of measurement allows the parameters linked to the lamellae to be found: C_i the relative number of oriented lamellae, μ_i their main direction and $\sigma_{ip,i}$ their

scatter. Afterwards, the data are interpolated on the whole cornea (*i.e.* at the nodes, for finite element modeling).

The second technique is based on a model by Pinsky *et al.* [Pinsky et al., 2005] (inspired by X-ray images), which gives the probability density function $\Phi(R, \phi|\theta)$, with (R, ϕ) being the polar coordinate of the location (the center of the cornea being the center of the coordinate system and the N-T and S-I directions being the x- and y-axes):

$$\Phi(R, \phi|\theta) = \begin{cases} \Phi_1(R, \phi|\theta) = \cos^{2n}(\theta) + \sin^{2n}(\theta) + c_1 & \text{for} \quad R \in [0, 4] \\ \Phi_2(R, \phi|\theta) = \sin^{2n}(\theta - \phi) + c_2 & \text{for} \quad R \in [5.5, 6.5] \end{cases} \tag{10}$$

with a linear combination of the 2 functions for $R \in [4, 5.5]$ to smoothly transition from one to the other. Figure **42** presents the results for the case used by Studer *et al.* [Studer et al., 2010] with $c_1 = 0.45$, $c_2 = 0.72$ and $n = 4$ and the linear combination $\Phi(R, \phi|\theta) = w_1(R)\Phi_1(R, \phi|\theta) + (1 - w_1(R))\Phi_2(R, \phi|\theta)$ in between with $w_1 = \frac{1}{2}\{\cos(\frac{\pi}{1.5}[5.5 - R]) + 1\}$.

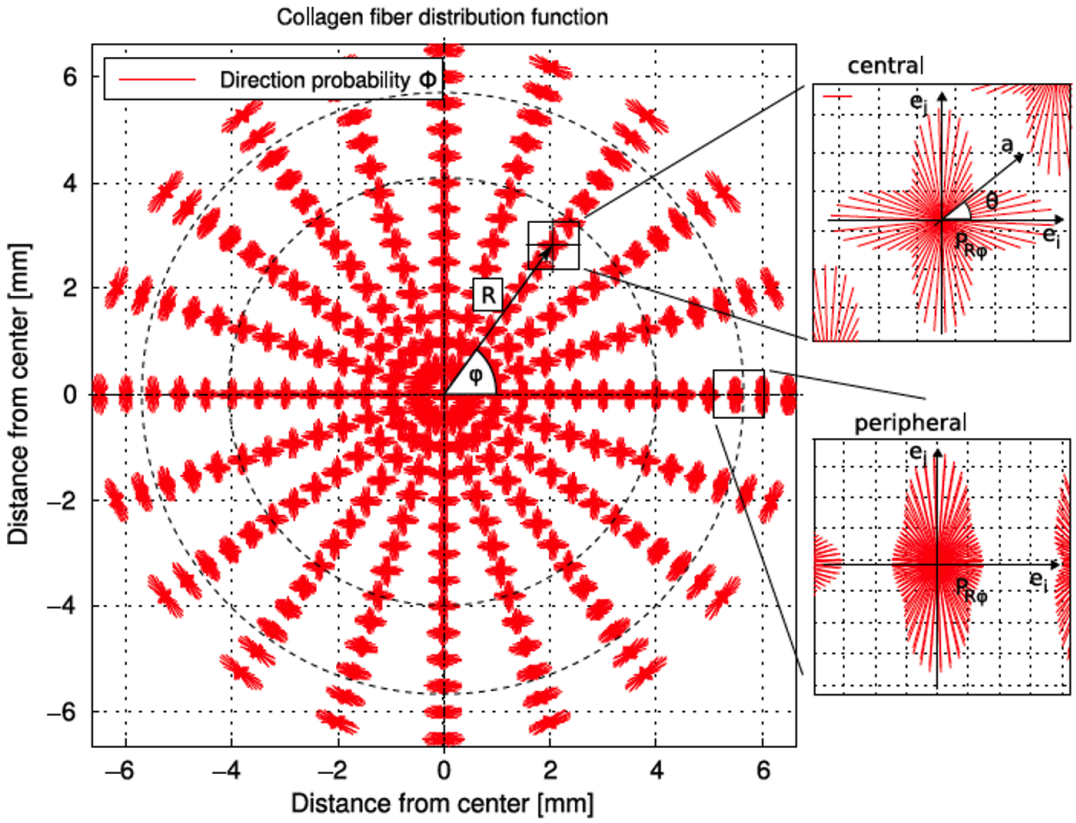

FIGURE 42. *Probability distribution map, computed using Eq.* (10)*, with* c_1 *= 0.45 and* c_2 *= 0.72. Transitional zone corresponds to radius between 4 and 5.5mm (dashed circles) [Studer et al., 2010].*

Both approaches give information on the so called in-plane orientation of the lamellae, but it gives no information on the out-of-plane distribution. The development of SHG microscopy imaging of cornea made it possible to have a model for the third dimension. Winkler *et al.* [Winkler et al., 2013] imaged the cornea and Petsche and Pinsky [Petsche and Pinsky, 2013] built a model of the distribution on the third dimension. SHG images (Fig. **43** – middle) are studied to model the out-of-plane scatter of the lamellae.

The authors show that there is an exponential dependency of the cut-off-angle ψ_{coa} with normalized depth s:

$$\psi_{coa}(s) = 28.6^{\circ}\frac{e^{3.19(1-s)}-1}{e^{3.19}-1}, \tag{11}$$

with a maximum cut-off-angle of 28.6°. No lateral heterogeneity has been measured. Then the out-of-plane distribution of the fibers can be modeled either as a Von Mises distribution

$$\mathrm{VM}_t(\theta|\kappa_t,\nu) = \frac{e^{\kappa_t\cos(2\theta)}}{C(\kappa_t)}\ (C(\kappa_t)\text{ being a normalization factor}),$$

taking into account the depth variation of the maximum out-of-plane angle $\psi(s)$ to characterize the change of the out-of-plane scatter κ_t in thickness, or as a coupled Heaviside function (as in [Petsche and Pinsky, 2013])

$$\rho^{SHG}(s,\phi) = \mathrm{H}[\phi - \{\frac{\pi}{2} - \psi_{coa}(s)\}] - \mathrm{H}[\phi - \{\frac{\pi}{2} + \psi_{coa}(s)\}],$$

with ϕ the local inclination angle.

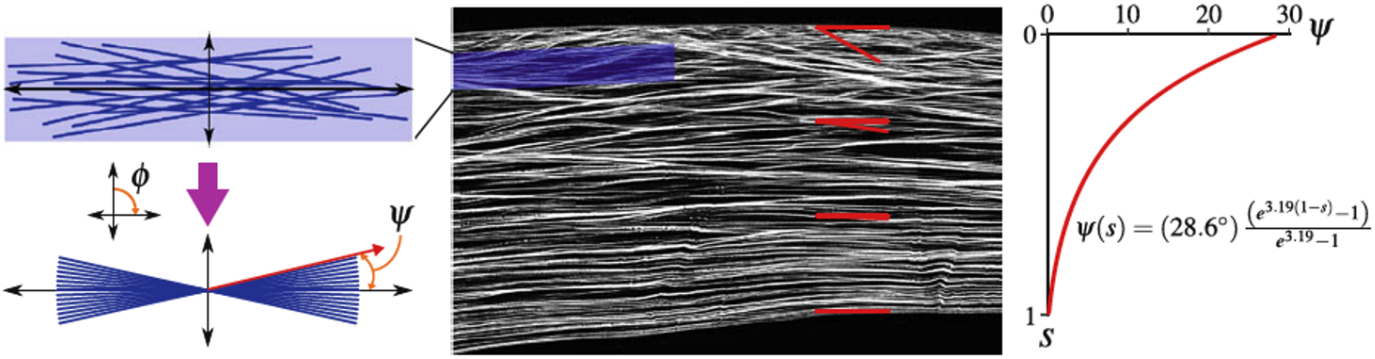

FIGURE 43. *Extraction of the 3D density distribution (from [Petsche and Pinsky, 2013]). The SHG images allow a model to be built for the out-of-plane angle ψ of the lamellae with depth.*

The table **4.2** gives a summary of the different models in the litterature cited here.

	Notation	Reference	Expression	Value of the coefficients	Comments
Isotropic matrix	ψ^{iso}	[Alastrué et al., 2006]	$\frac{C_1}{2}(\bar{I}_1-3)+\frac{C_2}{2}(\bar{I}_2-3)$	$C_1 = 5\ kPa$ $C_2 = 0\ kPa$	The neo-Hookean is mostly used to represent the isotropic matrix, but the Mooney-Rivlin energy allows to take into account second order response, that may exists in the cornea (no experimental data available0
		[Pandolfi et al., 2008]	$\frac{c}{2}(\bar{I}_1-3)$	$c = 60\ kPa$	
		[Simonini et al., 2008]	$\frac{\mu_1}{2}(\bar{I}_1-3)+\frac{\mu_2}{2}(\bar{I}_2-3)$	$\mu_1 = 60\ kPa$ $\mu_2 = -10\ kPa$	
		[Studer et al., 2010]	$\frac{C_{10}}{2}(\bar{I}_1-3)$	$C_{10} = 60\ kPa$	
		[Nguyen et al., 2011]	$\frac{\mu}{2}(\bar{I}_1-3)$	μ~26.5 kPa	
		[Petsche et al., 2013]	$\frac{\mu}{2}(I_1-3)$	$\mu = 5.59\ kPa$	
		[Giraudet et al., 2022]	$\kappa_1(\bar{I}_1-3)+\kappa_2(\bar{I}_2-3)$	κ_1 and κ_2 distributed over the cornea ~MPa	
Quasi-incompressibility	ψ^{vol}	[Alastrué et al., 2006]	$\frac{1}{D}(\ln(J))^2$	$D = 13.33\ MPa^{-1}$	As cornea is considered as a quasi-incompressible tissue, the volumetric part of the energy function is here to ensure that the volume is preserved (J~1), by penalizing using a relatively huge bulk modulus (at least one order of magnitude higher than the coefficient of the isotropic part)
		[Pandolfi et al., 2008]	$K(log(J))^2$	$K = 5.5\ MPa$	
		[Simonini et al., 2008]	$\frac{1}{4}K(J^2-1-2\,log(J))$	$K = 5.5\ MPa$	
		[Studer et al., 2010]	$\frac{1}{D}(J-1)^2$	NK	
		[Nguyen et al., 2011]	$\frac{1}{4}K(I_3-\ln(I_3)-1)$	NK	
		[Petsche et al., 2013]	$\frac{\lambda}{4}(J^2-1)-\left(\frac{\lambda}{2}+\mu\right)\ln(J)$	$\lambda = 500\ kPa$	
		[Giraudet et al., 2022]	$K(J^2-1-2\,log(J))$	$K = 80\ kPa$	
Anisotropic lamellae	ψ^{lam} (GST) or $\delta\psi^{lam}$(AI)	[Alastrué et al., 2006]	$\frac{k_1}{2k_2}\{\exp[k_2(\bar{I}_4-1)^2]-1\}+\frac{k_3}{2k_4}\{\exp[k_4(\bar{I}_6-1)^2]-1\}$ GST approach	$k_1 = 102.643\ MPa$ $k_2 = 102.643$ $k_3 = 0.004852\ MPa$ $k_4 = 102.643$	Two ways of integrating the anisotropic contribution are considered for the lamellar energy: the generalized structure tensor (GST) and the angular integration approach (IA). While the GST approach has a great advantage in term of computational cost, the AI approach allows to take into account the inhomogeneous contribution of the fibers in all the directions of integration at each point of the cornea considered. In the case of the cornea, 2D distribution of lamellae are obtained using X-rays data, while out-of-plane dispersion comes from SHG images. In all cases, exponential functions are often used to mimic the response of a collagen fibril, while considering that the collagen lamellae have the same behavior.
		[Pandolfi et al., 2008]	$\frac{k_{11}}{2k_{21}}\{\exp[k_{21}(\bar{I^*}_4-1)^2]-1\}+\frac{k_{12}}{2k_{22}}\{\exp[k_{22}(\bar{I^*}_6-1)^2]-1\}$, $\bar{I^*}_i = \kappa_i\bar{I}_i+(1-3\kappa_i)\bar{I}_i$ GST approach	$k_{11} = 20\ kPa$ $k_{21} = 400$ $k_{12} = 20\ kPa$ $k_{22} = 400$	
		[Simonini et al., 2008]	$\frac{k_{11}}{2k_{21}}\left\{\exp\left[k_{21}\left(\bar{I^*}_{4,1}-1\right)^2\right]\right\}\{1+K_1^*\sigma^2_{\bar{I^*}_{4,1}}\}+\frac{k_{12}}{2k_{22}}\{\exp\left[k_{22}\left(\bar{I^*}_{4,2}-1\right)^2\right]\}\{1+K_2^*\sigma^2_{\bar{I^*}_{4,2}}\}$ GST approach	$k_{11} = 40\ kPa$ $k_{21} = 200$ $k_{12} = 40\ kPa$ $k_{22} = 200$	
		[Studer et al., 2010]	$\frac{\mu_m}{\gamma_m}\left\{\bar{I}_4^{\frac{\gamma_m}{2}}-1\right\}-\mu_m\ln\left(\bar{I}_4\right)^{\frac{1}{2}}+\frac{\mu_k}{\gamma_k}\left\{\bar{I}_6^{\frac{\gamma_k}{2}}-1\right\}-\mu_k\ln\left(\bar{I}_6\right)^{\frac{1}{2}}$ 2D AI approach	$\mu_m = 24\ MPa$ $\gamma_m = 0.13$ $\mu_k = 95\ MPa$ $\gamma_k = 0.08$	
		[Nguyen et al., 2011]	$\frac{\alpha}{\beta}\{\exp[\beta(\lambda_f^2-1)]-\beta\lambda^2\}$ $\lambda_f^2 = \underline{a}.\underline{\underline{C}}.\underline{a}, \underline{a} = (\cos(\theta),\sin(\theta),0)$ 2D AI approach	α~0.12 kPa β~91	
		[Petsche et al., 2013]	$\frac{\alpha_1}{2\alpha_2}\{\exp[\alpha_2(I_4-1)^2]-1\}$ 3D AI approach	$\alpha_1 = 638\ kPa$ $\alpha_2 = 312$	
		[Giraudet et al., 2022]	$\frac{1}{2}k\lambda_u l_0\left(\frac{\lambda}{\lambda_u}-1\right)_+^2+t_u l_0\lambda$ $\lambda^2 = \underline{r_0}.\underline{\underline{C}}.\underline{r_0}$ 3D AI approach	$k\lambda_u l_0$ ~100-1000kPa $t_u = 0$	

TABLEAU 4.2. *Summary of the energy functions and parameters values used in the last paper on modeling of the cornea as an hyperelastic material only.*

4.1.3. Validation of models on inflation test

Most models are validated on inflation tests, against the data of Elsheikh *et al.* [Elsheikh et al., 2008] (see Sec. 3.1.1.), since they are the only available data on human corneas. Finite element (FE) methods are used to compute the mechanical response of cornea to intraocular pressure. Even though the mechanical behavior of cornea and the boundary conditions can change from one author to another, the principle remains the same. The tissue is fixed to the sclera and the intraocular pressure is applied to the posterior surface of the cornea. No other forces are applied. A constistutive model has to be provided. The geometry of cornea is described by the biconic function and usually adapted to real patient ones. A spatial discretization is performed to create the mesh used in the FE code. Figure **44** presents a typical scheme (Fig. **44**.a) and mesh (Fig. **44**.b) used to implement the corneal model in a FE code [Gefen et al., 2009].

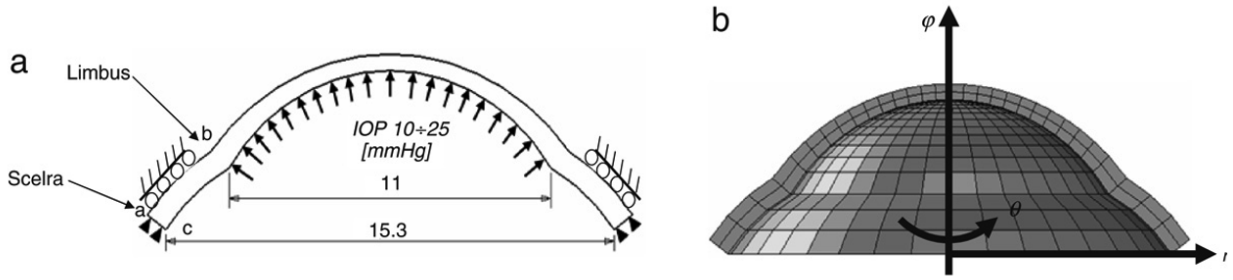

FIGURE 44. *FE modeling of an inflation test. a. Model description of the forces applied to the cornea (IOP) and of the boundary conditions. b. Typical mesh used to describe the geometry of the tissue (extracted from [Gefen et al., 2009]).*

Figure **45** presents the results for four different cases of modeling: one model with AI approach and only in-plane distribution of the lamellae (a.1 and a.2 – [Studer et al., 2010]), one model with GST approach and only in-plane distribution of the lamellae (b – [Pandolfi and Holzapfel, 2008]) and two models with AI approach and 3D distribution of the lamellae (c – [Petsche and Pinsky, 2013] and d – [Giraudet et al., 2022]). Figures **45**.a.1, a.2, c and d are comparing simultations to data from Elsheik *et al.* study [Elsheikh et al., 2008] on human cornea. Fig.**45**.b is comparing simulation to data from [Elsheikh and Anderson, 2005] on porcine corneas. It shows that all the models can be calibrated to fit the data of pressure with apex displacement and for both age groups in the first case. The parameters found in the validation process provide insight into the mechanical behavior of healthy cornea *ex-vivo* but they may not be unique and should be adapted for pathological cases.

4.2. *The case of the keratoconus*

The case of keratoconus has been studied numerically through inflation tests by several authors [Gefen et al., 2009, Carvalho et al., 2009, Norouzpour and Mehdizadeh, 2012, Pandolfi et al., 2019, Giraudet et al., 2022] considering different hypotheses based on the same assumptions: in keratoconic corneas a change of geometry is observed and the stiffness is decreased in the cone region with respect to the rest of the cornea (Sec. 3.2.). Gefen *et al.* [Gefen et al., 2009], Carvalho *et al.* [Carvalho et al., 2009] and Giraudet *et al.* [Giraudet et al., 2022] studied both the thinning of the region of the cone and the reduction of some mechanical properties of cornea (meridian elastic modulus and shear modulus perpendicular to corneal surface). While Gefen *et al.* [Gefen et al., 2009] shows that the main ingredient to

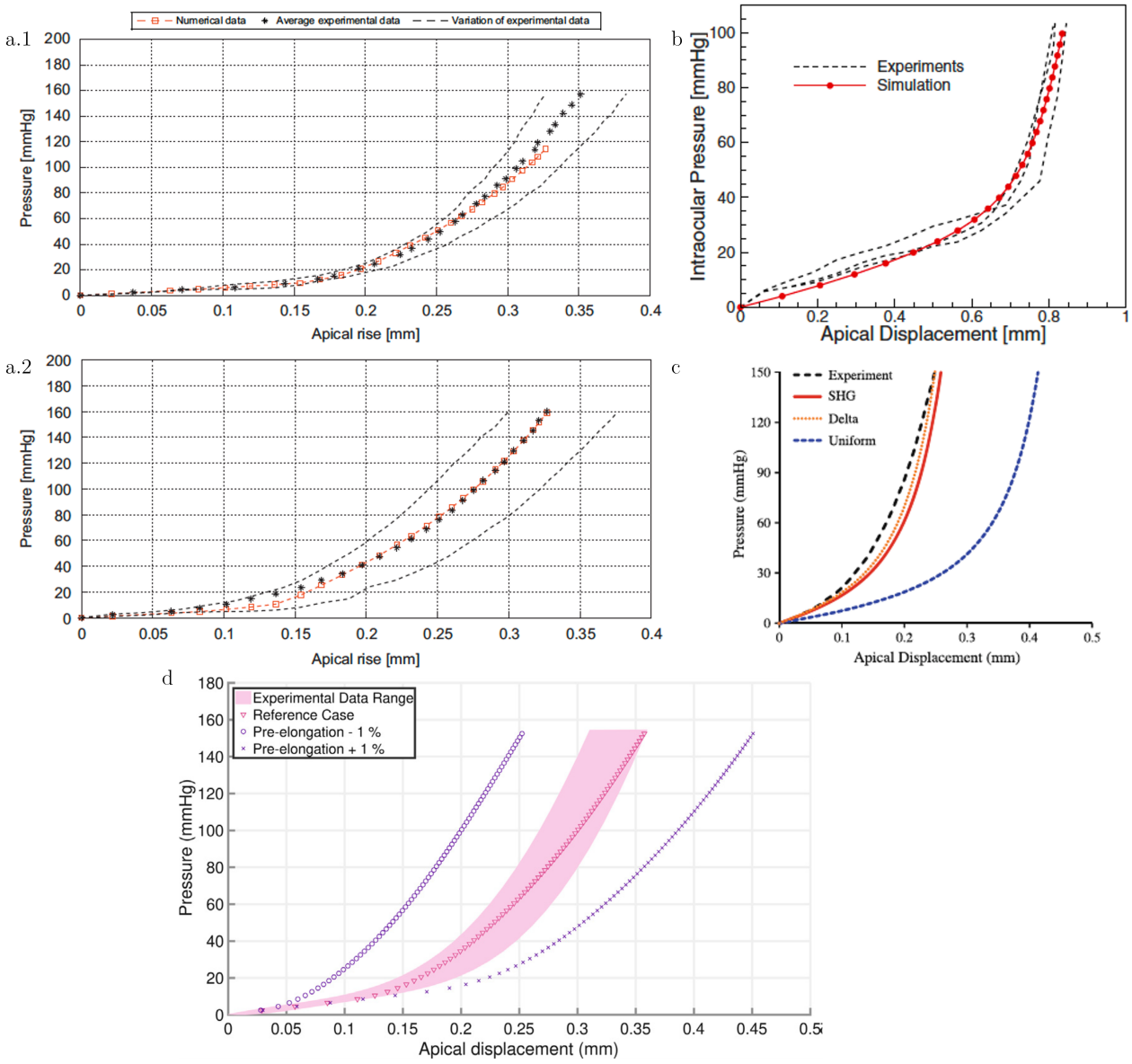

FIGURE 45. *Results of inflation test simulations compared with Elsheikh et al. [Elsheikh et al., 2008, Elsheikh and Anderson, 2005] data. a.1 and a.2. Results extracted from [Studer et al., 2010] for two age groups (a.1. 65–79 years old corneas and a.2. 80–95 years old corneas) – model with AI approach and only in-plane distribution of the lamellae compared to [Elsheikh et al., 2008]. b. Results extracted from [Pandolfi and Holzapfel, 2008] – model with GST approach and only in-plane distribution of the lamellae compared to data from [Elsheikh and Anderson, 2005]. c. Results extracted from [Petsche and Pinsky, 2013] – model with AI approach and 3D distribution of the lamellae (with different cases for the out-of-plane distribution) compared to data from [Elsheikh et al., 2008]. d. Results extracted from [Giraudet et al., 2022] – model with 3D AI approach, with different cases for the pre-elongation of the lamellae.*

keratoconus is the change in shape of cornea [Gefen et al., 2009], Carvalho *et al.* [Carvalho et al., 2009] and Giraudet *et al.* [Giraudet et al., 2022] state that the change of local mechanical properties is needed to generate a keratoconus. Figure **46** shows the maximum tissue displacement (Fig. **46**.a) and maximal diopter (Fig. **46**.b) with increasing IOP for normal and keratoconic cases from Gefen *et al.* study [Gefen et al., 2009]. The maximum displacement is more than three times greater in keratoconic corneas than in healthy tissues. For the diopter, while there is no change with pressure for healthy cornea, an increase of 8 diopters is found for keratoconic cases between 10 and 25 mmHg. In Giraudet *et al.* study, the change in diopter is also seen in the case of the keratoconus, while smaller (around 2 diopters as in [McMonnies and Boneham, 2010]). Figure **46**.c shows the results in variation of the SimK (representative diopter of the cornea) during an inflation test between 15 and 30 mmHg. It clearly showed that a change in geometry is not enough to have the expected change in diopter, but there is a need of mechanical weakness. Pandolfi *et al.* [Pandolfi et al., 2019] adopted another approach. Starting from a healthy

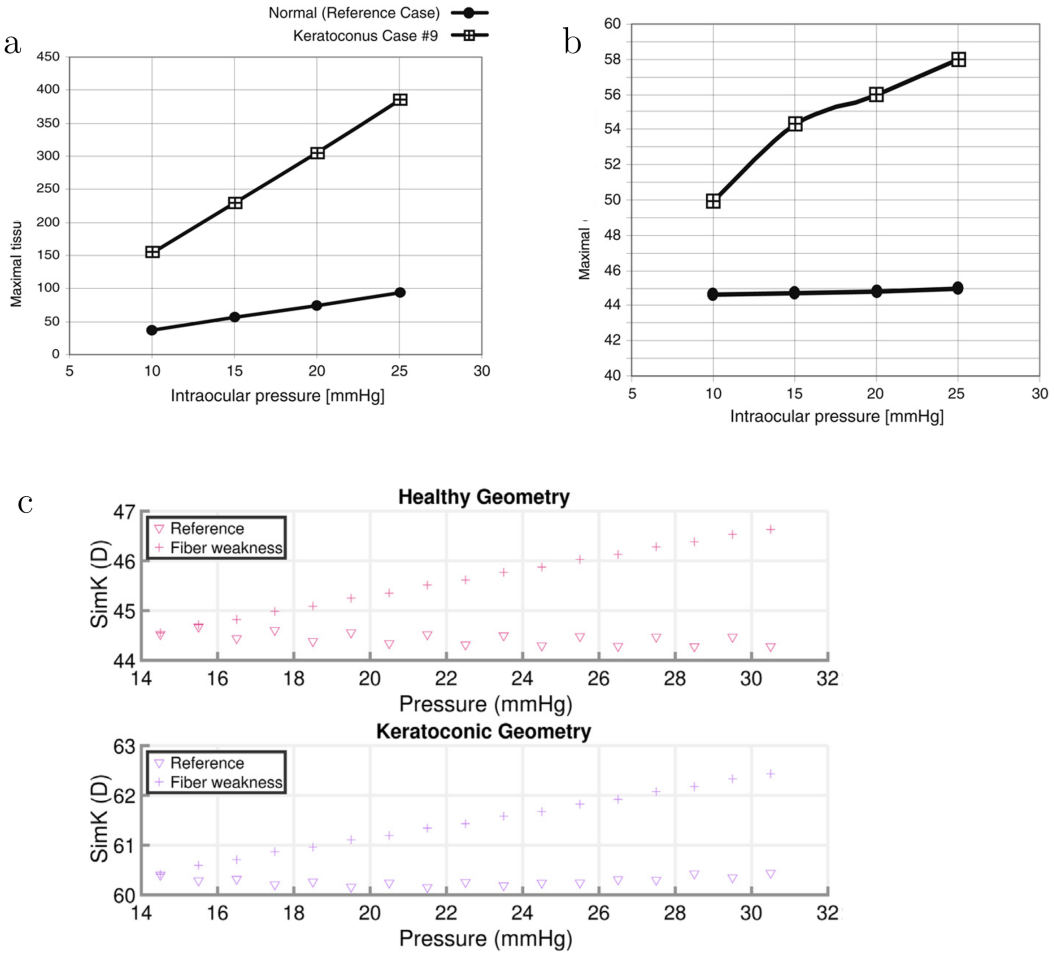

FIGURE 46. *a. Maximum corneal tissue displacement with IOP for healthy and keratoconic cases. b. Maximum dioptric power with IOP for normal and keratoconic corneas (extracted from [Gefen et al., 2009]). c. Variation of the SimK (a diopter indicator) with IOP for healthy (top) and keratoconic (bottom) geometries, for cornea with or without mechanical weakness (extracted from [Giraudet et al., 2022]).*

geometry, the authors created a network of fibrils and cross links (Fig. **47**.a.2) to represent the lamellae of collagen and their links to each other (glycosaminoglycans or other proteoglycans), and finally decreased the mechanical strength of each part of the fibrils unit cell (Fig. **47**.a.1). Looking at the displacement results of Fig. **47**.b.1–4, one must conclude that the weakening of the intra-cross link (in orange

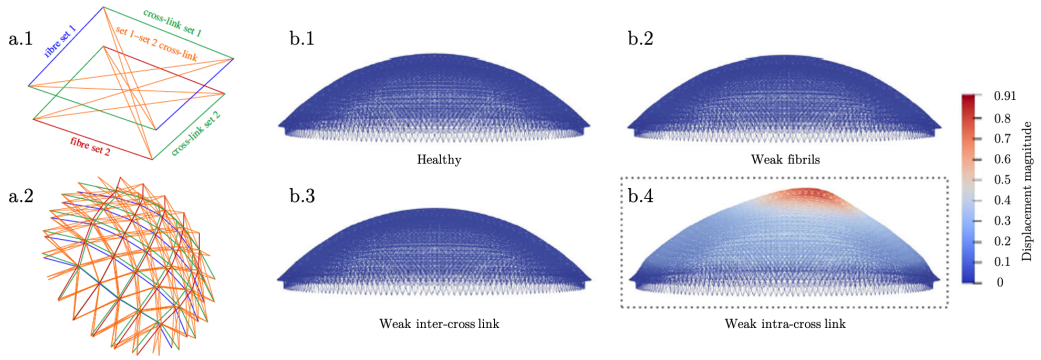

FIGURE 47. *a.1. Unit cell of the fibrils and cross links. Fibrils are divided into two sets: fiber set 1 (F1) in blue and fiber set 2 (F2) in red. Two types of cross-links are defined: cross-links between the fibrils of the same set (inter-link: C1 and C2) are in green and between the fibrils of two different sets (intra-link: C12) in orange. a.2. Fibrils and cross-link networks. b.1-4. Comparison of the deformed shape and displacement field between b.1. a healthy cornea, b.2. a cornea weakened only in the F1 and F2 fibril stiffness, b.3. a cornea weakened only in the C1 and C2 cross-link stiffness, and b.4. a cornea weakened only in the C12 cross-link stiffness.*

on Fig. **47**.a.1–2) gives a high deformability of the cornea and may lead to thinning and bulging of the tissue in the zone of the cone, as found in keratoconus.

Keratoconus has been studied numerically by various authors with different results regarding the explanation for the inception of the disease: the thinning of the zone (geometrical factor) or the decreasing of the fibrils stiffness (mechanical weakening) were considered and found to be relevant. While the geometry found for keratoconic corneas are consistent with actual cases of keratoconus, there is however no comparison of quantitative parameters with real data.

5. Conclusion

This paper presented an overview of the knowledge on cornea for mechanical modeling. It first presented it macro and microstructure (Sec. 1.), then detailed the OCT techniques used to image the cornea (Sec. 2.). Then, it showed the results of the different experiments performed on the cornea to measure its mechanical parameters (Sec. 3.) and finally how they can be used to model human cornea as an hyperelastic material reinforced by fibers (Sec. 4.). This paper did not present the viscous behavior of the cornea as it only focused on static experiments, but it has to be taken into account when modeling dynamic experiments such as air-puff.

Bibliographie

Aghamohammadzadeh, H., Newton, R. H., and Meek, K. M. (2004). X-Ray Scattering Used to Map the Preferred Collagen Orientation in the Human Cornea and Limbus. *Structure*, 12(2):249–256.

Alastrué, V., Calvo, B., Peña, E., and Doblaré, M. (2006). Biomechanical Modeling of Refractive Corneal Surgery. *Journal of Biomechanical Engineering*, 128(1):150–160.

Alastrué, V., Martínez, M., and Doblaré, M. (2008). Modelling adaptative volumetric finite growth in patient-specific residually stressed arteries. *Journal of Biomechanics*, 41(8):1773–1781.

Andreassen, T. T., Hjorth Simonsen, A., and Oxlund, H. (1980). Biomechanical Properties of Keratoconus and Normal Corneas. *Experimental Eye Research*, 31:435–441.

Ateshian, G. A., Rajan, V., Chahine, N. O., Canal, C. E., and Hung, C. T. (2009). Modeling the Matrix of Articular Cartilage Using a Continuous Fiber Angular Distribution Predicts Many Observed Phenomena. *Journal of Biomechanical Engineering*, 131.

Bay, B. K., Smith, T. S., Fyhrie, D. P., and Saad, M. (1999). Digital volume correlation: Three-dimensional strain mapping using X-ray tomography. *Experimental Mechanics*, 39(3):217–226.

Bell, J., Hayes, S., Whitford, C., Sanchez-Weatherby, J., Shebanova, O., Vergari, C., Winlove, C., Terrill, N., Sorensen, T., Elsheikh, A., and Meek, K. (2018). The hierarchical response of human corneal collagen to load. *Acta Biomaterialia*, 65:216–225.

Benoit, A., Latour, G., Marie-Claire, S.-K., and Allain, J.-M. (2016). Simultaneous microstructural and mechanical characterization of human corneas at increasing pressure. *Journal of the Mechanical Behavior of Biomedical Materials*, 60:93–105.

Billiar, K. L. and Sacks, M. S. (2000). Biaxial Mechanical Properties of the Natural and Glutaraldehyde Treated Aortic Valve Cusp—Part I: Experimental Results. *Journal of Biomechanical Engineering*, 122(1):23–30.

Bols, J., Degroote, J., Trachet, B., Verhegghe, B., Segers, P., and Vierendeels, J. (2013). A computational method to assess the in vivo stresses and unloaded configuration of patient-specific blood vessels. *Journal of Computational and Applied Mathematics*, 246:10–17.

Boote, C., Hayes, S., Abahussin, M., and Meek, K. M. (2006). Mapping Collagen Organization in the Human Cornea: Left and Right Eyes Are Structurally Distinct. *Investigative Opthalmology & Visual Science*, 47(3):901.

Bourne, W. M. (2003). Biology of the corneal endothelium in health and disease. *Eye*, 17(8):912–918.

Boyce, B., Jones, R., Nguyen, T., and Grazier, J. (2007). Stress-controlled viscoelastic tensile response of bovine cornea. *Journal of Biomechanics*, 40(11):2367–2376.

Boyce, B. L., Grazier, J. M., Jones, R. E., and Nguyen, T. D. (2008). Full-field deformation of bovine cornea under constrained inflation conditions. *Biomaterials*, 29(28):3896–3904.

Buljac, A., Jailin, C., Mendoza, A., Neggers, J., Taillandier-Thomas, T., Bouterf, A., Smaniotto, B., Hild, F., and Roux, S. (2018). Digital Volume Correlation: Review of Progress and Challenges. *Experimental Mechanics*, 58(5):661–708.

Carvalho, L. A., Prado, M., Cunha, R. H., Costa Neto, A., Paranhos Jr, A., Schor, P., and Chamon, W. (2009). Keratoconus prediction using a finite element model of the cornea with local biomechanical properties. *Arquivos Brasileiros de Oftalmologia*, 72(2):139–145.

Chakraborty, S. and Ruiz, P. D. (2012). Measurement of all orthogonal components of displacement in the volume of scattering materials using wavelength scanning interferometry. *Journal of the Optical Society of America A*, 29(9):1776.

Chang, S.-H., Zhou, D., Eliasy, A., Li, Y.-C., and Elsheikh, A. (2020). Experimental evaluation of stiffening effect induced by UVA/Riboflavin corneal cross-linking using intact porcine eye globes. *PLOS ONE*, 15(11):e0240724.

Cheng, X., Petsche, S. J., and Pinsky, P. M. (2015). A structural model for the *in vivo* human cornea including collagen-swelling interaction. *Journal of The Royal Society Interface*, 12(109):20150241.

Ciarlet, P. and Geymonat, G. (1982). On consitutive equations in compressible non linear elasticity. *Comptes rendus des séances de l'Académie des Sciences.*, 295(4):423–426.

Davis, A. (2019). *Tomographie par cohérence optique confocale en ligne multimodale pour le diagnostic non invasif des cancers cutanés*. PhD thesis, Université Paris-Saclay.

De Stefano, V. S., Ford, M. R., Seven, I., and Dupps, W. J. (2020). Depth-Dependent Corneal Biomechanical Properties in Normal and Keratoconic Subjects by Optical Coherence Elastography. *Translational Vision Science & Technology*, 9(7):4.

den Toonder, J. M. J., Ramone, Y., van Dijken, A. R., Beijer, J. G. J., and Zhang, G. Q. (2005). Viscoelastic Characterization of Low-Dielectric Constant SiLK Films Using Nanoindentation in Combination With Finite Element Modeling. *Journal of Electronic Packaging*, 127(3):276–285.

Dias, J., Diakonis, V. F., Lorenzo, M., Gonzalez, F., Porras, K., Douglas, S., Avila, M., Yoo, S. H., and Ziebarth, N. M. (2015). Corneal stromal elasticity and viscoelasticity assessed by atomic force microscopy after different cross linking protocols. *Experimental Eye Research*, 138:1–5.

Dias, J. M. and Ziebarth, N. M. (2013). Anterior and posterior corneal stroma elasticity assessed using nanoindentation. *Experimental Eye Research*, 115:41–46.

Drexler, W., Liu, M., Kumar, A., Kamali, T., Unterhuber, A., and Leitgeb, R. A. (2014). Optical coherence tomography today: speed, contrast, and multimodality. *Journal of Biomedical Optics*, 19(7):071412.

Dua, H. S., Faraj, L. A., Said, D. G., Gray, T., and Lowe, J. (2013). Human Corneal Anatomy Redefined. *Ophthalmology*, 120(9):1778–1785.

Eberwein, P., Nohava, J., Schlunck, G., and Swain, M. (2014). Nanoindentation Derived Mechanical Properties of the Corneoscleral Rim of the Human Eye. *Key Engineering Materials*, 606:117–120.

Elsheikh, A., Alhasso, D., and Rama, P. (2008). Biomechanical properties of human and porcine corneas. *Experimental Eye Research*, 86(5):783–790.

Elsheikh, A. and Anderson, K. (2005). Comparative study of corneal strip extensometry and inflation tests. *Journal of The Royal Society Interface*, 2(3):177–185.

Espana, E. M. and Birk, D. E. (2020). Composition, structure and function of the corneal stroma. *Experimental Eye Research*, 198:108137.

Ford, M. R., Dupps, W. J., Rollins, A. M., Roy, A. S., and Hu, Z. (2011). Method for optical coherence elastography of the cornea. *Journal of Biomedical Optics*, 16(1):016005.

Fratzl, P., Hulmes, D. J. S., Wess, T. J., Avery, N. C., Bailey, A. J., Ker, R., Silver, F. H., Landis, W. J., Gupta, H. S., Buehler, M. J., Kjaer, M., Magnusson, S. P., Biewener, A. A., Holzapfel, G. A., Purslow, P. P., Meek, K. M., Currey, J., Zalansky, P., Blank, R., Boskey, A. L., Sander, E. A., and Barocas, V. H. (2008). *Collagen: structure and mechanics*. Springer, New York. OCLC: ocn172979453.

Fu, J. (2014). Identification of corneal mechanical properties using optical tomography and digital volume correlation. *Thèse de l'Université de Technologie de Troyes*, page 201.

Fu, J., Pierron, F., and Ruiz, P. D. (2013). Elastic stiffness characterization using three-dimensional full-field deformation obtained with optical coherence tomography and digital volume correlation. *Journal of Biomedical Optics*, 18(12):121512.

Gasser, T. C., Ogden, R. W., and Holzapfel, G. A. (2006). Hyperelastic modelling of arterial layers with distributed collagen fibre orientations. *Journal of The Royal Society Interface*, 3(6):15–35.

Gatinel, D., Malet, J., Hoang-Xuan, T., and Azar, D. T. (2011). Corneal Elevation Topography: Best Fit Sphere, Elevation Distance, Asphericity, Toricity, and Clinical Implications:. *Cornea*, 30(5):508–515.

Gefen, A., Shalom, R., Elad, D., and Mandel, Y. (2009). Biomechanical analysis of the keratoconic cornea. *Journal of the Mechanical Behavior of Biomedical Materials*, 2(3):224–236.

Giraudet, C., Diaz, J., Le Tallec, P., and Allain, J.-M. (2022). Multiscale mechanical model based on patient-specific geometry: Application to early keratoconus development. *Journal of the Mechanical Behavior of Biomedical Materials*, page 105121.

Grieve, K. (2019). Tomographie par Cohérence Optique. *La lumière et ses applications*, 95:19–23.

Grieve, K., Ghoubay, D., Georgeon, C., Latour, G., Nahas, A., Plamann, K., Crotti, C., Bocheux, R., Borderie, M., Nguyen, T.-M., Andreiuolo, F., Schanne-Klein, M.-C., and Borderie, V. (2017). Stromal striae: a new insight into corneal physiology and mechanics. *Scientific Reports*, 7(1):13584.

Hashemi, H. (2005). Distribution of intraocular pressure in healthy Iranian individuals: the Tehran Eye Study. *British Journal of Ophthalmology*, 89(6):652–657.

Hayashi, S., Osawa, T., and Tohyama, K. (2002). Comparative observations on corneas, with special reference to bowman's layer and descemet's membrane in mammals and amphibians. *Journal of Morphology*, 254(3):247–258.

Holmes, D. F., Gilpin, C. J., Baldock, C., Ziese, U., Koster, A. J., and Kadler, K. E. (2001). Corneal collagen fibril structure in three dimensions: Structural insights into fibril assembly, mechanical properties, and tissue organization. *Proceedings of the National Academy of Sciences*, 98(13):7307–7312.

Holzapfel, G. A., Niestrawska, J. A., Ogden, R. W., Reinisch, A. J., and Schriefl, A. J. (2015). Modelling non-symmetric collagen fibre dispersion in arterial walls. *Journal of The Royal Society Interface*, 12(106):20150188.

Holzapfel, G. A. and Ogden, R. W. (2009). Constitutive modelling of passive myocardium: a structurally based framework for material characterization. *Philosophical Transactions of the Royal Society A: Mathematical, Physical and Engineering Sciences*, 367(1902):3445–3475.

Holzapfel, G. A., Ogden, R. W., and Sherifova, S. (2019). On fibre dispersion modelling of soft biological tissues: a review. *Proceedings of the Royal Society A: Mathematical, Physical and Engineering Sciences*, 475(2224):20180736.

Janunts, E., Kannengießer, M., and Langenbucher, A. (2015). Parametric fitting of corneal height data to a biconic surface. *Zeitschrift für Medizinische Physik*, 25(1):25–35.

Jin, Z., Khazaeinezhad, R., Zhu, J., Yu, J., Qu, Y., He, Y., Li, Y., Gomez Alvarez-Arenas, T. E., Lu, F., and Chen, Z. (2019). In-vivo 3D corneal elasticity using air-coupled ultrasound optical coherence elastography. *Biomedical Optics Express*, 10(12):6272.

Jor, J. W. Y., Nash, M. P., Nielsen, P. M. F., and Hunter, P. J. (2011). Estimating material parameters of a structurally based constitutive relation for skin mechanics. *Biomechanics and Modeling in Mechanobiology*, 10(5):767–778.

Kaufman, H., Barron, B., and McDonald, M. (1998). *The Cornea*. Woburn.

Kennedy, B. F., Kennedy, K. M., and Sampson, D. D. (2014). A Review of Optical Coherence Elastography: Fundamentals, Techniques and Prospects. *IEEE Journal of Selected Topics in Quantum Electronics*, 20(2):272–288.

Kling, S., Bekesi, N., Dorronsoro, C., Pascual, D., and Marcos, S. (2014). Corneal Viscoelastic Properties from Finite-Element Analysis of In Vivo Air-Puff Deformation. *PLoS ONE*, 9(8):e104904.

Kling, S., Remon, L., Pérez-Escudero, A., Merayo-Lloves, J., and Marcos, S. (2010). Corneal Biomechanical Changes after Collagen Cross-Linking from Porcine Eye Inflation Experiments. *Investigative Opthalmology & Visual Science*, 51(8):3961.

Komai, Y. and Ushikif, T. (1991). The Three-Dimensional Organization of Collagen Fibrils in the Human Cornea and Sclera. *Investigative Ophthalmology & Visual Science*, 32(8):2244–2258.

Lan, G., Aglyamov, S. R., Larin, K. V., and Twa, M. D. (2021). In Vivo Human Corneal Shear-wave Optical Coherence Elastography. *Optometry and Vision Science*, 98(1):58–63.

Larin, K. V. and Sampson, D. D. (2017). Optical coherence elastography – OCT at work in tissue biomechanics [Invited]. *Biomedical Optics Express*, 8(2):1172.

Last, J. A., Thomasy, S. M., Croasdale, C. R., Russell, P., and Murphy, C. J. (2012). Compliance profile of the human cornea as measured by atomic force microscopy. *Micron*, 43(12):1293–1298.

Lombardo, G., Serrao, S., Rosati, M., and Lombardo, M. (2014). Analysis of the Viscoelastic Properties of the Human Cornea Using Scheimpflug Imaging in Inflation Experiment of Eye Globes. *PLoS ONE*, 9(11):e112169.

Luyckx, T., Verstraete, M., De Roo, K., De Waele, W., Bellemans, J., and Victor, J. (2014). Digital image correlation as a tool for three-dimensional strain analysis in human tendon tissue. *Journal of Experimental Orthopaedics*, 1(1):7.

Marchini, M., Morocutti, M., Ruggeri, A., Koch, M. H., Bigi, A., and Roveri, N. (1986). Differences in the Fibril Structure of Corneal and Tendon Collagen. An Electron Microscopy and X-Ray Diffraction Investigation. *Connective Tissue Research*, 15(4):269–281.

Markert, B., Ehlers, W., and Karajan, N. (2005). A general polyconvex strain-energy function for fiber-reinforced materials. *PAMM*, 5(1):245–246.

Mashige, K. P. (2013). A review of corneal diameter, curvature and thickness values and influencing factors*. *African Vision and Eye Health*, 72(4):185–194.

McMonnies, C. W. and Boneham, G. C. (2010). Corneal Responses to Intraocular Pressure Elevations in Keratoconus. *Cornea*, 29(7):764–770.

Meek, K. M. and Boote, C. (2009). The use of X-ray scattering techniques to quantify the orientation and distribution of collagen in the corneal stroma. *Progress in Retinal and Eye Research*, 28(5):369–392.

Meek, K. M. and Knupp, C. (2015). Corneal structure and transparency. *Progress in Retinal and Eye Research*, 49:1–16.

Meek, K. M. and Quantock, A. J. (2001). The Use of X-ray Scattering Techniques to Determine Corneal Ultrastructure. *Progress in Retinal and Eye Research*, 20(1):95–137.

Meng, F., Chen, C., Hui, S., Wang, J., Feng, Y., and Sun, C. (2019). Three-dimensional static optical coherence elastography based on inverse compositional Gauss-Newton digital volume correlation. *Journal of Biophotonics*, 12(9).

Mergler, S. and Pleyer, U. (2007). The human corneal endothelium: New insights into electrophysiology and ion channels. *Progress in Retinal and Eye Research*, 26(4):359–378.

Mikula, E., Hollman, K., Chai, D., Jester, J. V., and Juhasz, T. (2014). Measurement of Corneal Elasticity with an Acoustic Radiation Force Elasticity Microscope. *Ultrasound in Medicine & Biology*, 40(7):1671–1679.

Mikula, E., Winkler, M., Juhasz, T., Brown, D. J., Shoa, G., Tran, S., Kenney, M. C., and Jester, J. V. (2018). Axial mechanical and structural characterization of keratoconus corneas. *Experimental Eye Research*, 175:14–19.

Mikula, E. R., Jester, J. V., and Juhasz, T. (2016). Measurement of an Elasticity Map in the Human Cornea. *Investigative Opthalmology & Visual Science*, 57(7):3282.

Montanino, A., Gizzi, A., Vasta, M., Angelillo, M., and Pandolfi, A. (2018). Modeling the biomechanics of the human cornea accounting for local variations of the collagen fibril architecture. *ZAMM - Journal of Applied Mathematics and Mechanics / Zeitschrift für Angewandte Mathematik und Mechanik*, 98(12):2122–2134.

Naderan, M. (2017). Histopathologic findings of keratoconus corneas underwent penetrating keratoplasty according to topographic measurements and keratoconus severity. *International Journal of Ophthalmology*.

Nahas, A., Bauer, M., Roux, S., and Boccara, A. C. (2013). 3D static elastography at the micrometer scale using Full Field OCT. *Biomedical Optics Express*, 4(10):2138.

Najmi, H. (2019). The correlation between keratoconus and eye rubbing: a review. *International Journal of Ophthalmology*, 12(11):1775–1781.

Napoli, P. E., Nioi, M., d'Aloja, E., Loy, F., and Fossarello, M. (2020). The architecture of corneal stromal striae on optical coherence tomography and histology in an animal model and in humans. *Scientific Reports*, 10(1):19861.

Nash, I. S., Greene, P. R., and Foster, C. (1982). Comparison of mechanical properties of keratoconus and normal corneas. *Experimental Eye Research*, 35(5):413–424.

Nguyen, T. D. and Boyce, B. L. (2011). An inverse finite element method for determining the anisotropic properties of the cornea. *Biomechanics and Modeling in Mechanobiology*, 10(3):323–337.

Nguyen, T. D., Jones, R. E., and Boyce, B. L. (2008). A Nonlinear Anisotropic Viscoelastic Model for the Tensile Behavior of the Corneal Stroma. *Journal of Biomechanical Engineering*, 130(4):041020.

Nohava, J., Swain, M., Lang, S. J., Maier, P., Heinzelmann, S., Reinhard, T., and Eberwein, P. (2018). Instrumented indentation for determination of mechanical properties of human cornea after ultraviolet-A crosslinking: MECHANICAL PROPERTIES OF HUMAN CORNEA. *Journal of Biomedical Materials Research Part A*, 106(5):1413–1420.

Norouzpour, A. and Mehdizadeh, A. (2012). A Novel Insight into Keratoconus: Mechanical Fatigue of the Cornea. *Med Hypothesis Discov Innov Ophthalmol.*, 1(1):4.

Okuyama, K. (2008). Revisiting the Molecular Structure of Collagen. *Connective Tissue Research*, 49(5):299–310.

Okuyama, K., Xu, X., Iguchi, M., and Noguchi, K. (2006). Revision of collagen molecular structure. *Biopolymers*, 84(2):181–191.

Pan, B., Qian, K., Xie, H., and Asundi, A. (2009). Two-dimensional digital image correlation for in-plane displacement and strain measurement: a review. *Measurement Science and Technology*, 20(6):062001.

Pandolfi, A., Gizzi, A., and Vasta, M. (2019). A microstructural model of cross-link interaction between collagen fibrils in the human cornea. *Philosophical Transactions of the Royal Society A: Mathematical, Physical and Engineering Sciences*, 377(2144):20180079.

Pandolfi, A. and Holzapfel, G. A. (2008). Three-Dimensional Modeling and Computational Analysis of the Human Cornea Considering Distributed Collagen Fibril Orientations. *Journal of Biomechanical Engineering*, 130(6):061006.

Petsche, S. J. and Pinsky, P. M. (2013). The role of 3-D collagen organization in stromal elasticity: a model based on X-ray diffraction data and second harmonic-generated images. *Biomechanics and Modeling in Mechanobiology*, 12(6):1101–1113.

Pierce, D. M., Unterberger, M. J., Trobin, W., Ricken, T., and Holzapfel, G. A. (2016). A microstructurally based continuum model of cartilage viscoelasticity and permeability incorporating measured statistical fiber orientations. *Biomechanics and Modeling in Mechanobiology*, 15(1):229–244.

Pinsky, P. M., van der Heide, D., and Chernyak, D. (2005). Computational modeling of mechanical anisotropy in the cornea and sclera. *Journal of Cataract and Refractive Surgery*, 31(1):136–145.

Qu, Y., Ma, T., He, Y., Zhu, J., Dai, C., Yu, M., Huang, S., Lu, F., Shung, K. K., Zhou, Q., and Chen, Z. (2016). Acoustic Radiation Force Optical Coherence Elastography of Corneal Tissue. *IEEE Journal of Selected Topics in Quantum Electronics*, 22(3):288–294.

Ramier, A., Eltony, A. M., Chen, Y., Clouser, F., Birkenfeld, J. S., Watts, A., and Yun, S.-H. (2020). In vivo measurement of shear modulus of the human cornea using optical coherence elastography. *Scientific Reports*, 10(1):17366.

Ramos, J. L. B., Li, Y., and Huang, D. (2009). Clinical and research applications of anterior segment optical coherence tomography - a review. *Clinical & Experimental Ophthalmology*, 37(1):81–89.

Raoux, C., Schmeltz, M., Bied, M., Alnawaiseh, M., Hansen, U., Latour, G., and Schanne-Klein, M.-C. (2021). Quantitative structural imaging of keratoconic corneas using polarization-resolved SHG microscopy. *Biomedical Optics Express*, 12(7):4163.

Ruberti, J. W., Sinha Roy, A., and Roberts, C. J. (2011). Corneal Biomechanics and Biomaterials. *Annual Review of Biomedical Engineering*, 13(1):269–295.

Ruiz, P. D., Zhou, Y., Huntley, J. M., and Wildman, R. D. (2004). Depth-resolved whole-field displacement measurement using wavelength scanning interferometry. *Journal of Optics A: Pure and Applied Optics*, 6(7):679–683.

Sacks, M. S. (2003). Incorporation of Experimentally-Derived Fiber Orientation into a Structural Constitutive Model for Planar Collagenous Tissues. *Journal of Biomechanical Engineering*, 125(2):280–287.

Sardar, D. K., Swanland, G.-Y., Yow, R. M., Thomas, R. J., and Tsin, A. T. C. (2007). Optical properties of ocular tissues in the near infrared region. *Lasers in Medical Science*, 22(1):46–52.

Scarcelli, G., Besner, S., Pineda, R., Kalout, P., and Yun, S. H. (2015). In Vivo Biomechanical Mapping of Normal and Keratoconus Corneas. *JAMA Ophthalmology*, 133(4):480.

Scarcelli, G., Besner, S., Pineda, R., and Yun, S. H. (2014). Biomechanical Characterization of Keratoconus Corneas Ex Vivo With Brillouin Microscopy. *Investigative Opthalmology & Visual Science*, 55(7):4490.

Scarcelli, G., Kling, S., Quijano, E., Pineda, R., Marcos, S., and Yun, S. H. (2013). Brillouin Microscopy of Collagen Crosslinking: Noncontact Depth-Dependent Analysis of Corneal Elastic Modulus. *Investigative Opthalmology & Visual Science*, 54(2):1418.

Scarcelli, G., Pineda, R., and Yun, S. H. (2012). Brillouin Optical Microscopy for Corneal Biomechanics. *Investigative Opthalmology & Visual Science*, 53(1):185.

Seiler, T. G., Shao, P., Eltony, A., Seiler, T., and Yun, S.-H. (2019). Brillouin Spectroscopy of Normal and Keratoconus Corneas. *American Journal of Ophthalmology*, 202:118–125.

Shao, P., Eltony, A. M., Seiler, T. G., Tavakol, B., Pineda, R., Koller, T., Seiler, T., and Yun, S.-H. (2019). Spatially-resolved Brillouin spectroscopy reveals biomechanical abnormalities in mild to advanced keratoconus in vivo. *Scientific Reports*, 9(1):7467.

Simonini, I. and Pandolfi, A. (2015). Customized Finite Element Modelling of the Human Cornea. *PLOS ONE*, 10(6):e0130426.

Singh, M., Li, J., Han, Z., Raghunathan, R., Nair, A., Wu, C., Liu, C.-H., Aglyamov, S., Twa, M. D., and Larin, K. V. (2017). Assessing the effects of riboflavin/UV-A crosslinking on porcine corneal mechanical anisotropy with optical coherence elastography. *Biomedical Optics Express*, 8(1):349.

Spoerl, E., Huhle, M., and Seiler, T. (1998). Induction of Cross-links in Corneal Tissue. *Experimental Eye Research*, 66(1):97–103.

Studer, H., Larrea, X., Riedwyl, H., and Büchler, P. (2010). Biomechanical model of human cornea based on stromal microstructure. *Journal of Biomechanics*, 43(5):836–842.

Venkateswaran, N., Galor, A., Wang, J., and Karp, C. L. (2018). Optical coherence tomography for ocular surface and corneal diseases: a review. *Eye and Vision*, 5(1):13.

Wang, S. and Larin, K. V. (2014). Noncontact depth-resolved micro-scale optical coherence elastography of the cornea. *Biomedical Optics Express*, 5(11):3807.

Wang, S. and Larin, K. V. (2015). Optical coherence elastography for tissue characterization: a review. *Journal of Biophotonics*, 8(4):279–302.

Whitford, C., Movchan, N. V., Studer, H., and Elsheikh, A. (2018). A viscoelastic anisotropic hyperelastic constitutive model of the human cornea. *Biomechanics and Modeling in Mechanobiology*, 17(1):19–29.

Whitford, C., Studer, H., Boote, C., Meek, K. M., and Elsheikh, A. (2015). Biomechanical model of the human cornea: Considering shear stiffness and regional variation of collagen anisotropy and density. *Journal of the Mechanical Behavior of Biomedical Materials*, 42:76–87.

Winkler, M., Chai, D., Kriling, S., Nien, C. J., Brown, D. J., Jester, B., Juhasz, T., and Jester, J. V. (2011). Nonlinear Optical Macroscopic Assessment of 3-D Corneal Collagen Organization and Axial Biomechanics. *Investigative Opthalmology & Visual Science*, 52(12):8818.

Winkler, M., Shoa, G., Xie, Y., Petsche, S. J., Pinsky, P. M., Juhasz, T., Brown, D. J., and Jester, J. V. (2013). Three-Dimensional Distribution of Transverse Collagen Fibers in the Anterior Human Corneal Stroma. *Investigative Opthalmology & Visual Science*, 54(12):7293.

Wollensak, G., Spoerl, E., and Seiler, T. (2003). Stress-strain measurements of human and porcine corneas after riboflavin–ultraviolet-A-induced cross-linking. *Journal of Cataract and Refractive Surgery*, 29(9):1780–1785.

Yun, S. H. and Chernyak, D. (2018). Brillouin microscopy: assessing ocular tissue biomechanics. *Current Opinion in Ophthalmology*, 29(4):299–305.

